DIGITAL SIGNAL PROCESSING TECHNIQUES FOR SEMICONDUCTOR COMPTON CAMERAS

Thesis submitted in accordance with the requirements of the University of Liverpool for the degree of Doctor in Philosophy

by

David Peter Thomas Scraggs

November 2007

Simple intelligence testing

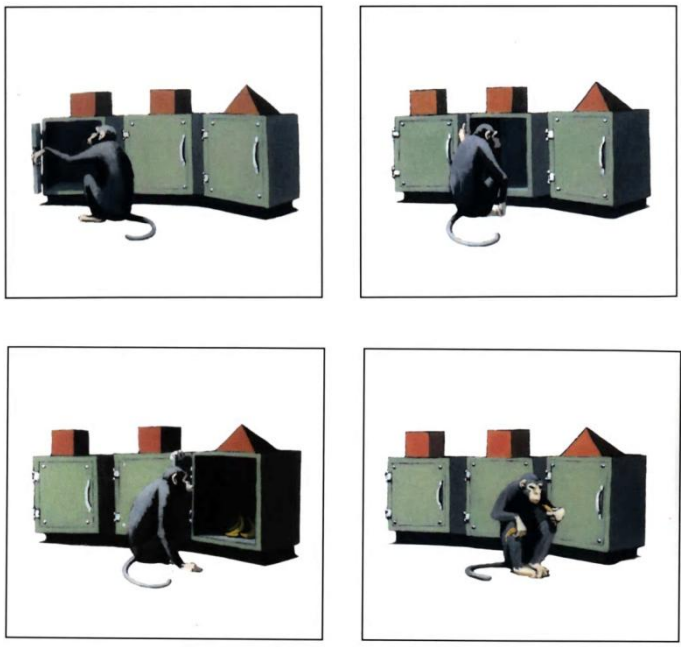

A lot of people never use their initiative because no-one told them to

Abstract

The work presented in this thesis has focused on the development of a low dose Compton camera for nuclear medicine. A Compton camera composed of two high-purity planar germanium orthogonal-strip detectors has been constructed. Fast digital data acquisition has been utilised for the application of pulse shape analysis techniques. A simple back projection imaging code has been developed and validated with a Geant4 radiation transport simulation of the Compton camera configuration.

A ^{137}Cs isotropic source and a ^{22}Na anisotropic source have been experimentally reconstructed. Parametric pulse shape analysis was applied to both data sets and has been shown to increase the detector spatial resolution from a raw granularity of 5x5x20mm to a spatial resolution that can be represented by a Gaussian distribution with a standard deviation of $1.5\text{mm} < \sigma < 2\text{mm}$ in all dimensions; this result was in-part derived from Geant4 simulations. Qualitatively poor images have been shown to result – based wholly on simulation – from Gaussian spatial-resolution distributions that have a standard deviation of greater than 4mm. A partial experimental basis-data-set has been developed and proved capable of providing 1.9mm FWHM average spatial resolution through the depth axis of a single detector crystal.

A novel technique to identify gamma ray scattering within single detector closed-face-pixels – hitherto unrecognised – has also been introduced in this thesis. This technique, henceforth known as Digital Compton Suppression (DiCS), is based on spectral analysis and has demonstrated the ability of identifying events in which the Compton scattering and photoelectric absorption sites are separated by 13mm in the direction of the electric field.

Acknowledgements

I would first like to thank Paul Nolan for allowing me to pursue a Ph.D and supervising me throughout. I would also like to thank the *taxpayers* who financed my research and the occasional jaunt. Hopefully, in some small way, they will benefit from this research. A special thank you is also reserved to the individuals who unselfishly contribute to the internet and empower other individuals with free knowledge; free as in freedom! Additionally, I would also like to thank the few great teachers who have had a profound influence on my personal development and without whom my appreciation of the awe-inspiring world would not be so precious.

I would like to high-five, hug, kiss, and maybe more, all of the people that made me realise that the past three years were not as dystopian as I have implied in numerous diatribes. Willy 'fit Will' Turner always managed to distract me in the early days with chess; and win! I needed that lad! B 'bring me my...' M provided immeasurable quantities of joy with his big chin and other notable appendages throughout; you are an absolute disgrace, but I love ya! Moonie and Mercer... what can I say to the two people who were there at the very start, revelled in the good times and stood by me during the bad, other than you are both stars and I hope you are both there at the end! Oh, and I'm – now officially, in black and white – the ultimate arm wrestle champ! Sai and Craig, you are true adventurers and provided the breathless, masculine, physical exertion that I yearn for. Grinto, Reggie and Bager I owe you boys a massive thank you for some great times, support and nights out, and a big apology for being such an antagonistic t$%t!

It has also been a privilege to work with and socialise with so many other great people who have enriched the experience; Arron, thanks for the thrashings in squash, being a cool guy

and encouragement during the 32oz steak ordeal; Markos, you're nuts and that's what I love about you, maybe we'll get that AFF license one day; Carl, you big militant Viking, thanks for the debates, I'm looking forward to the new ones; Meister, it does end one day... I promise! Special thanks also go to: Mather, Gerard, Jenny, Suzanne, Laura, Majid, Toby, John, AJ and the entire NSG.

It's a true pleasure to thank my mother and father (for my brains and beauty ☺) and my sister for always being there for me and providing me with unconditional love and support, even when I have most definitely not deserved it.

So, after that eruption of affection... here's to little Moon, pastures new and a halcyon future for *everybody* who's special to me! Onwards to chapter 8!

Contents

Chapter 1

Introduction

Given the common lineage of medical imaging and nuclear physics, it is perhaps fitting that advances in one field may complement the other. The demands placed on modern gamma-ray spectroscopy have driven the development of composite segmented germanium sensors, offering excellent energy and spatial resolution. Whilst new detector arrays are being investigated by large international collaborations [Del99][Sim06] for the purpose of probing the nucleus, their technological advances are equally applicable to nuclear medicine. SmartPET intends to demonstrate this transferability through the utilisation of planar germanium sensors as proposed in [Phl02] coupled with gamma-ray tracking. The project's name is an appropriate abbreviation as the system was initially aimed at small animal positron emission tomography. However, project evolution has now occurred to encompass single photon emission imaging as described in [Mar01] and [Vet04]. Although two modalities can be investigated with SmartPET, the effort behind this thesis has unwaveringly supported single photon studies. An interdisciplinary approach has been taken whereby original solutions related to Compton scattering and pulse-shape analysis have been developed. Reconstructed images of real and simulated radioisotopes are presented herein.

1.1 Motivation

The foundation of medical imaging rests on the creative spark of Roentgen who ingeniously created the world's first x-ray image, triggering an avalanche of patient demand in the

process. This is hardly surprising as medical diagnosis had always involved measurements of vital statistics or intrusive surgery, which itself incurred a high probability of infection and death. Radiology has now matured and is rightfully widespread, but it does have inherent limitations and alternative modalities are now available.

The current comprehensive suite of medical imaging modalities now includes nuclear magnetic resonance, nuclear medicine and ultrasound. The principal objectives of each modality are the production of images which allow informed readability, so that an accurate interpretation of the diagnostically-critical features can be made. Consequently, the clinical information required will usually determine the favoured modality.

Nuclear medicine has a distinct advantage when the physiological functioning of an internal organ is of interest. It is unique for studying myocardial perfusion/infarction, cerebral perfusion, and thyroid, liver and renal functions [Hua00]. Radiopharmaceuticals, an important field of research in its own right, are internally assimilated and tracked by means of detecting the emitted radiation. No biological differentiation is made between a radiopharmaceutical and its stable equivalent. Therefore, extremely chemically-active organs which absorb the radiopharmaceutical in abundance become conspicuous. Conversely, organs which fail to absorb the radiopharmaceutical also appear abnormal.

Nuclear medicine exclusively refers to positron emission tomography (PET) and single photon emission computed tomography (SPECT). PET has seen a dramatic improvement in spatial resolution, and a modern clinical scanner can achieve approximately 5mm [Tar03] without the assistance of geometrical compensation for patient movement. A multiple gated acquisition scan (MUGA) can achieve sub 4mm [Hue99]. On the contrary, SPECT studies have seen only a marginal increase in spatial resolution. A clinical gamma camera using a parallel-hole collimator to image the most common radiopharmaceutical (^{99m}Tc), achieves a spatial resolution of approximately 10mm [Che03] when the source is 10cm from the camera front face. Compounding this poor resolution is the inherently low sensitivity of clinical systems in which less than 1% [Che03] of gamma rays incident on the camera assembly are actually detected, adding to the Poisson noise of the images. Spatial resolution and efficiency is overwhelmingly determined by the collimator. Removing the collimator

assembly clearly has potential benefits for single photon imaging, and a potential alternative based on Compton kinematics is the motivation for this thesis.

1.2 Conventional Gamma-Ray Imaging

Almost all nuclear medicine studies are performed with a gamma camera, which will invariably be a derivative of the Anger camera as developed by Hal Anger [Ang58]. A schematic of a gamma camera is shown in Fig. 1.1. Anger originally used a 1cm thick single crystal of NaI(Tl) as the photon absorber, coupled to an array of photomultiplier tubes via a light guide. NaI(Tl) is still the most commonly used scintillator, although other scintillator materials are sometimes favoured. PET studies require thicker crystals than 1cm but the photopeak efficiency for 140keV photons (^{99m}Tc) in a 1cm thick NaI(Tl) crystal is sufficiently in excess of 85%. A typical crystal has an area of 40x60cm which can support 30-50 photomultiplier tubes.

Scintillation light from an interaction is simultaneously split among several photomultiplier tubes (PMT). A weighted centroid positioning algorithm is needed to analyse all PMT signals and weight the signal strengths accordingly to determine the original interaction location. The interaction locations can only be defined in two dimensions since the PMTs can only be arranged in a single plane. Although the interaction location can be partially defined, no information regarding the incident photons' direction can be assigned and the source location can lie arbitrarily in space. A collimator acts to provide directional sensitivity, allowing image reconstructions to project out into a two-dimensional patient plane, thus building an image of a distributed source. This method is inherently inefficient because the overwhelming majority of photons are absorbed in the collimator.

The collimator shown in Fig. 1.1 is the workhorse parallel-hole collimator. Holes are typically 1.9mm across and run perpendicular to the crystal face, whilst septa thicknesses are 0.2mm. Collimator thickness is determined by gamma-ray energy; a thickness of 27mm is commonly used for 140keV. System resolutions are reported as 4.2mm FWHM at 0mm from the camera face and 8.3mm FWHM at 10mm from the camera face [PICKER]. Not all imaging events are constructive, erroneous data arise from detector scattering, patient scattering,

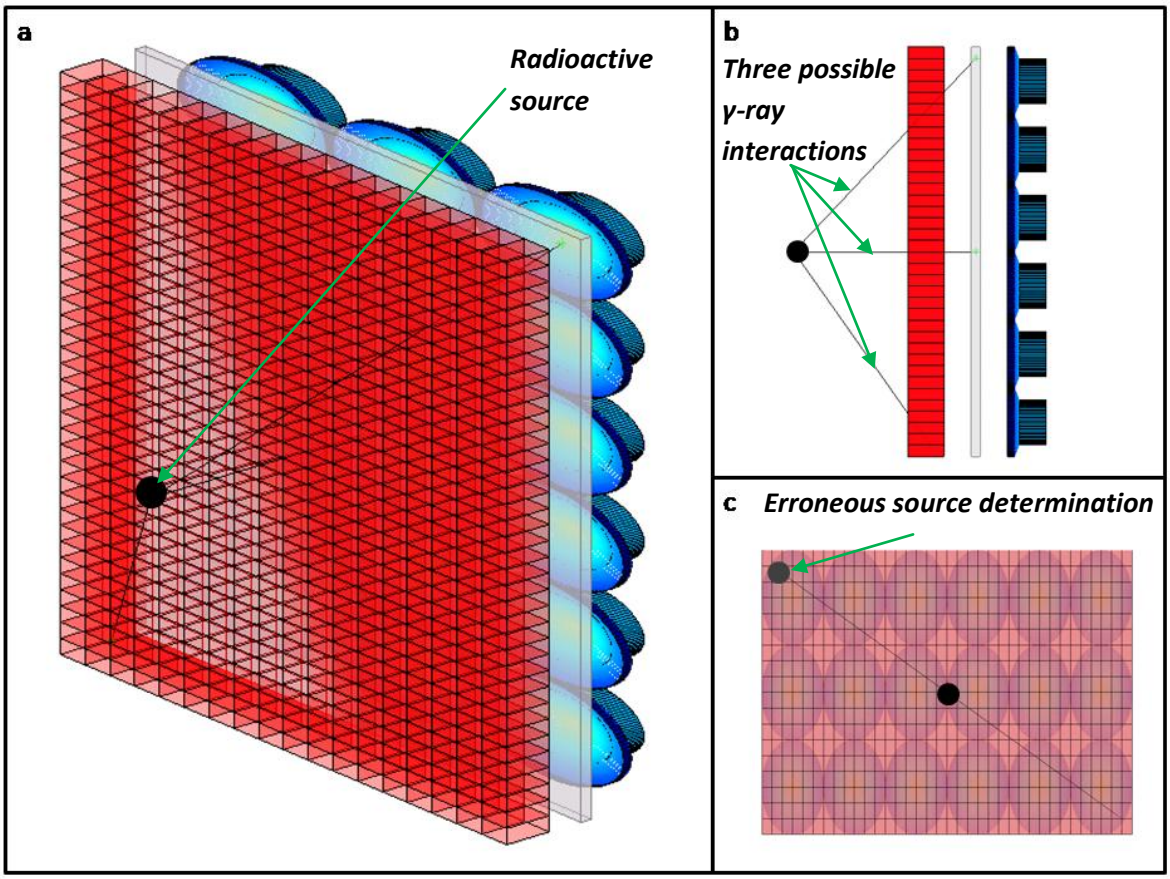

Figure 1.1: A schematic of a gamma camera from three viewing perspectives. The collimator is shown in red, NaI(Tl) crystal in grey, and PMTs in blue. Image a) shows an isotropic radioactive source located in front the parallel-hole collimator. Image b) shows three possible interactions: the photon traverses a hole, the photon is absorbed, and the photon penetrates the collimator. Image c) shows how an invalid source location (highlighted) could be determined from the penetrative ray. The PMTs can clearly be seen behind the collimators in image c), illustrating how individual signals can be weighted to calculate the interaction location.

collimator scattering, and septal penetration. Compton scattering becomes a significant source of degradation at higher energies. Other collimator configurations are available, pinhole, converging and diverging are the most common, but they all have the same inherent problems and their use is much less common.

SPECT images are simply an extension of the 2D intensity images formed from the gamma camera and collimator assembly. The 3D distribution is estimated from a set of 2D projections acquired by the planar camera from a number of views surrounding the patient. Reconstruction algorithms can be divided into two main types: analytical and iterative. Analytical methods are computationally efficient and as a result they are the most common, with the most popular algorithm being filtered back projection (FBP) [Boc00]. FBP simply runs the projections back through the source. Star-like artefacts appear which can be

removed with a high-pass filter. FBP does not account for the Poisson statistics of data collection, characteristics of the imaging device, attenuation or scattering, and the resulting images are often of poor quality. Alternatively, iterative algorithms start with a system matrix that contains an initial estimate of the source distribution and knowledge of the imaging system.

Assuming the source is in free space, the collimator detection efficiency, g, defined as the fraction of gamma rays passing through the collimator per gamma ray emitted is given by [Sor87]:

$$g \approx K\left(\frac{d}{l}\right)^2\left[\frac{d^2}{(d^2+t^2)}\right] \tag{1.1}$$

where K is a constant related to collimator hole shape, d is the collimator diameter, l is the hole length and t is the septum thickness. The FWHM of a reconstructed point source defines the collimator resolution, R_c, and is given by [Sor87]:

$$R_c \approx \frac{d(l+b)}{l} \tag{1.2}$$

where b is the collimator to source separation. It can be seen that collimator resolution improves as the ratio of the hole diameter to hole length decreases. However, from Equ. 1.1 it can be seen that detection efficiency decreases approximately as the square of the ratio of hole diameter to hole length, $(d/l)^2$. Thus an approximate square relationship between collimator efficiency and collimator resolution exists. Improving the collimator resolution by a factor of 2 will reduce efficiency by a factor of 4. This inverse square relationship compromises collimator performance and results in collimators with $10-12$mm FWHM resolution at 10cm with a detection efficiency of less than 1% at 140keV. System spatial resolution of a gamma camera is determined in terms of collimator resolution, R_c, and intrinsic camera resolution, R_i, as given by [Hut07]:

$$R_s = \sqrt{R_i^2 + R_c^2} \tag{1.3}$$

For typical organ depths inside the human body (5-10cm), the system resolution is dominated by collimator resolution rather than intrinsic camera resolution. Furthermore, at

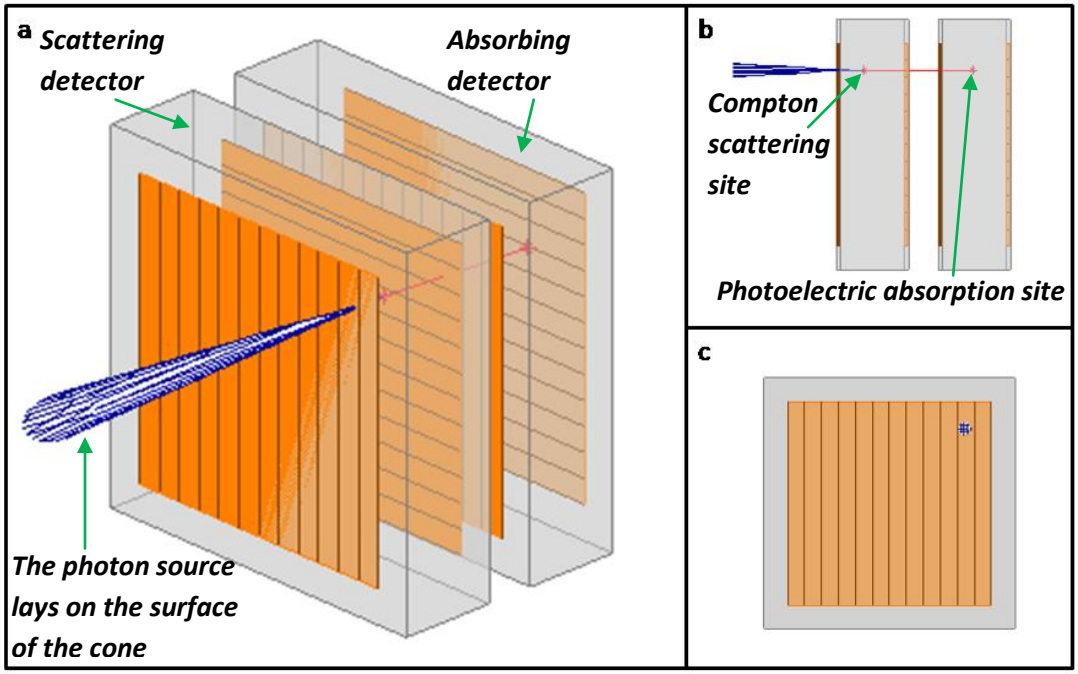

Figure 1.2: Schematic of the SmartPET detectors in Compton camera configuration. The orthogonal electrode segmentation can be seen in image (a). A photon scatters from a site in the first detector and then deposits its remaining energy at a site in the second detector. According to Compton kinematics the energy and locations of these interactions then define a cone, the coordinates of which are possible solutions for the location of the emissive radioactive source.

higher energies a thicker collimator is required which further reduces sensitivity. A better design is clearly required if these performance limitations are to be overcome. Many methods have been proposed to increase sensitivity whilst maintaining a constant spatial resolution, or improving resolution without a loss of sensitivity. Expanding the detector area, or using ring geometries are just some suggestions. However, collimator removal is fundamentally advantageous.

1.3 Electronic Collimation

An alternative method to mechanical collimation in nuclear medicine was first suggested by Todd [Tod74]. However, no imaging system was able to provide the originally anticipated increase in sensitivity. Only recent developments in the manufacture of three dimensionally sensitive semiconductor detectors and the necessarily fast digital electronics provide the basis to realise the envisioned imaging system. The original proposal was to exploit Compton kinematics so that if two interactions occurred in separate detectors, the energies and locations of these interactions would be measured. It would then be possible to

calculate the angle of incidence of the original photon. This method of using two detectors is now commonly known as a traditional Compton camera. Sophisticated software can be applied to more advanced methods [Wul03][Kro00] but the basic apparatus can be seen in Fig. 1.2. The detectors used for this research are high purity orthogonal strip planar germanium detectors. Excellent energy resolution and digital data acquisition allows significantly improved interaction position resolution. Signal analysis and processing techniques replace the mechanical collimators to improve system sensitivity. Unprecedented sensitivities in nuclear medicine are expected at high energies.

1.4 Thesis Synopsis

The essential requirements of a Compton camera are excellent energy and (interaction) spatial resolution. The required methodology is presented in this thesis and covers three major areas: the assembly of a traditional Compton camera, development of advanced pulse-shape analysis techniques to extract energy and interaction information from experimental data, and the development of an analytical Compton camera imaging code. This thesis is organised across seven chapters to entirely describe and expand on the work performed, with each chapter having its own introductory paragraph.

Chapter 1 has fully explained the motivation and aims of this thesis. Physical limitations of current nuclear medicine systems have been explored and an alternative method has been proposed, which performs collimation with software. Chapter 2 covers the background of semiconductor based radiation detection, which is important and applicable to the remaining work. Chapter 3 discusses the actual system developed for the SmartPET project and details an experiment which was conducted to qualify pulse shape analysis. This experiment is analysed in chapter 4 in which the response of the detector is explored and a basis data set is constructed for depth of interaction information. Chapter 5 details new digital signal processing techniques which can be used to analyse data and identify Compton scattering in single detector ‘pixels’. An analytical imaging code is developed and validated with Geant4 simulation data in chapter 6. This imaging code is then used to reconstruct real sources. Chapter 7 is a discussion of the salient points of this thesis and contains suggestions for the future direction of the project.

Chapter 2

Principles of Radiation Detection

Energy and spatial resolution are the paramount components of Compton camera performance. Poor experimental geometry and large scattering angles are peripheral factors which will ultimately cause image-quality degradation, but these factors are not necessarily a fundamental consideration in system design. It is possible to account for poor geometry whilst analysis software can be used to exclude large scattering angles, the practicalities of which are discussed in chapter 6. Excellent energy and spatial resolution must be inherent detector properties from which image reconstruction is derived from the analysis of simple signals. However, signal generation is not so trivial and a careful consideration of the detector material should be made to optimise the attainable resolutions. Essentially, energy resolution is proportional to the number of charge carriers which constitute the signal, and spatial resolution requires a characteristic response from spatially disparate interactions, permitting an intelligible estimation of the interaction location. Therefore, a comprehensive description of the physical processes which govern signal generation is given in this chapter, supporting the analysis in subsequent chapters. The choice of germanium based on its attributes is well justified, and the advantage of using pulse shape analysis is described.

2.1 Interaction of Radiation with Matter

Charge carriers must first be liberated prior to any signal analysis. Nine principal mechanisms compete, each with various probabilities over a range of energies and atomic numbers. However, only three primary interactions are of interest for the energies used in

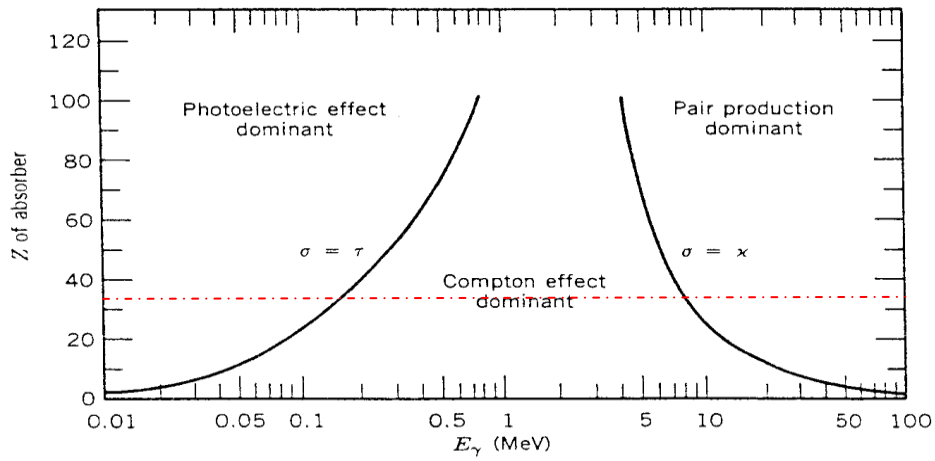

Figure 2.1: Relative importance of the three interaction mechanisms of interest. Red line indicates atomic number of germanium for which scattering is dominant above 150keV [Kno00].

this thesis. Once a charge carrier is liberated it can be directly detected or the secondary effects of its liberation can be detected. However, it is inescapable that a charge carrier must be initially liberated, and liberation is appropriately the only point of interest in this subsection. The three mechanisms of interest are photoelectric absorption, Compton scattering and pair production, all of which result in an at least one electron capable of constituting a basic electrical signal. The importance of each interaction in the energy range 0-100MeV for a range of atomic numbers is shown in Fig. 2.1. The total cross section can be used to describe photon ranges in materials. The total cross section of interaction is given by the sum of the individual cross sections; photoelectric, σ_{ph}, Compton, σ_{Comp}, and pair production, σ_{pair} :

$$\sigma_{tot} = \sigma_{ph} + \sigma_{Comp} + \sigma_{pair} \tag{2.1}$$

The linear attenuation coefficient, μ, represents the probability for an interaction per unit length and is proportional to the density of atoms, N. This can then be represented in terms of Avogadro's number, N_a, material density, ρ, and the molecular mass, A.

$$\mu = N\sigma_{tot} = \left(\frac{N_a \rho}{A}\right)\sigma_{tot} \tag{2.2}$$

The intensity, I, of photons transmitted through thickness, x, of a material is then given by:

$$I = I_0 e^{-\mu x} \tag{2.3}$$

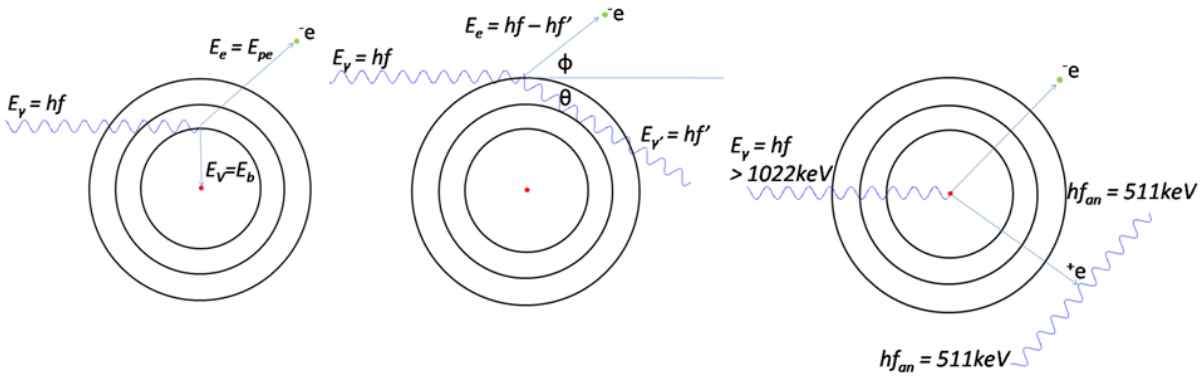

Figure 2.2: Schematic representation of the three principle interaction mechanisms presented in the following order: photoelectric effect, Compton scattering and pair production.

where I_0 is the initial intensity incident on the material.

The mean free path, λ, is defined as the average distance between two interaction points and is simply the reciprocal of the linear attenuation coefficient.

$$\lambda = \frac{1}{\mu} \tag{2.4}$$

Typical values of μ in germanium range from a few millimetres to a few centimetres. The photon energy 662keV is of particular importance in this thesis, for which the mean free path in germanium can be calculated as 23mm.

2.1.1 Photoelectric Effect

It can be seen in Fig. 2.1 that the photoelectric effect is the dominant process in germanium below 150keV. A gamma ray enters the Coulomb field of an atom and transfers its entire energy to a bound electron causing ionisation. The electron is subsequently ejected from the atom with a kinetic energy, E_{pe}, equal to the sum of the difference between the gamma ray energy and the binding energy of the ejected photoelectron.

$$E_{pe} = hf - E_b \tag{2.5}$$

where E_b is the binding energy of the photoelectron and hf is the quantised energy of the incident photon. The ejection is most likely to originate from the atomic K-shell, leaving a

vacancy which is filled by an electron from a lower shell, resulting in the emission of characteristic X-rays. Coulomb's law requires that the photoelectron interacts with all surrounding charges leading to tortuous tracks and the production of delta radiation along this track. The cross section for photoelectric effect can be calculated as a function of atomic number and photon energy [Dav65].

$$\sigma_{ph} \approx constant \times \frac{Z^n}{E^{\sim 3}} \tag{2.6}$$

where n is a number between 4 and 5. Therefore, higher atomic numbers have larger cross sections for photoelectric effect, whilst the photoelectric cross section decreases with increasing photon energy. This effect can be seen in Fig. 2.1.

2.1.2 Compton Scattering

Compton scattering is undoubtedly the most important interaction in this thesis. Not only is it used for imaging purposes in chapter 6 but also indirectly for spatial calibrations in chapter 4. It is also highly significant to the work presented in chapter 5. Compton scattering is the predominant interaction in germanium for gamma rays in the energy range of 150keV - 8MeV. A photon transfers a fraction of its initial energy to a loosely bound electron. The binding energy is usually negligible compared with the photon energy and as such it is usually neglected. The electron is 'knocked' free resulting in a recoil electron and the incident photon is scattered through an angle, θ, between 0^o and 180^o with respect to its original direction. Conservation of linear momentum and energy leads to an expression [Kra88] for the energy of the scattered photon, hf'.

$$hf' = \frac{hf}{1 + \frac{hf}{m_0 c^2}(1 - \cos\theta)} \tag{2.7}$$

where hf is the initial photon energy and $m_0 c^2$ is the rest mass energy of the electron (511keV). Since all scattering angles are possible, the energy given to an electron can range from zero up to a maximum value, for which the photon is backscattered through 180^o. This fundamental equation is the basis of the Compton camera and is recast in terms of the recoil electron energy deposited in the scatter detector and the photoelectron energy

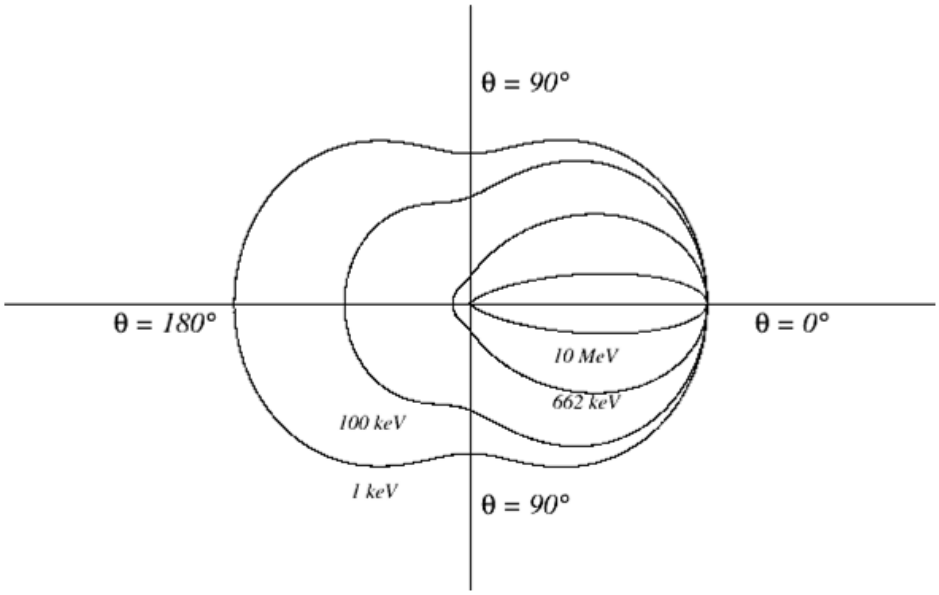

Figure 2.3: The Klein-Nishina angular distribution plot which shows that forward scattering is the most probable scattering angle at high energies, whilst backscattering is equally as probable at low energies.

deposited in the absorber detector. The electron is still considered free even if the scatter occurs from a tightly bound K-shell electron provided that the gamma-ray energy exceeds 300keV [Sur92]. Therefore, scattering angles can be defined with good spatial and energy resolution of the original recoil electron site and the final interaction site. However, the temporal resolution of the interaction sequence is not well known and it is impossible to analytically calculate which interaction occurred first. Gamma-ray tracking uses the angular distribution of the scattered gamma rays as given by the Klein-Nishina formula. Sequencing can thus proceed on a statistical basis. This has been demonstrated on simulated data and partially reproduced on real data with promising results [Pea02], with gamma-ray tracks successfully disentangled. Recently it [Ham05] has been shown that gamma-ray tracking cannot always reconstruct the gamma-ray path, but that this ambiguity is only for a small fraction of events. The Klein-Nishina formula [Kle42] is given by: (2.8)

$$\frac{d\sigma}{d\Omega} = Zr_0^2 \left(\frac{1}{1+\alpha(1-\cos\theta)}\right)^2 \left(\frac{1+cos^2\theta}{2}\right)\left(1+\frac{\alpha^2(1-\cos\theta)^2}{(1+cos^2\theta)[1+\alpha(1-\cos\theta)]}\right)$$

where $\alpha = E_\gamma / m_0c^2$ and r_0 is the classical electron radius. The Klein-Nishina distribution is plotted in Fig. 2.3, and special attention should be drawn towards the distribution for 662keV because the isotope ^{137}Cs was intensively used throughout this research. At this

energy forward scattering is most probable, knowledge of which permits a simply method of applying the principles of gamma-ray tracking to the Compton camera of chapter 6.

2.1.3 Pair Production

Providing the incident photon has at least twice the rest mass energy of an electron, the photon may disappear in the presence of the Coulomb field of a nucleus and be replaced by an electron-positron pair. Any excess energy above 1022keV is carried away as kinetic energy by the electron-positron pair. Conservation of energy is shown in Equation 2.9.

$$E_\gamma = T_p + m_p c^2 + T_e + m_e c^2 \tag{2.9}$$

where T_p is the kinetic energy of the positron, $m_p c^2$ is the rest mass energy of the position, T_e is the kinetic energy of the electron and $m_e c^2$ is the rest mass energy of the electron. The positron will annihilate after slowing down in the absorbing medium, usually resulting in two annihilation photons. Due to conservation of momentum these particular annihilation photons will be back-to-back and can be used for PET. This is shown schematically in Fig. 2.2.

2.2 Charge Cloud Formation

Electrons liberated via the mechanisms presented in the previous section lose energy in the field of other charges immediately after production. The total linear stopping power is a combination of energy losses through impact ionisation and Bremsstrahlung.

$$-\left(\frac{dE}{dx}\right)_{tot} = -\left(\frac{dE}{dx}\right)_{coll} - \left(\frac{dE}{dx}\right)_{rad} \tag{2.10}$$

Where the subscripts tot, $coll$, and rad represent total, collision and Bremsstrahlung respectively. The energy loss by impact ionisation is dominant for energies below a few MeV and is given by the Bethe-Bloch formula [Leo94]:

$$-\left(\frac{dE}{dx}\right)_{coll} = 2\pi N_a r_0^2 m_e c^2 \rho \frac{Z}{A}\frac{1}{\beta^2}\left[ln\frac{\tau^2(\tau+2)}{2\left(\frac{I}{m_e c^2}\right)^2} + P(\tau) - \delta - 2\frac{C}{Z}\right] \quad (2.11)$$

where N_a is Avogadro's number, r_0 is the classical electron radius, ρ, Z, and A are the density, atomic number and atomic mass of the absorbing material respectively; β is v/c of the incident electron, τ is the kinetic energy of the incident electron. δ and C are factors accounting for density and shell corrections. $P(\tau)$ is a function of the energy of the incident electron. Finally, I represents the average excitation and ionisation potential of the absorber. Bremsstrahlung losses become comparable with collision ionisation for high-energy electrons above a few MeV and is given by [Leo94]:

$$-\left(\frac{dE}{dx}\right)_{rad} = NE_0 4Z^2 r_e^2 \alpha\left(ln\frac{2E_0}{m_e c^2} - \frac{1}{3} - f(Z)\right) \quad (2.12)$$

where N is the atomic density in atoms/cm^3, α is the fine structure constant, E_0 is the initial energy of the electron and $f(Z)$ is a correction factor accounting for the Coulomb attraction due to the nucleus. Bremsstrahlung radiation is clearly capable of interacting via the processes described in the earlier section. However, energy loss through Bremsstrahlung represents only 5% energy loss at 1MeV.

Photoelectron energy is ultimately lost by the creation of electron-hole pairs. The number of electron-hole pairs created, $\overline{N}_{pair}$, for a given electron energy, E, is clearly proportional to the average ionisation energy of the detector material, $\in_{pair}$.

$$\overline{N}_{pair} = \frac{E}{\in_{pair}} \quad (2.13)$$

It is necessary to use average ionisation energies to account for a partial transfer of energy from the electron to lattice vibrations. The process of electron-hole pair production is not independent because the production of creating one electron-hole pair affects the probability of another electron-hole pair being created. It cannot be described by Poisson statistics. The Fano factor, F, is introduced as a correction parameter for the statistical variance of the number of charge carriers for a given interaction energy:

$$\sigma_{\bar{N}_{pair}} = \sqrt{F\bar{N}_{pair}} \tag{2.14}$$

The Fano factor for germanium at 77K is reported as 0.129 [Bil67]. If the entire kinetic energy of the electron were always converted into charge carriers, the number of charge carriers produced would always be exactly the same for a given energy and no statistical variance would occur. Therefore, an ideal detector would have a zero Fano factor. Crucially, germanium does have a small Fano factor compared with other detection materials.

Property	Germanium	Silicon	NaI(Tl)
Atomic Number	32	14	50 (effective)
Crystalline Structure	Diamond	Diamond	N/A
Lattice Constant	5.658Å	5.43Å	N/A
Intrinsic Carrier Density	$2.4 \times 10^{13}\,\mathrm{cm}^{-3}$	$1.45 \times 10^{10}\,\mathrm{cm}^{-3}$	N/A
Energy Gap (T = 300K)	0.67eV	1.12eV	N/A
Energy Gap (T = 0K)	0.75eV	1.17eV	N/A
Ionisation Energy	2.96eV	3.72eV	$\sim$100eV
Fano Factor	0.129	N/A	1
Dielectric Constant	16	N/A	N/A

Table 2.1: A selection of important physical properties for possible radiation detection media taken from [IOFFE].

2.3 Detection Medium

In reference to equation 2.7, it should come as no surprise that the optimal detection material for a Compton camera must have good energy and spatial resolution. However, this prerequisite does not restrict choice to a single detector material. Indeed, the scattering and absorbing detectors serve disparate purposes. From consideration of the interaction mechanisms shown in section 2.1 it can be seen that for a given energy, materials with lower atomic numbers will have a lower cross-section for photoelectric effect and a higher cross-section for Compton scattering. A full description of the ideal Compton camera is postponed until chapter 6, but a dual-material camera based on SmartPET is currently being

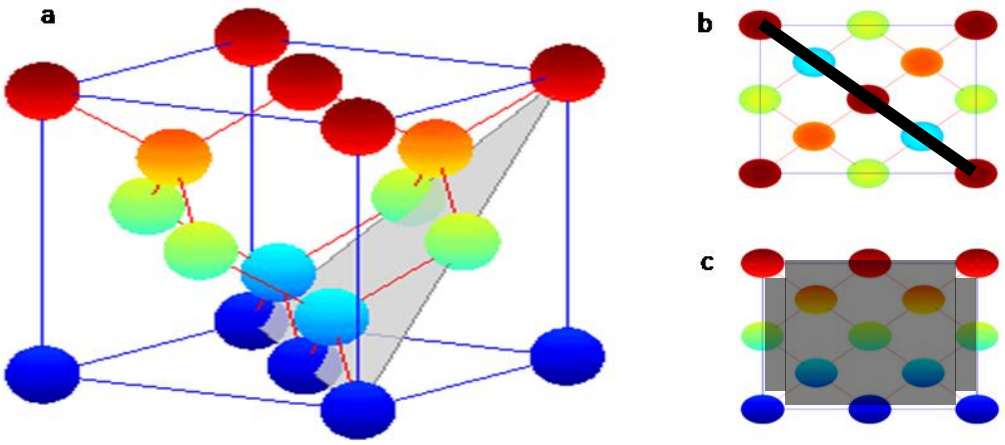

Figure 2.4: Diamond lattice unit cell composed of 8 atoms (only portions inside the blue 'frame' contribute to the total number of atoms inside the cell). All red lines indicate a covalent bond. Image b) and image c) show side views of the model. The (111) plane is shown in grey in image (a), the black line in image b) indicates the (110) plane, and (100) plane is displayed in grey in image (c). The crystal directions [100], [110] and [111] can be visualised as unit vectors normal to the plane surfaces.

investigated [Gri07]. Dual material cameras do exist, the self-named Advanced Compton Camera (ACC) has been constructed and tested [Tan06], achieving an angular FWHM of 6^{o} at 364keV. This camera is an amalgamation of gaseous detectors and scintillators. Gaseous detectors have low efficiency. To avoid low efficiency SmartPET is based upon the use of solid state detectors, exclusively in the form of semiconductors. Although scintillators can have higher atomic numbers and therefore higher efficiency, they have larger average ionisation energies of ~100keV (see Tab. 2.1) and larger Fano factors, resulting in fewer charge carriers and bigger statistical variances. Semiconductors have much smaller ionisation energies and Fano factors, and therefore superior energy resolution. The band theory of solids can be used to explain the small ionisation energies of semiconductors.

2.4 Semiconductors

Germanium has been utilised for SmartPET because it has a high atomic number and a small band gap compared with silicon. Both materials are elemental semiconductors. Compound semiconductors are finding applications in nuclear physics but are harder to grow and not readily available in appropriate bulk sizes. Unit cells can be used to describe the structure of crystalline germanium. Consecutive unit cells are built upon each other to form the bulk material or crystal lattice. A diamond lattice characterises both silicon and germanium and is

shown in Fig. 2.4. Individual atoms have four valence electrons which bond with their nearest neighbours. Germanium has 8 atoms per unit cell and a lattice constant of 5.658Å. Therefore, a single SmartPET crystal has $\sim 3.18 \times 10^{24}$ atoms or an atomic density of $\sim 4.42 \times 10^{22}\,\text{cm}^{-3}$. The atom is a quantised system in which electrons have discrete energies, bringing successive atoms together requires that electrons are shared suggesting that the actual energy-levels themselves are shared. Without degeneracy, electrons corresponding to the energy-level of one atom would sit in the equivalent energy-level of another atom, and the system as a whole would not obey the Pauli exclusion principle. However, energy-levels subdivide so that no two electrons share the same level. So for *N* atoms in a bulk material, it is found that each distinct energy-level is split into *N* slightly different energy-levels. The splitting is so infinitesimally small that one can think of bands of energy levels in which electrons are permitted to exist, separated by a forbidden region. Only valence bands and the first conduction band are of any significance for charge transport purposes. The energy spread of a 'band' is ~1eV or less [Par04]. Therefore, separation between individual atomic levels in a single band in a SmartPET crystal is $\sim 3.14 \times 10^{-25}$ eV or less, which is indeed a pseudo continuous band.

2.4.1 Density of States

A crystal constructed entirely of multiples of the unit cell of Fig. 2.4 would represent an intrinsic semiconductor. The crystal would be exclusively composed of a single element or compound without impurities. The breaking of a bond constitutes promoting an electron into the conduction band in which the electron is free to migrate around the lattice as a charge carrier. Conversely, a hole is left behind and this effectively wanders through the lattice as neighbouring electrons fill the hole leaving another hole in their place. Thus every electron in the conduction band corresponds to a hole in the valence band and the density of conduction electrons, n, is equivalent to the density of holes, p.

$$n = p = n_i \tag{2.15}$$

The number of allowed states in each band is simply four times the number of atoms in the crystal. However, the energy distribution of allowed states, which determines the number of

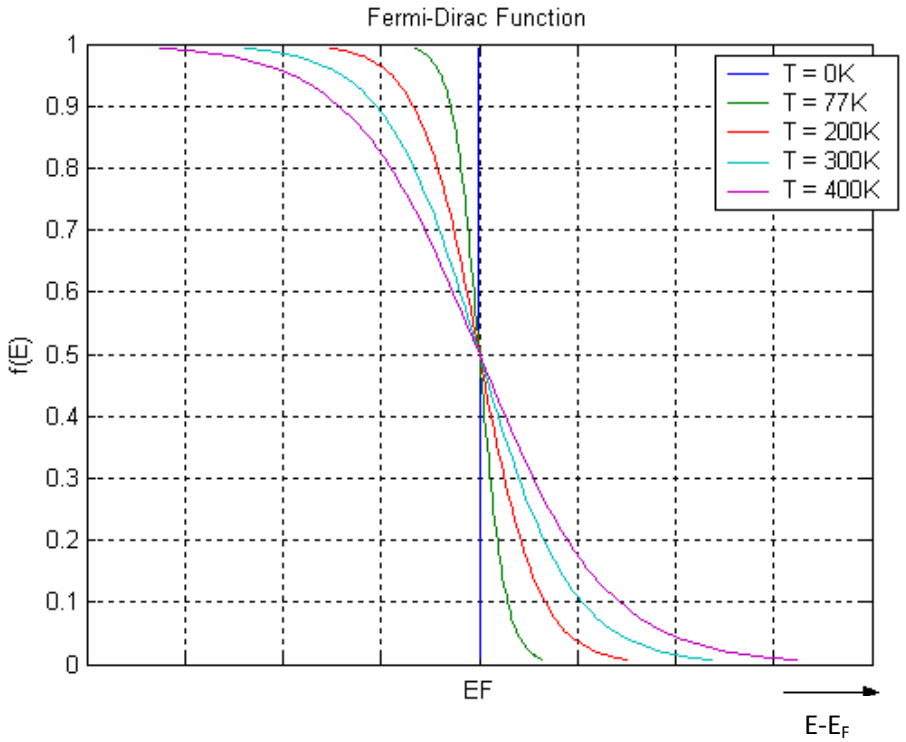

Figure 2.5: Fermi-Dirac function for 5 different temperatures. These simply give the probability that an available state at an energy *E* will be occupied by an electron as a function of temperature.

states to be found at any given energy, is not so trivial. After quantum mechanical considerations, the density of states in the conduction band, g_c, and the valence band, g_v, are given by [Col06]:

$$g_c(E) = \frac{m_n^* \sqrt{2m_n^*(E - E_c)}}{\pi^2 \hbar^3} \tag{2.16}$$

$$g_v(E) = \frac{m_p^* \sqrt{2m_p^*(E_v - E)}}{\pi^2 \hbar^3} \tag{2.17}$$

where E is an energy in the conduction or valence band for which the density of states are calculated, $m_{n,p}^*$ is the effective mass of the electron or hole, and $E_{c,v}$ are boundary energies in between which the forbidden region exists. By inspection it follows $g_c(E)$ is zero at E_c and increases as the square root of energy when energy increases in the conduction band.

The density of states specifies how many states exist at a given energy, E, whilst the Fermi-Dirac function, $f(E)$, specifies how many states at E will be filled with an electron.

$$f(E) = \frac{1}{1 + e^{(E-E_F)/kT}} \tag{2.18}$$

where E_F is the Fermi energy, k is the Boltzmann constant and T is temperature. It is possible to show that the Fermi-level is positioned mid point between the conduction and valence bands for an intrinsic semiconductor. Fig. 2.5 is a plot of the Fermi-Dirac function for a range of energies and temperatures. Essentially, the Fermi-Dirac function indicates that at T = 0 all states below E_F will be occupied. It also shows that for an incremental energy above the Fermi-level, the probability that an electron can exist is greatly affected by temperature. For SmartPET operating at temperatures approaching 77K the most probable occupied state is below the Fermi-level. Hence one can expect very few electrons to exist in the conduction band. Since g_c represents the number of conduction band states and $f(E)$ specifies the probability that an available state will be occupied, then it follows that the electron density, n, in an energy band can be calculated by integrating the product of the occupation probability by the density of states [Mar02].

$$n = \int_{E_c}^{\infty} g_c(E) f(E) dE = N_c e^{(E_F - E_c)/kT} \tag{2.19}$$

Similarly,

$$p = \int_{-\infty}^{E_v} g_v(E)[1 - f(E)] dE = N_v e^{(E_v - E_F)/kT} \tag{2.20}$$

where $N_{c,v}$ is the effective density of states in the conduction or valence band. The charge carrier densities can be drastically changed by doping the semiconductor with impurities. Impurities are either valence five atoms or valence three atoms. Therefore, impurities donate electrons to the conduction band or accept them from the valence band. Semiconductors doped with donor impurities are known as n-type, whilst semiconductors doped with acceptor impurities are known as p-type. Energy levels inside the forbidden region are now available. Impurity concentrations are denoted $N_{A,D}$.

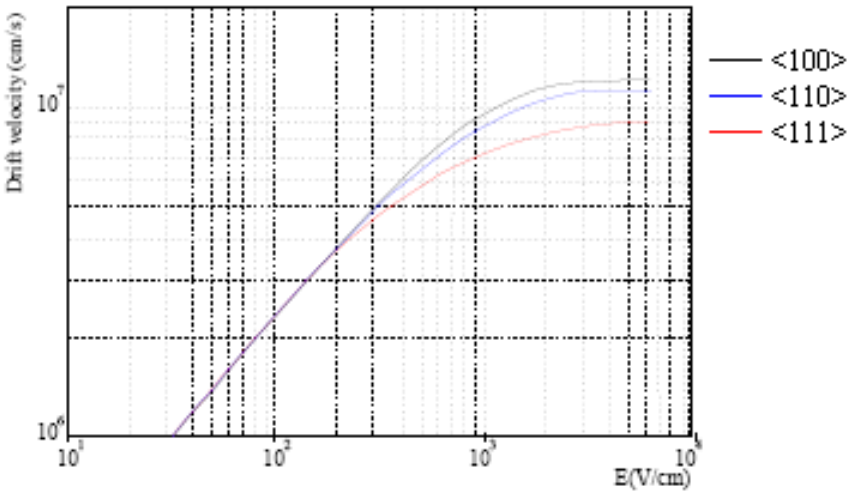

Figure 2.6: Experimental field dependences of the electron drift velocity along different equivalent directions. Image was taken from [Tur06].

2.4.2 Effective Mass

Liberated electrons quickly recombine giving rise to the concept of a *mean life-time*. Spectroscopic studies require the collection of conduction band electrons and thus an electric field is applied to quickly collect these charge carriers. However, an electron moving through a lattice will interact with every potential along its trajectory. The crystal direction [100] has the fewest potential sites along a given track and hence this trajectory has the least effect on the particles' motion. Because the force exerted on an electron by a collection of periodic potentials in the lattice is very much different to that of a free electron model, the concept of effect mass is introduced. The time-independent Schrödinger equation leads to a relationship for effective mass, were each atom acts as a source of potential.

$$-\frac{\hbar^2}{2m^*}\frac{d^2\psi(x)}{dx^2} + V(x)\psi(x) = E\psi(x) \tag{2.21}$$

where m^* is the effective mass, x is a displacement in potential V and E is the particles' energy.

The solution to equation 2.21 is a wave equation which results in an expression for the wavenumber, k. This expression is usually rearranged in terms of particle energy, E:

$$E = \frac{\hbar^2 k^2}{2m^*} \tag{2.22}$$

It should be noted that a perfectly periodic potential field (zero lattice vibrations) will provide no resistance. It is only when the lattice vibrates that the electrons' motion through a lattice is of concern. Equation 2.22 can be used to plot energy-momentum graphs. When this is plotted for germanium it is found that germanium is an indirect band semiconductor. This simply implies than a change in particle energy firstly requires a change in particle momentum. The significance of this is that photons are not produced by a drop in particle energy alone. Because each crystal orientation has different characteristics the resulting conductivity of germanium is anisotropic. Therefore, drift velocity is highly dependent on crystallographic directions. The maximum drift velocity is unsurprisingly along the $\langle 100 \rangle$ equivalent crystal direction. The drift velocity of each crystallographic direction is plotted as a function of applied electric field in Fig. 2.6. Collection times will have an effect on the pulse shape of observed detector signals. Saturation drift velocities are reached for fields in excess of $\sim 10^3\,\mathrm{V/cm}$. SmartPET has been cut along the (100) crystal plane to minimise charge collection times.

2.4.3 p-n Junction

Semiconductor radiation detectors are in principle equivalent to a common two-terminal photodiode. They are fundamentally based on the physical characteristics of a p-n junction. An idealised view of this junction is to consider two regions of differing dopant concentrations being brought into contact. The transition from one plane to another is perfectly sharp, occurring at a single junction plane. Electrons diffuse from the n-type semiconductor to holes in the p-type semiconductor. Similarly, holes from the p-type semiconductor diffuse across the junction to combine with electrons in the n-type semiconductor. This migration of charge carriers from their original locations leaves behind an uncovered space-charge region; this region is depleted of free charge carriers and is thus known as the depletion region. Eventually, the depletion region constitutes an electric field due to the remaining fixed charges. The direction of the electric field inhibits the diffusion of charge carriers until equilibrium is reached. The equilibrium situation is shown in Fig 2.7.

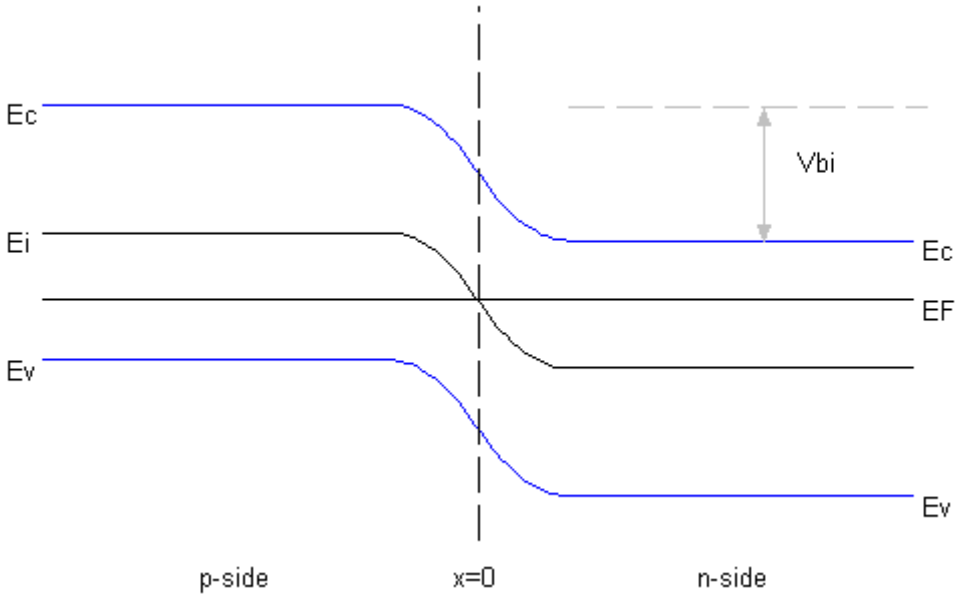

Figure 2.7: Simulation of p-n junction energy diagram at equilibrium. Semiconductor simulated at T = 300K with acceptor and donor impurities of $10^{14}cm^{-3}$, and a dielectric constant of 16 (Ge). Electrons encounter a voltage drop across the depletion region V_{bi} calculated as 0.6V under these conditions.

Electrons in the n-type semiconductor encounter a built-in potential, V_{bi}, which prevents diffusion across to the p-type material. The characteristic of the potential difference is determined by obtaining quantitative solutions of the Poisson equation. In one-dimensional problems the Poisson equation simplifies to:

$$\frac{d^2V(x)}{dx^2} = -\frac{\rho(x)}{K_s\varepsilon_0} \tag{2.23}$$

where ρ is the charge density, K_s is the semiconductor dielectric and ε_0 is the permittivity of free space. Overall space-charge neutrality gives:

$$N_A x_p = N_D x_n$$

where x_p and x_n are the extents of the depletion region in the two sides of the junction and $N_{A,D}$ are the impurity concentrations. Solutions for the Poisson equation are possible by considering each side of the junction individually and using the boundary conditions:

$$V_p(-x_p) = -\frac{qN_A x_p^2}{2K_s\varepsilon_0} \tag{2.24}$$

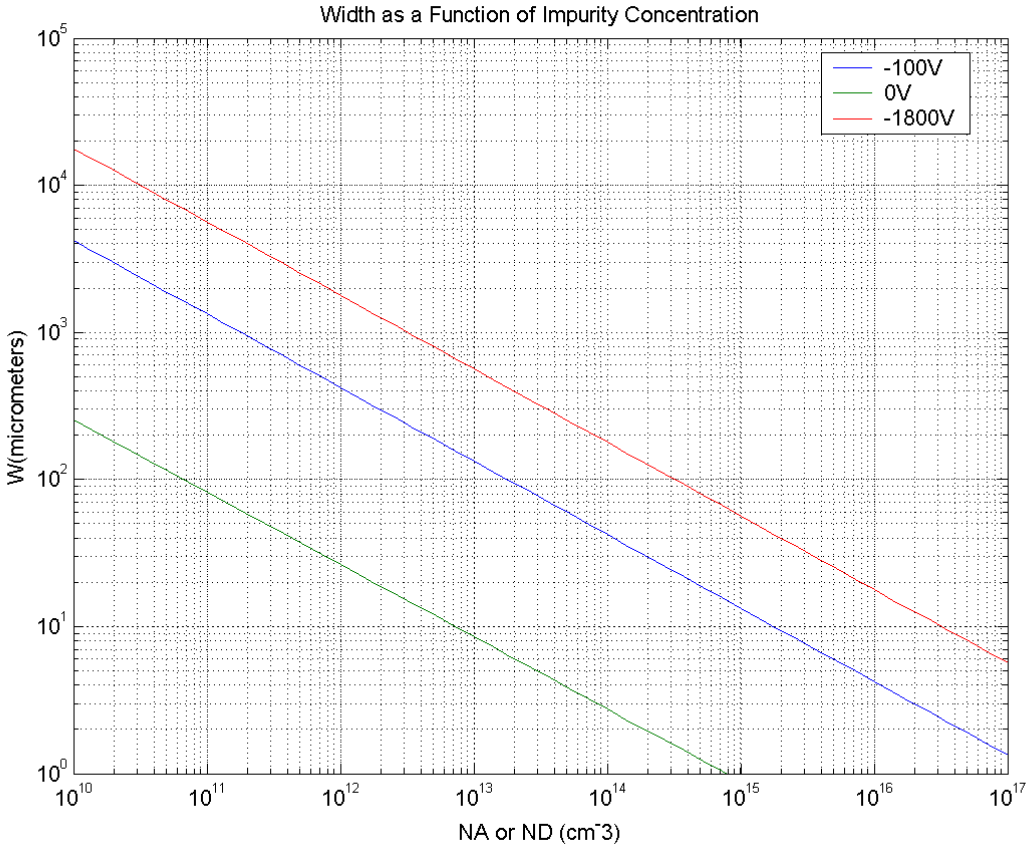

Figure 2.8: Depletion region width as a function of impurity concentration (NA or ND) for a range of applied potentials. SmartPET is operated at -1800V and is shown in red.

$$V_n(x_n) = \frac{qN_D x_n^2}{2K_s\varepsilon_0} \tag{2.25}$$

The total potential difference across the whole junction is just the built-in voltage and therefore:

$$V_{bi} = V_n - V_p = \frac{q}{2K_s\varepsilon_0}\left(N_A x_p^2 + N_D x_n^2\right) \tag{2.26}$$

Rearrangement of this equation allows expressions for x_n and x_p to be derived in terms of the built-in voltage. This voltage sweeps electrons or holes out of the depletion region. However, because charge carriers recombine over time it is necessary to apply an external reverse bias across the junction. The application of an external electric field in reverse bias is effectively the application of a potential across the depletion region because of the much higher resistivity in the depletion region. For higher applied potentials the width of the depletion region is increased, leading to an increased volume [Col06].

$$W = \left[\frac{2K_s\varepsilon_0}{q}\left(\frac{N_A + N_D}{N_A N_D}\right)(V_{bi} - V_A)\right]^{1/2} \quad (2.27)$$

where W is the width of the depletion region and V_A is the applied potential. Fig. 2.8 shows the depletion width as a function of doping for various applied potentials. For SmartPET to have a 20mm depletion width at -1800V the impurity concentration is $\sim 10^{10}\,\mathrm{cm}^{-3}$.

2.5 Semiconductor Detection Practicalities

The response of a semiconductor detection system to a photonic interaction is the generation of a number of charge carriers. Swept out of the depletion region by the application of an external electric field, the motion of these charge carriers constitutes current that flows for a time that is equal to the charge collection time. This should be as short as possible to prevent recombination. Ideally, the signal is proportional to the incident radiation energy and a counting system can be used to collect useful information from the radiation field. A number of considerations must be made to fully appreciate the practical operation of a semiconductor-based radiation detection counting system. The subsequent analysis of signals, which can be used to extract energy and spatial information regarding to individual interactions, is based upon analysis of the signals resulting from the system as an entity, in which the signals are processed at various stages.

2.5.1 Detector Geometry

Depletion regions of a few centimetres thick are required to detect highly-penetrating gamma rays. Standard germanium has impurity concentrations of $10^{15}\,\mathrm{cm}^{-3}$, which in reference to Fig. 2.8 will not provide a sufficiently thick depletion region under an applied potential of -1800V. Reference to equation 2.27 indicates that depletion thickness is inversely proportional to the impurity concentration. Impurity concentrations have to be greatly reduced for large depletion regions. The fabrication of a photodiode for gamma-ray detection requires refining techniques which approach impurity concentrations of $\sim 10^{10}\,\mathrm{cm}^{-3}$. A germanium crystal with this impurity is otherwise known as hyper-pure

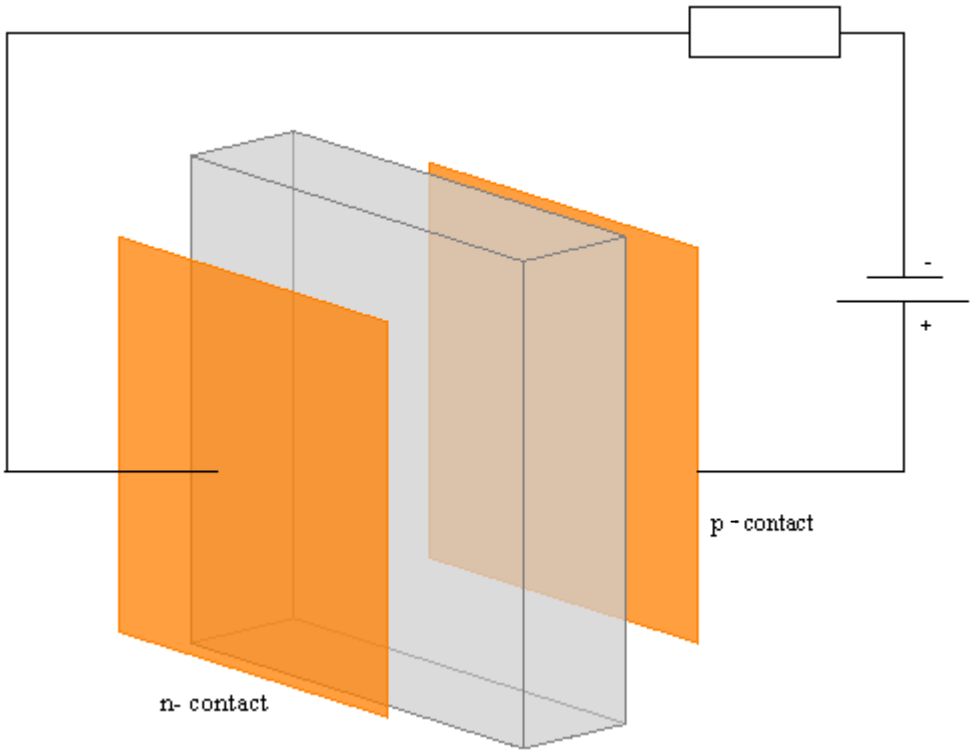

Figure 2.9: Schematic of a SmartPET crystal. The hyper-pure crystal is shown in grey. Electrodes are implanted with slight impurities so that a depletion region is established. The depletion region is then increased by an applied potential as shown. This is the simplest detector geometry that can be fabricated.

germanium. With such refinement it is possible to achieve depletion widths of $\sim 2\mathrm{cm}$ as shown in Fig. 2.8. The simplest detector geometry is that of a planar configuration as shown in Fig. 2.9. A hyper-pure crystal sits between two electrodes. The electrode contacts are commonly made by doping the crystal through boron implantation, for the p-type contact and through lithium drifting for the n-type contact. The actual contact specifications for SmartPET are proprietary and the contact compositions are not freely available. However, contact thicknesses for SmartPET are specified; $0.3\mu\mathrm{m}$ is quoted for the p-type and $50\mu\mathrm{m}$ is quoted for the n-type. A small built-in potential is created between one contact and the oppositely doped junction. The depletion region is then increased by the application of external potential. High voltage NIM units are used which transform AC mains into DC potential with typical magnitudes of between 0-5000V. The detector forms part of a circuit with the detection system so that liberated charge carriers can be collected.

2.5.2 Signal Generation Process

A collection of charge carriers drifting through the crystal under the influence of an external electric field represents a net induced current in the detection material. This then induces a time-dependent charge on a collecting electrode. The electrostatic field at a point resulting from a charge distribution can be calculated by a triple integration over the entire distribution. This is an intractable numerical problem and it is easier to solve a numerically differential equation in the form of Gauss's law [He01]:

$$\oint \boldsymbol{E}.d\boldsymbol{S} = \frac{Q}{\varepsilon} \tag{2.28}$$

where, $\boldsymbol{E}$ is the electrostatic flux through small surface element $d\boldsymbol{S}$, Q is the total charge inside the closed surface and ε is the dielectric constant of the medium in which the charge is located. Using Gauss's law is an unattractive proposal for a calculation of the induced charge on an electrode due to charges in transit. Prior knowledge of the electrostatic field at a large number of discrete points internally to the detection medium along the trajectory of the charge carriers is required. A simpler method of calculating the induced current on an electrode has been developed [Ram39]. Ramo emphasises a change of state in which a charge is enclosed between two electrodes. Firstly, the electrodes are grounded and a tiny equipotential sphere is placed around the charge, the state of this system is determined with a Laplacian operator and Gauss's law. Secondly, the charge is removed and one electrode is set to unit electrostatic potential. The relationship of potentials and charges for the two states is defined by Green's theorem. Both states are equated and after substitution the final equation can be derived as follows [Sho38].

$$0 = -\int_{SA} \frac{\partial V}{\partial n} ds - V_{e'} \int_{SS} \frac{\partial V'}{\partial n} ds \tag{2.29}$$

where the differentials indicate differentiation of the electrostatic potential with respect to the outward normal of the equipotential sphere, primes are used to denote the change of state and $V_{e'}$ is simply the potential at the point in which the electron was placed. These two equations both represent Gauss's law for a change of state, but crucially they can be simplified in terms of charge, current, drift velocity and electrostatic weighting field. The

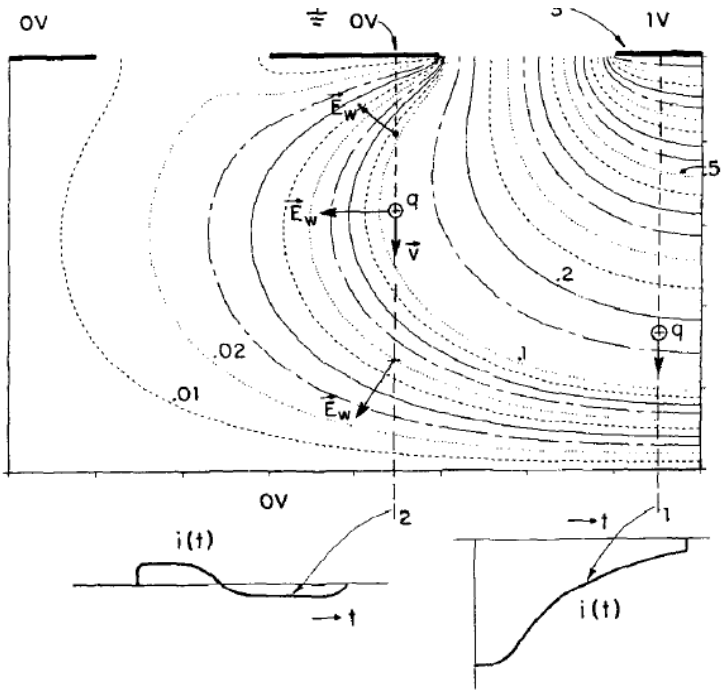

Figure 2.10: The weighting field concept utilised for spatial resolution in photodiodes as a plot of equipotential lines [Rad88]. Two examples of charge transit are shown. The resulting induced current waveforms, resulting from equation 2.32 are shown at the bottom of the plot.

weighting field is used to couple a moving charge to a sensing electrode and is conceptual in its derivation. Solving equation 2.29 and dividing through by surface area gives:

$$Q_A = -eV_{e'} \tag{2.30}$$

where Q_A is the charge induced on the electrode, e is the charge associated with an electron, but could represent the charge associated with any number of charged particles and $V_{e'}$ is the electrostatic potential energy at the initial electron position before it was removed. The induced current is then:

$$i_A = \frac{dQ_A}{dt} = -e\frac{dV_e}{dt} = -e\left[\frac{\partial V_{e'}}{\partial x}\frac{dx}{dt}\right] \tag{2.31}$$

where, x is the direction of motion. The weighting field is plotted as a function of location in Fig 2.10. Simplifying this equation 2.31 to the form most commonly used in radiation detection [Rad88] gives:

$$i(t) = -q_m . E_w(x,t)v(x,t) \tag{2.32}$$

where q_m is an arbitrary charge, E_w is the weighting field and v is the charge group velocity, assumed to be constant. Therefore, it is crucial that the detector is operated at saturation

potential. Ramo's theorem provides a convenient way of simulating the currents induced on the electrodes of a radiation detector by the movement of charge carriers. Two charges are shown in transit in Fig. 2.10 along paths 1 and 2. The current induced on the electrode at unit potential is shown for both paths. Charge is collected along path 1 and therefore the current pulse has a net area. However, the signal from path 2 is more complex with no charge collected; but the Coulomb force of the moving charge does indeed produce a current on the electrode. The influence of this effect is determined by the weighting field, and because the charge crosses over a weighting field vector 'maximum' no net current is seen in the signal. Henceforth, discrimination between induced signals that represent the collection of charge, and those that do not, shall be made using the terms real charge and transient induced charge respectively.

2.5.3 Preamplifiers

A preamplifier, by definition, precedes another amplifier to prepare the signal for further amplification. It represents the interface between the crystal and the signal processing electronics. The interaction of a gamma ray liberates only a few thousand electron-hole pairs resulting in signals of small amplitude. These signals cannot be easily passed through relatively long cables without significant degradation. Therefore the preamplifier is necessary to transport the signal along cables to the data acquisition system. Charge-sensitive preamplifiers are commonly used with photodiodes in which the charge carried by the incoming pulse is integrated by a capacitor and then discharged through a resistive feedback network. The primary amplification stage is based on the use of a Field Effect Transistor (FET) which is coupled between the input stage of the preamplifier and the crystal. A simplified circuit diagram of a preamplifier is shown in Fig. 2.11; the FET is not shown. If the preamplifier has a large bandwidth, the product of amplification is a charge pulse with a fast leading edge that depends on the collection time of the charges in the detector, and a slow exponential decay characterised by a time constant, $\tau = R_f C_f$ where R_f is the feedback resistor and C_f is the feedback resistor. The fast leading edge is important because it preserves timing information from electron-hole transport.

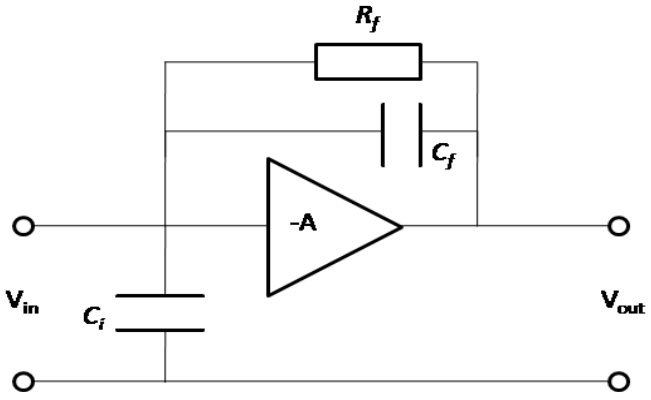

Figure 2.11: Schematic of charge sensitive preamplifier. C_i is the capacitance across the detector, C_f is the feedback capacitor and R_f is the feedback resistance. The FET is not shown.

Two noise factors contribute to degrade the performance of the preamplifier. Firstly, random fluctuations in the Gate-Source current of the FET add *shot noise* to the signal and secondly, *Johnson noise* is added from thermal noise in the FET. *Cross-talk* can also be a consideration with preamplifiers on segmented detectors, signals from different contacts couple and net charge is shared between neighbouring contacts. Short cables and electronic shielding is used to minimise cross-talk.

2.5.4 System Noise

Any unwanted fluctuations in the signal response are usually classified as noise for many applications. However, for radiation detection one has to be careful using this definition as random fluctuations in the number of charge carriers created is a significant effect. Therefore, noise is divided between intrinsic signal noise and superimposed electronic noise. Electronic noise is most significant at the beginning of the signal train because it can translate into an unusable signals during analysis, and can be treated as an equivalent noise charge (ENC)[Pie92]. A significant fraction of this thesis is dedicated to dealing with electronic noise superimposed on signals. The signal-to-noise ratio (SNR) can be used to quantify a signals' total noise, defined as the ratio of a signal power to the noise power corrupting the signal. Because the frequency distribution of the noise is broad it can be considered as white noise and will thus have a flat power spectrum. Therefore, a power spectrum can also be used to quantify the noise in a signal [Gro05]. Unwanted high

frequencies from SmartPET signals are removed with 40MHz low pass Nyquist filters. These form part of the analogue to digital converter circuitry in the data acquisition cards.

2.5.5 Energy Resolution

Energy resolution is conventionally defined as the FWHM of a spectral photopeak assuming a Gaussian distribution and no background contribution. A typical germanium detector has a FWHM of ~2keV at 1.33MeV. The intrinsic energy resolution, ΔE_i, of a germanium detector is determined by the contribution of three factors [Kno00].

$$(\Delta E_i)^2 = (\Delta E_D)^2 + (\Delta E_X)^2 + (\Delta E_E)^2 \tag{2.33}$$

where ΔE_D is the inherent statistical fluctuation of the number of charge carriers created, given by $(\Delta E_D)^2 = (2.35)^2 F \epsilon_{pair} E_\gamma$, where F is the Fano factor, ϵ_{pair} is the ionisation energy and E_γ is the photon energy. ΔE_X arises from incomplete charge collection due to recombination, or trapping in severely damaged detectors. ΔE_E is the contribution from electronic noise introduced by electronic components. The total energy resolution, ΔE_γ, of a detection system is obtained by adding the intrinsic energy resolution in quadrature to the contribution of Doppler broadening, ΔE_{Dop} (Equ. 6.3).

$$\Delta E_\gamma = \sqrt{(\Delta E_i)^2 + \left(\Delta E_{Dop}\right)^2} \tag{2.34}$$

2.5.6 Efficiency

Efficiency is a measure of the fraction of photons that are counted against the possible number of photons that could have been counted. It is measured using four primary methods:

Absolute efficiency: Defined as the ratio of detected photons against the total number emitted by the source. It is therefore influenced by geometrical considerations, with low absolute efficiencies for distant sources and is given by:

$$\epsilon_{abs} = \frac{number\ of\ detected\ photons}{number\ of\ emitted\ photons} \tag{2.35}$$

Relative efficiency: Defined as the efficiency of a germanium detector relative to a NaI(Tl) crystal measuring 76mm in diameter and 76mm in length. The source is located 25cm from the detector, and the efficiency is usually measured using a 1.33MeV photopeak.

Intrinsic efficiency: Accounts for the stopping power of the detection medium and is given by:

$$\epsilon_{int} = \frac{number\ of\ detected\ photons}{number\ of\ photons\ incident\ on\ detector} \tag{2.36}$$

Photopeak efficiency: When considering counting efficiency, the nature of the interaction also has to be taken into account. The photopeak efficiency accounts only for those events in which the gamma ray deposits the full energy in the detector; it is given by:

$$\epsilon_{ph} = (PT) \times \epsilon_{abs} \tag{2.37}$$

where PT is the peak-to-background ratio. A standard measurement of the peak-to-background is obtained from the sum of the ^{60}Co net peak areas divided by the total number of counts in the spectrum for energies ranging from 100keV to 1350keV. This is of importance when Compton scattering is a consideration. Low photopeak efficiency is ideally required for a Compton camera scattering detector, and high photopeak efficiency is ideally required for the absorbing detector.

2.6 Gamma-Ray Tracking

The escape of Compton scattered photons from detector systems was a major limitation in early nuclear structure studies, resulting in only partial energy deposition. Consequently, energy spectra displayed many features which degraded ones ability to examine the discrete energies emitted from transitions between energy levels in the nucleus under investigation. The problem is so severe because Compton scattering has such a high cross section at the energies of interest in most nuclear spectroscopy experiments. Several developments have been made to limit the degradation caused. Compton-suppressed

detectors [Nol85] provided a substantial improvement in the peak-to-total ratio. The principle is to house a germanium detector inside a dense scintillation shield and measure coincidence events with a timing circuit. All coincidence events between the germanium and scintillator are vetoed. Typical peak-to-total ratios for a suppressed spectrometer are ~60% compared with ~20% for an unsuppressed detector [Nol85]. By replacing the suppression shields with a cluster of germanium detectors it is possible to accurately measure both coincident energies. If both energies are from the same event they can be summed to give the total event energy. This mode of operation is known as add-back and is clearly beneficial to system efficiency. However, a naive application of add-back permits the summation of two random coincident events.

The concept of gamma-ray tracking provides a possible solution to false add-back by using knowledge of an events' kinematics. Theoretically, if the kinematics match that of a Compton scatter then the event is valid, otherwise the event is vetoed. This is in principle a tracking of an events' interactions throughout the detector array, from the first scatter through to photoelectric absorption. Although appearing to be simple, in reference to the Compton scattering formula (Equ. 2.7), it can be seen that the incident energy is assumed to be the total energy of the original emission. Additionally, if there are only two interactions then two possible directions for the incident gamma ray can be obtained. The sequence of interactions may not even be unique for a known target location due to finite spatial and energy resolution [Lee03], and a figure of merit is needed to determine the actual sequence of the event. The uncertainties in directionality can be addressed to some extent with the Klein-Nishina distribution (section 2.1.2). Gamma-ray tracking has been shown to work in principle [Baz00].

Spatial resolution is a primary factor which also influences successful experimental gamma-ray tracking in a Compton camera. Newer detector fabrication technologies are used to increase raw granularity by electrically segmenting the electrodes. This is only a partial solution because practical limitations on the number of read-out channels prevent mega-pixel arrays. An increase in raw spatial resolution is possible with an intelligent use of the digital pulse shape, which provides extra attributes related to the interaction location.

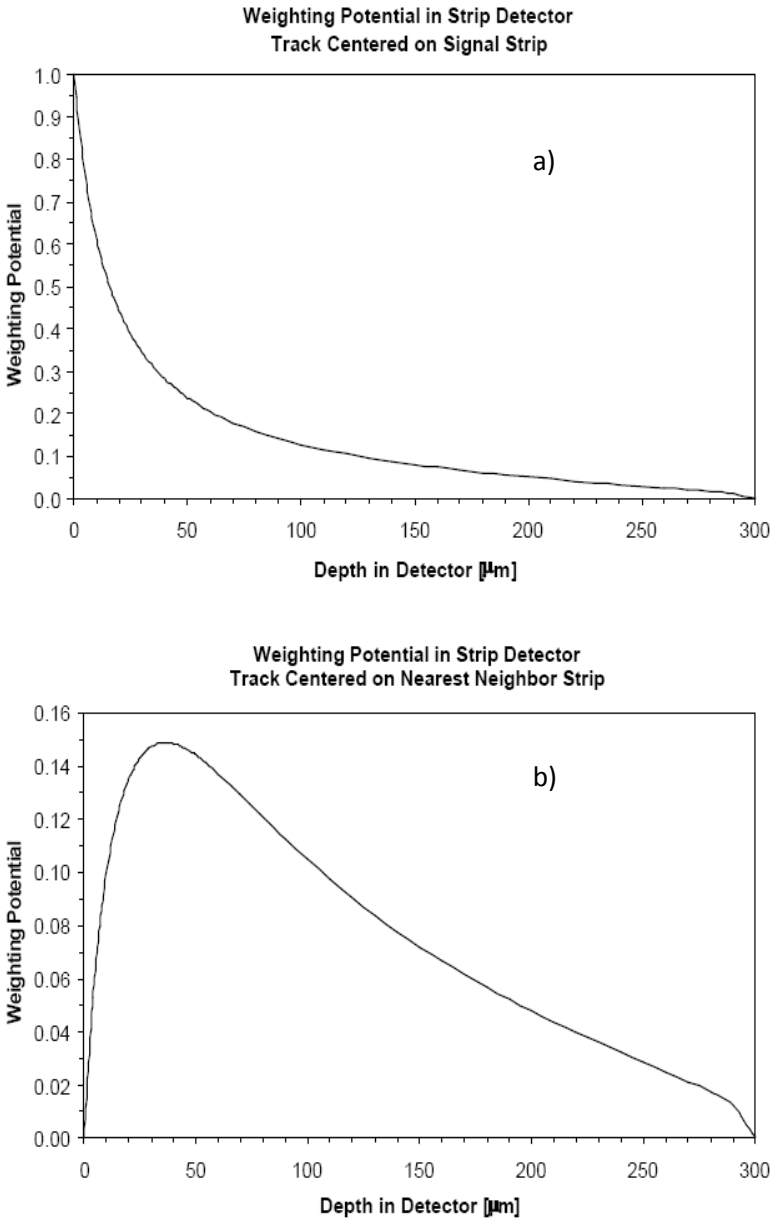

Figure 2.12: Comparative weighting potentials for a single path along through the centre of a strip. The collecting electrode couples to the charge through the field shown in image (a). The coupling of the next nearest neighbouring electrode (spectator electrode) is shown in image (b). [Spi01]

2.7 Pulse Shape Analysis

Pulse shape analysis (PSA) increases spatial resolution beyond that provided by the raw detector granularity and it is a technique which is essential for the success of gamma-ray tracking and perhaps segmented Compton cameras. PSA is a somewhat expansive term and a restriction shall be applied in this thesis in which it specifically refers to the method of analysing signals from photodiodes in the context of an associated weighting field. Other

PSA techniques have been established in radiation detection, such as PSA for drift chambers [Sch86] and pulse shape discrimination PSD [Asp07] for fast neutron detection, but neither of these methods exploits the weighting field concept for increased spatial resolution and thus PSA for gamma-ray tracking is a distinct technique. A position resolution of 1-2mm is thought to be sufficient for gamma-ray tracking [Mih00]. Whilst no such estimate will be made for a Compton camera, it is sufficient to assume that, based on Compton kinematics, it is critical to achieve the best possible spatial resolution. Simulations have been performed, and are presented in appendix A, that attempt to quantify image quality as a function of spatial resolution.

PSA requires segmented electrodes coupled to fast analogue to digital converters (FADC). The signals can then be processed offline or with onboard field programmable gate arrays (FPGA). Returning to the concept of the weighting field allows an appreciation of the concepts of PSA. Segmented electrodes allow non-collecting electrodes to observe the motion of charge carriers in the detection material via a coupling effect of the observing electrode and charge through the weighting field. The weighting field is only valid in a multi-electrode device and is shown for two electrodes of such a device in Fig. 2.10. Charge carriers are formed upon interaction and immediately drift towards their collecting electrodes. Real charge is collected on the collecting electrode whilst induced transient charges are seen on spectator electrodes. The weighting field coupling is shown for the collecting strip and observing strip in Fig. 2.12. A key point that has significance in radiation detection is that all induced signals occur simultaneously. A beneficial use of this information is to sum all of the signals to quantify the time of interaction.

2.7.1 Basic Pulse Shapes

In theory the weighting field plays an important role in relating signal shapes to interaction locations. More practical work is described in subsequent chapters but it is worth building a model of signal shape in this concluding section for later reference. Defining a point in three dimensions requires three basis vectors or axes in Cartesian space. The first axis is through depth, and coordinates along this axis can be specified by the real charge depth between the electrodes. The second and third axes are orthogonal and parallel to the electrodes'

planes. These axes specify the lateral locations of interaction. Thus the interaction can be located with varying accuracy based on coordinates on these axes.

Conceptualising the depth dependence of real charges is straight forward. If the detector is operating under saturation potential then the real charge corresponds to electrons and holes separating at saturation velocity. Under constant velocity, the growth of charge on the collecting electrode must simply be a function of drift time which is constant for a given interaction depth. Therefore, the real charge must have a characteristic *rise time* parameter. For interactions occurring in the central depth, the drift distances are equal for both charge carriers and one could naively expect this location to result in the fastest signal *rise times*. However, the charge carriers have different mobility and therefore the *rise time* distributions are not symmetrical about the central depth.

Lateral information can be gained from analysis of electrodes adjacent to the collecting electrode. These shall be referred to as spectator electrodes. The transient induced charges that appear on these strips actually fully describe the interaction location but are difficult to analyse due to noise. Therefore, all PSA work in this thesis and beyond takes the approach of combining real and transient induced charge signal information. The weighting field potential coupling for spectator electrodes is shown in Fig 2.12b. Charge carriers respond to the coupling immediately upon liberation. Transient induced charge coupling can take three distinct polarities [Tur06]:

- The charge cloud is created in a field of decreasing potential. The small induced transient signal is then found to be positive.
- The charge cloud is created in a maximum field of near zero differential potential. The small induced transient signal is then found to be bi-polar. This region is relatively small and it is shown that polarity transitions occur rapidly.
- The charge cloud is created in a field of increasing potential. The small induced transient is then found to be negative.

Observations support this simplified picture of the weighting field. Induced transient charges are therefore highly sensitive to interaction location. However, the presence of noise makes relative comparisons of the spectator electrode responses necessary. Because weighting potential also varies as a function of lateral interaction location and not only of

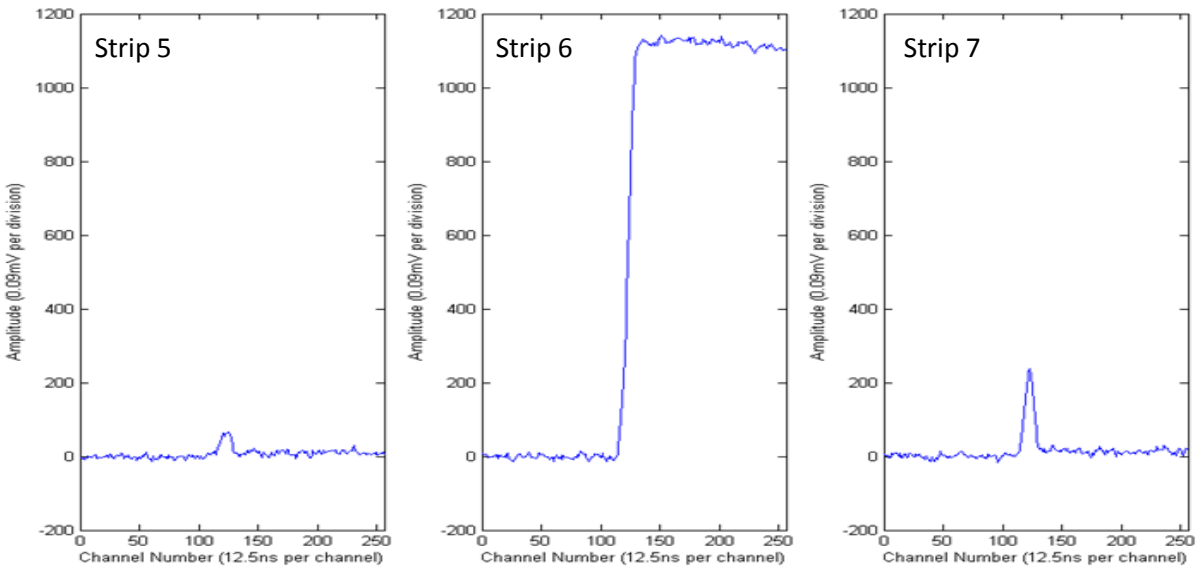

Figure 2.13: Examples of the response of SmartPET 1 to a 662keV interaction. The real charge was observed on the sixth strip and transient induced charges can be seen on strips 5 and 7. Given the relative magnitudes of the transient induced charges it is assumed that the interaction was probably located nearer to strip 7.

depth, see Fig 2.10, a parameter can be used to specify the relative interaction location between two nearest neighbour spectator electrodes. The induced transient charge *asymmetry parameter* is defined as [Mih04]:

$$R = \frac{A_{s+1}(t50) - A_{s-1}(t50)}{A_{s+1}(t50) + A_{s-1}(t50)} \tag{2.38}$$

where $A(t50)$ is the signal value recorded on the spectator electrodes $s+1$ or $s-1$, when the signal on the collecting electrode exceeds a 50% threshold of its amplitude. *Rise time* and *asymmetry parameter* methods for determining interaction location are collectively considered as pulse shape analysis. Signals shall be analysed according to pre-defined parameters discussed during the application of PSA. Sub millimetre resolution has been reported [Mil05] with average data. A very similar experiment to the one reported in [Mil05] is performed in this thesis but no comparison will be drawn against this method. A best test of spatial resolution is in the analysis of the resulting images.

An example of the characteristic response of the detector to a 662keV 'single' interaction at an unknown location within the detector volume is shown in Fig. 2.13. Only the collecting electrode strip and neighbouring spectator electrode strips are shown. It is difficult to gauge the depth of interaction, but the interaction can be assumed to be closer to the left spectator electrode strip given the relative magnitudes of the transient induced charges.

Chapter 3

SmartPET Coincidence Measurements

Initial detector performances and a number of coincidence scans are described in this chapter. The purpose of a coincidence scan is to provide a measure of the characteristic detector response to single site interactions at various locations from within the active volume. Single site interactions are those in which the full energy of a photon is deposited at a single site through photoelectric absorption, or a single Compton interaction in which the scattered photon escapes the system. Therefore, a direct relationship between interaction location and interaction response is constructed. Whilst previous characterisations have been performed [Tur06], the conditions under which they were performed makes them susceptible to Compton scattering. This scan should vigorously reject multiple scattering and allow a robust analysis of single site interactions. Indeed, the collection of detector responses at single sites permits the development of a partial basis data set which has a variety of applications, including pattern recognition for improved spatial resolution and Compton signal reconstruction for digital Compton suppression testing.

3.1 SmartPET

The principal aim of SmartPET is to exploit the technological advances made in radiation detection for the purposes of small animal imaging. Innovative fabrication techniques in the

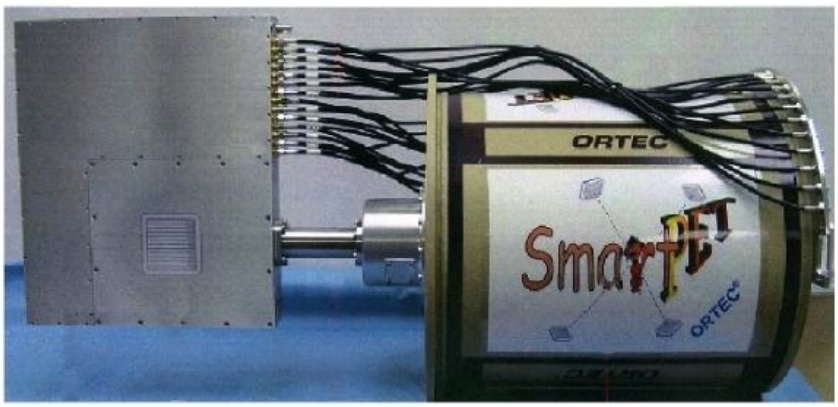

Figure 3.1: Photograph of SP1. The crystal is housed behind the small window in the cryostat which is marked with the electrode segmentation. The preamplifiers are read out from the black cables. The copper cold finger runs through the tube from the crystal to the dewar.

early nineties allowed the segmentation of large electrode surfaces. Furthermore, a multi-electrode device permits the analysis of signals that have been generated by means of the weighting field concept. The feasibility of gamma-ray tracking relies on these electrically autonomous contacts to improve spatial resolution. PSA, and ultimately gamma-ray tracking could be invoked to reconstruct images of distributed radioisotope sources in a fashion which will be unique in nuclear medicine. The anticipated gain in spatial resolution will be complemented by an energy resolution that is already far superior to that of current scintillators. This endeavour necessarily requires segmented germanium detectors and orthogonal segmentation on a planar geometry has been selected.

3.1.1 SmartPET Detectors

Both SmartPET detectors were manufactured by Ortec. The first detector was delivered in February 2005. The monikers SP1 and SP2 are used to differentiate between both detectors in chronological order. SP2 was delivered in June 2005. Both detectors were made to the same specifications but have slight variations in their operational characteristics. A brief description of these variations and the implications for imaging is given in chapter 6.

SP1 and SP2 are high-purity planar germanium double-sided strip detectors (DSGSD). The raw crystal dimensions are $74 \times 74 \times 20$mm, but the actual active regions are $60 \times 60 \times 20$mm. This allows the active region to be flanked by a 7mm-wide guard ring. Electric fields

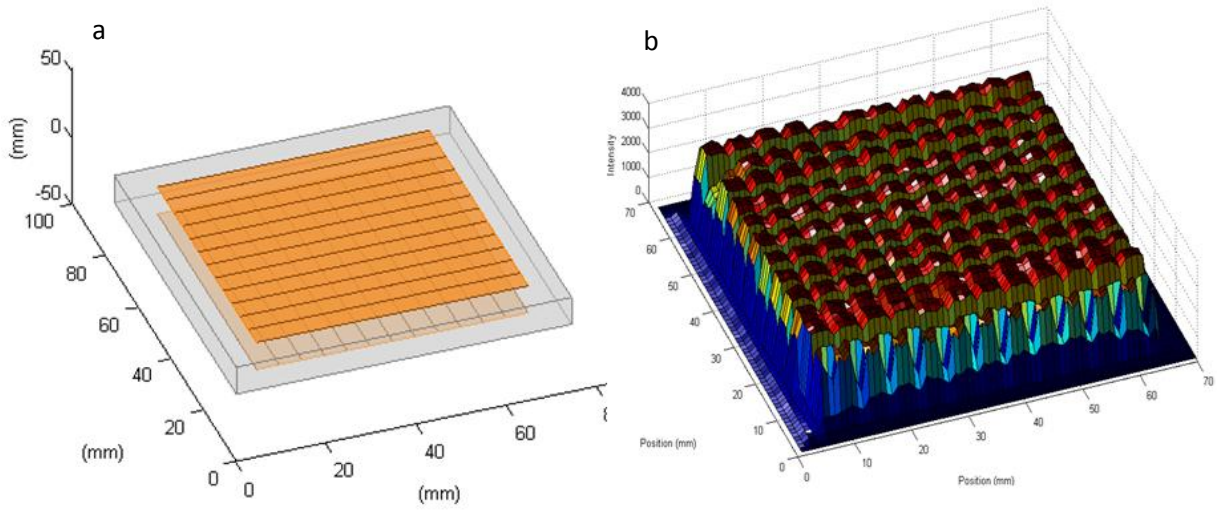

Figure 3.2: Image (a) shows a geometrical representation of a SmartPET detector. Each active electrode face is surrounded by a 7mm wide guard ring. 12 electrically separate strips are etched on each face and each strip is 5mm wide. Strips on opposing faces are orthonormal to create 144 closed-face-pixels. Image (b) shows the effect of the orthonormal arrangement on effective pixilation. A source was scanned across the face of SP1 in 1mm steps with the number of fold 1 events being recorded at each position. Compton scattering at strip boundaries reduces the intensity of fold 1 events. Therefore, a 2D histogram of fold 1 events shows the effective pixilation of the detector.

warp at the edges of a capacitor of finite length, and the guard ring is a necessary dead region which ensures the electric field within the active region can be considered relatively uniform. The crystals are housed in a cryostat with a 1mm-thick aluminium entrance window. Cryogenic temperatures are maintained by a copper cold finger that is in thermal contact with the crystal, and is also in thermal contact with a 12 litre liquid nitrogen dewar that can sustain cryogenic temperatures for 72 hours. Fig 3.1 shows a photograph of the cryostat and dewar of SP1, the cold finger runs through the connecting cylinder.

Ortec will not disclose the details of electrode fabrication (thought to include amorphous germanium on one contact). However, electrodes are usually created through boron ion implantation for the p-type contact and lithium diffusion for the n-type. Consequently, p-type contacts have a shallow thickness typically less than $0.5\mu m$ and n-type contacts are usually two orders of magnitude thicker. Segmentation can be achieved with photolithographic techniques. The actual segmentation dimensions for SP1 and SP2 are quoted as $\sim 0.3\mu m$ thick with a $180\mu m$ separation for the p-type contact, whilst the n-type contact is $50\mu m$ thick with a $300\mu m$ separation. The segmentation is such that 12 parallel strips are created on each face. The strips are orthonormal and 144 closed-faced-pixels are formed. Fig 3.2 (a) shows a schematic of the segmentation of a SmartPET detector crystal, whilst Fig 3.2 (b) shows the results of a front-face singles scan of SP1; *front-face* refers to the

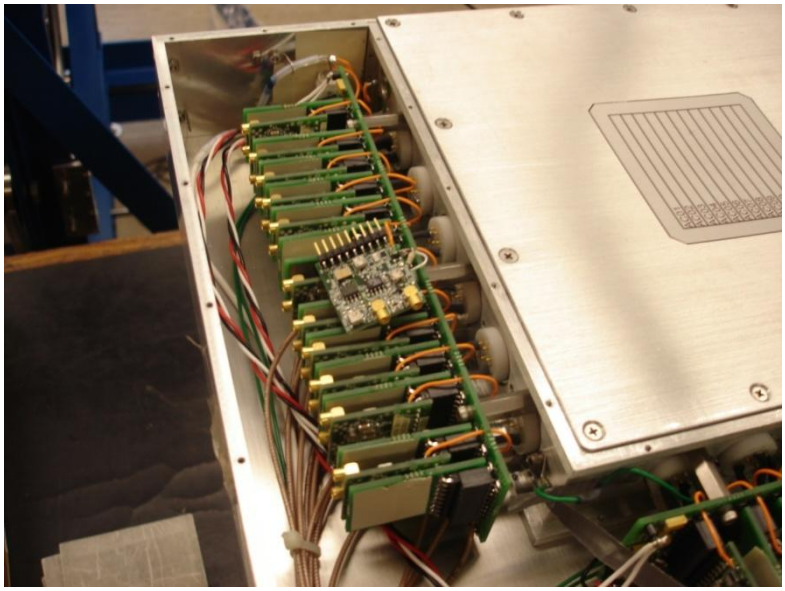

Figure 3.3: Cryostat casing removed to expose the DC preamplifiers of SP2.

act of shining a source over the face of the crystal. *Singles* implies that only 'single' interactions were of interest and no other detectors were involved in the scan.

The impurity concentration is quoted as $\sim 6 \times 10^{9} \mathrm{cm}^{-3}$ with a maximum variation of 5% through the depth of the crystal along the <100> crystallographic direction. The operating voltage of the crystal is -1800V, the field lines of which follow the <100> crystallographic direction as this is the fastest charge carrier axis at saturation velocity (section 2.4.2). Potential is applied through the preamplifier (next sub section) to the p-type contacts whilst the n-type contact is earthed. Contact identification is performed on the basis that the p-type contact is coupled indirectly to the high voltage, provided by an Ortec 660 bias supply NIM unit which is in turn coupled to the mains supply. The p-type contact is therefore known as the AC face and all strips on this face are then AC01, AC02, …, AC12. Likewise, the n-type is technically coupled to earth through a network of electrical components and is therefore referred to as the DC face. All strips on this face are then DC01, DC02, …, DC12.

3.1.2 Preamplifiers

Each electrode is fitted with a charge sensitive preamplifier, thought to be based on a design by the University of Cologne [Ebe01]. The preamplifiers use warm FETs at the input stage and are located in the cryostat near to the crystal. The FETs are the first active component

that the crystal signals are processed by, requiring the FETs to be extremely close to the crystal. The preamplifiers are low noise, high bandwidth, and the gain is specified as 300mV/MeV. Rise times for a 5ns, 100mV step function are reported as 69.2ns for the DC side and 67.2ns for the AC side [Tur06]. The decay constant is reported as 43μs for both sides of the detector [Tur06]. Measured rise times and the decay constant can be used to simulate the response of the preamplifier, this is important for any electric field calculations. Fig 3.3 shows the preamplifiers exposed in the cryostat.

3.1.3 Reported Performance

Basic SP1 detector performance is reported in earlier work [Tur06]. It was found that the energy resolution was slightly worse near active region edges, probably due to a weaker electric field. It was also discovered that DC11 had a poor energy resolution of 4.1keV at 122keV. Excluding DC11, mean energy resolution is 1.4keV for the AC side and 1.3keV for the DC side at 122keV. Efficiency as a function of energy is also reported for each face. It is found that DC efficiency drops considerably at low energy, whilst AC efficiency remains stable, the explanation for this is given as the different thicknesses of the contacts.

3.2 Data Acquisition

The analysis of signals for time, energy and spatial information in this work required the use of fast digital data acquisition and associated controlling software. The hardware is designed by Daresbury Laboratory, and the software is an in-house solution which collects data from the hardware and saves it to disk file for later access. Every recorded event can be accessed with a bespoke C code, written to perform any analysis the user wishes to perform. The work in this thesis represents ~5000 lines of C code.

All triggered signals are digitised with Gamma-Ray Tracking 4-channel cards (GRT4) [Laz04]. Each card has four parallel analogue-to-digital converter (ADC) input channels and 8 field programmable gate arrays (FPGA), which are programmed with algorithms to time stamp signals, and calculate interaction energies using a moving window de-convolution (MWD)

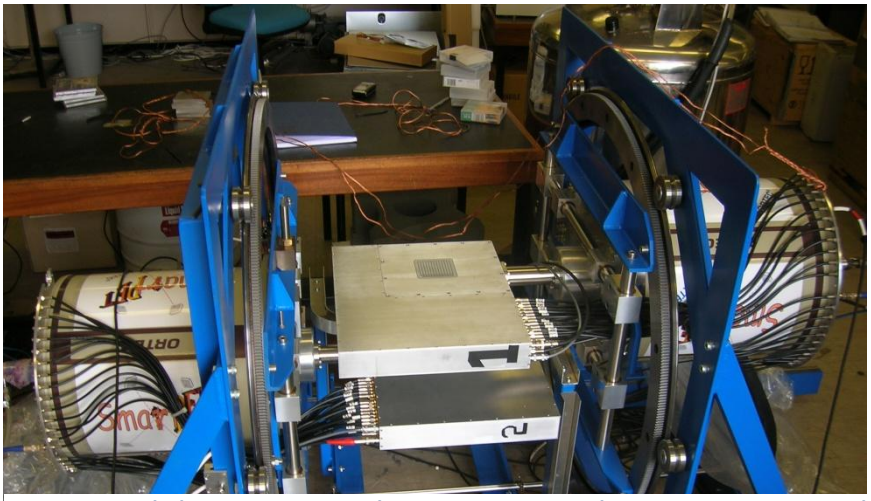

Figure 3.4: Both detectors sitting in their rotating gantry. The gantry permits PET and Compton camera studies and is controlled via 'in-house' MIDAS software. The gantry uses a holding torque to hold the detectors horizontal.

method [Geo93]. The ADCs are 14bit, 80MHz, sampling the signal every 12.5ns over 256 samples. GRT4 cards use VME architecture and as such are limited to a data rate which translates to 220 events per second. The signals are buffered, by means of a first-in first-out buffer (FIFO), and can be extracted when a trigger signal is received. Newer data acquisition cards based on a Lyrtech design are currently being commissioned but were not used in this work. This new system is based on PCI architecture and combines several levels of FPGAs and digital signal processors (DSP) allowing higher count rates and more advanced online analysis. This new system also includes Total Data Readout (TDR), and can be used with a digital trigger. Perhaps more importantly, these cards provide a synchronous clock to all parallel channels, removing a large obstacle in the pre-analysis chain. The GRT4 cards do not have a synchronous clock and therefore every channel in a single event is extracted from the FIFO at almost arbitrary times. This implies that average signals cannot be aligned around a common time because there was no common time to begin with. The consequence of this will become apparent in subsequent chapters.

3.3 Previous Characterisation

Previous work [Tur06] characterised the response of detector SP1 with collimated sources, providing the investigator with a well defined beam of photons. The collimator had two degrees of freedom in an x-y plane. Therefore, the beam was shone into the detector either

directly onto the front face through the aluminium window, or through the cryostat and into the detector's short axis. SP1 response through depth or across the detector face was then measured as a function of x and y coordinates. The penetration depth of photons within the active volume was not measured and only defined by the attenuation of gamma rays in germanium. However, a third plane is required to properly define detector response as a function of interaction location.

Another problem with such a scan results from the selection criteria of analysed events; if only two opposing electrodes trigger, the event is determined to be the resultant of a single-site interaction. However, Compton scattering is the most probable interaction for ^{137}Cs gamma rays. If a scatter is contained within a closed-face-pixel it is falsely accepted as a single-site interaction when in reality the event is a scatter. Therefore, discrimination of scattering within individual closed-face-pixels cannot be used to reject events. Scattering information is simply lost in electrode response. Chapter 5 details a technique to identify these events but requires validation first. This issue becomes a major concern near strip boundaries, where the scattering contained by the detector will not be symmetrical and detector response is favourable for scattering towards the detector centre. This scenario must to some degree skew observed average detector response towards the centre of a closed face pixel. The coincidence scan is biased towards detecting well defined scattered events which are most probably single-site interactions. Only SP1 was scanned using coincident measurements.

3.4 Coincidence Scan

The coincidence scan records only those events which are effectively detected simultaneously in two independent detectors. Event types are now restricted to random coincidences from background, direct coincidences from the collimated source and true scatter coincidences. The geometrical arrangement of the detectors provides an exclusive measurement of scattering angle and hence the Compton kinematics are well defined. A narrow time-to-amplitude (TAC) coincidence window can be used to reduce the influence of random coincidences [Pet93]. Alternatively, off-line analysis of energy deposition and prior knowledge of possible scattering angles can be utilised to increase sensitivity to true

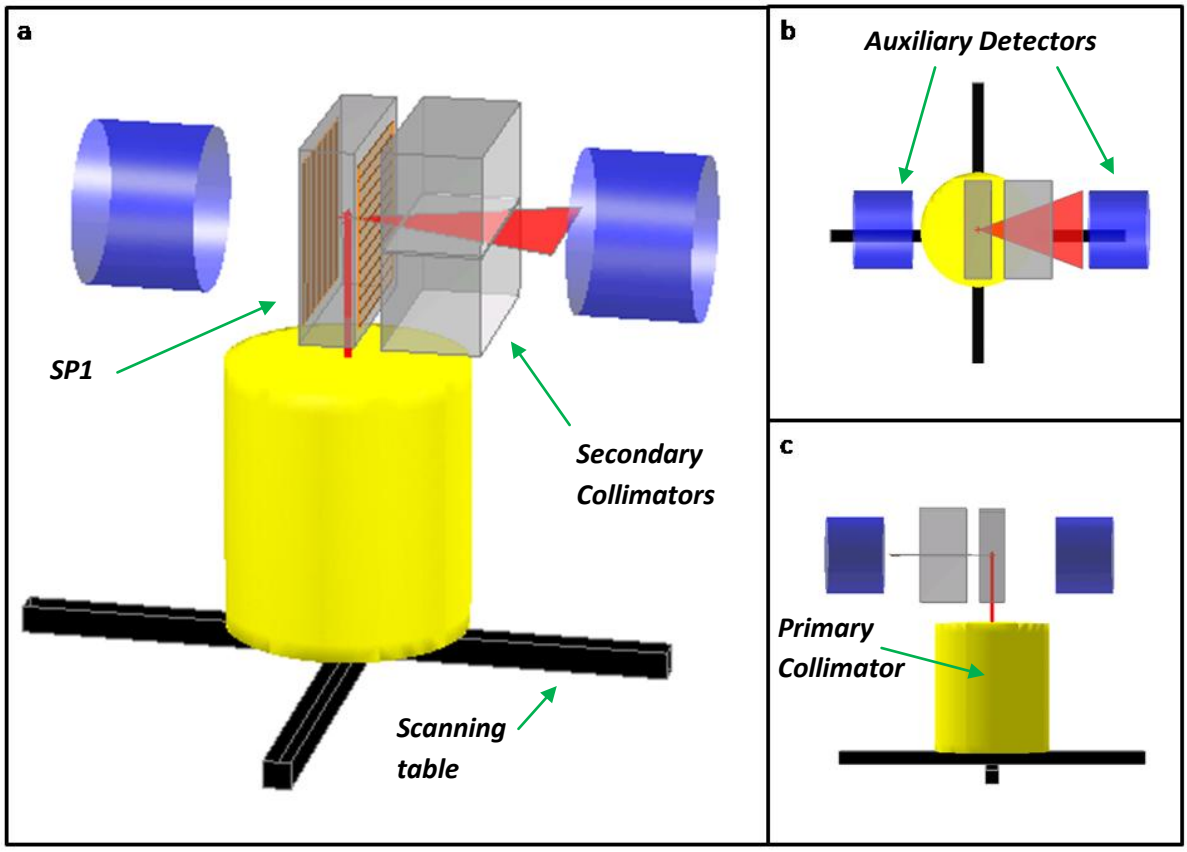

Figure 3.5: Schematic of coincidence experiment. The primary collimator is housed in a large lead cylinder shown in yellow. The beam is shone into SP1 and is controlled in the x-y plane by two stepper motors (black slides). Coincidence is performed with two auxiliary detectors angled at 90^0 to the primary detector (represented as blue volumes). Secondary collimation can be performed to define the interaction in three dimensions, or the secondary collimators can be removed and the interaction is defined in two dimensions. See Fig. 3.6 for a photograph of the experiment.

scattering coincidence [Mil05]. Geant3 simulations have been reported [Vet00] showing that energy gates are highly effective in restricting data analysis to only single site interactions; only 55% of scatter coincidences interact at single sites in each detector compared with over 85% with energy gates.

Secondary collimation[1] is used in all three reported coincidence experiments [Pet03][Mil05][Vet03]. However, these experiments all suffered from low statistics. Therefore, based on a high probability of single-site interactions with the utilisation of energy gates, a judicious removal of secondary collimation has been made for a number of experiments in this thesis. This also provides a fair comparison with previous work [Tur06]. Fig. 3.5 shows the geometrical arrangement of the coincidence experiments performed, in which an axis connecting the two auxiliary detectors sits perpendicular to the collimated

[1] Secondary collimators are defined as the collimators which restrict the scattering angle to ninety degrees.

beam axis, and an SP1 long axis is parallel to the beam. The beam was shone along AC strips and across DC strips so that the scattered beam in Fig 3.5 is shown escaping the DC face.

This coincidence experiment required auxiliary detectors with excellent energy resolution, and as such coaxial germanium detectors were used, permitting energy gates to be applied. Interaction locations are uniquely defined by x, y and z coordinates when secondary collimators are used. However, the auxiliary detectors then measure photons which have only been scattered through ninety degrees to the primary beam and although the energy of scattered photons is well defined by the Compton scattering formula (section 2.1.2), the probability of this particular ninety degree scatter is particularly low as defined by the Klein-Nishina formula (section 2.1.2). A 1GBq collimated ^{137}Cs source was used and predicted to give a maximum count rate of ~200 per hour with secondary collimators, with energy depositions of 374keV in SP1 and 288keV in the auxiliary detector.

3.4.1 Auxiliary Detectors

Two high-purity germanium detectors were used as the auxiliary detectors. One was manufactured by Canberra and the other was manufactured by Ortec. The Canberra detector has a segmented outer contact and is referred to as the M6X6 in all subsequent work. The other auxiliary detector is known as the PT6X2 (Ortec) [San03], which was a revolutionary n-type coaxial detector combining external monolithic segmentation with internal monolithic segmentation. It is the world's first 12-segment coaxial detector requiring only eight preamplifiers. The average performance of the central core on finalisation of production at ORTEC was 0.9keV FWHM @ 122keV in the front and 2.4keV FWHM @ 1.33MeV in the back. A recent use for the PT6X2 was a radiation hardness test at Cologne in which it was exposed to a large neutron flux. However, the performance was measured before experimental execution and was found to be suitable for coincidence measurements. Both PT6X2 inner contacts have been used in the coincidence experiment, whilst no outer contacts were used. Likewise, only the central core of the M6X6 has been used. The average energy resolution stated upon performance measurements taken at the time of delivery are 3.6keV FWHM @ 122keV and 4.10keV FWHM @ 1.33MeV.

3.4.2 Collimated Source

A 994MBq ^{137}Cs radioisotope source was collimated with a hevimet alloy channel of 1mm diameter. This alloy is composed of tungsten (Z = 74), nickel (Z = 28), copper (Z = 29) and iron (Z = 26) with a 95% concentration of tungsten and undisclosed concentrations for the remaining elements [TUNG]. Hevimet is a common shielding and collimator material that is used extensively in nuclear physics experiments. Given hevimet's high atomic number, the photoelectric cross section for 662keV photons will be significant (section 2.1.1), although smaller than that of lead. However, the stopping power of hevimet is greater than that of lead due to a greater density, $18\mathrm{g/cm^3}$ versus $11.34\,\mathrm{g/cm^3}$. It is also easier to manufacture a 1mm diameter channel in hevimet. Additionally, because it is a hard material, a reliable linear channel is provided throughout the experimental duration.

The channel was machined directly in the front face centre of a hevimet cylinder of length 17cm and radius 5mm. With such thin walls it is necessary to house the primary hevimet collimator in a lead containment vessel, as shown in yellow in Fig 3.5. This lead cylinder consisted of lead bricks and a single large lead radial disk of 17cm in length and 36cm in diameter. The radial disk effectively sits between emitted photons and the auxiliary detectors, providing 24cm of shielding. The mean free path of 662keV gamma rays in lead is 24mm, therefore the source will be significantly attenuated. Hence, few direct coincidences from collimator penetration were expected. The lead bricks acted as a radiological shield beneath the source. In total, the collimator aperture was 26cm from the base plate of the scanning table. Monte Carlo N-Particle (MCNP) simulations of the collimator assembly have been performed. The total separation between SP1 and the collimator aperture was 83mm. Simulation predicts that the beam diameter in the centre of the crystal with this separation will be 1.3mm.

3.4.3 Interaction Localisation

The scanning table provides x-y position information by driving the collimator housing across the underneath of SP1. The multi-axis, high-load table is manufactured by Parker Hannifin instruments (model number 408012ST) and has a range of 300mm in either the x

or y direction with a precision of 100µm under a maximum load of 708kg. The table is user-controlled by MIDAS, an 'in-house' software solution which then records the scanning table position and includes this information in data acquisition for each subsequent run.

Simple lead blocks, machined to specification in Liverpool, were used as the secondary collimators to provide z position information. Two sizes of lead block were machined, a large block (73x150x74mm) and a smaller block (14x98x50mm). This was partly due to the need to scan several DC strips simultaneously due to the expected low statistics, which requires the shorter blocks, but also because the larger blocks can be used nearest to the primary collimator aperture where the scatter beam profile is more intense. Both block sizes had near perfect planes sheared onto their faces so they could sit together or be prised apart with shims to form a collimation slit. The shim materials used were brittle plastic (1.2mm thick), flexible plastic (0.2mm thick) and aluminium (1.4mm thick). Once the shim thickness was selected, the complete stack of secondary collimators was placed onto a thick aluminium plate. The plate was suspended below a purpose-built uni-strut structure and moved vertically along the z axis by a screw and thread at each corner. This offered the ability of levelling the plate to within a thousandth of a degree with an engineering level. Once level, the secondary collimator stack was simply scanned across the front face of the detector by placing shims under the entire secondary collimation stack. See Fig 3.6 for the actual experimental configuration.

3.5 Experimental Data Acquisition System

Data acquisition (DAQ) from all detectors was performed using the GRT4 cards of the SmartPET system (section 3.2). The signals from all detector channels were split in a patch panel. This action served two purposes; individual signals could be split for an external trigger system and a common earth could be established to reduce noise. The trigger system managed the data acquisition, triggering under predefined conditions and sending an acceptance signal to the GRT4 cards. When a trigger event occurred, a user-specified number of samples were extracted from the FIFO buffer as the pre-trigger information, after which new signal samples are retained until the FIFO fills. An inhibit signal is sent out from the GRT4 cards to a gate and delay generator whilst each event is recorded to ensure the

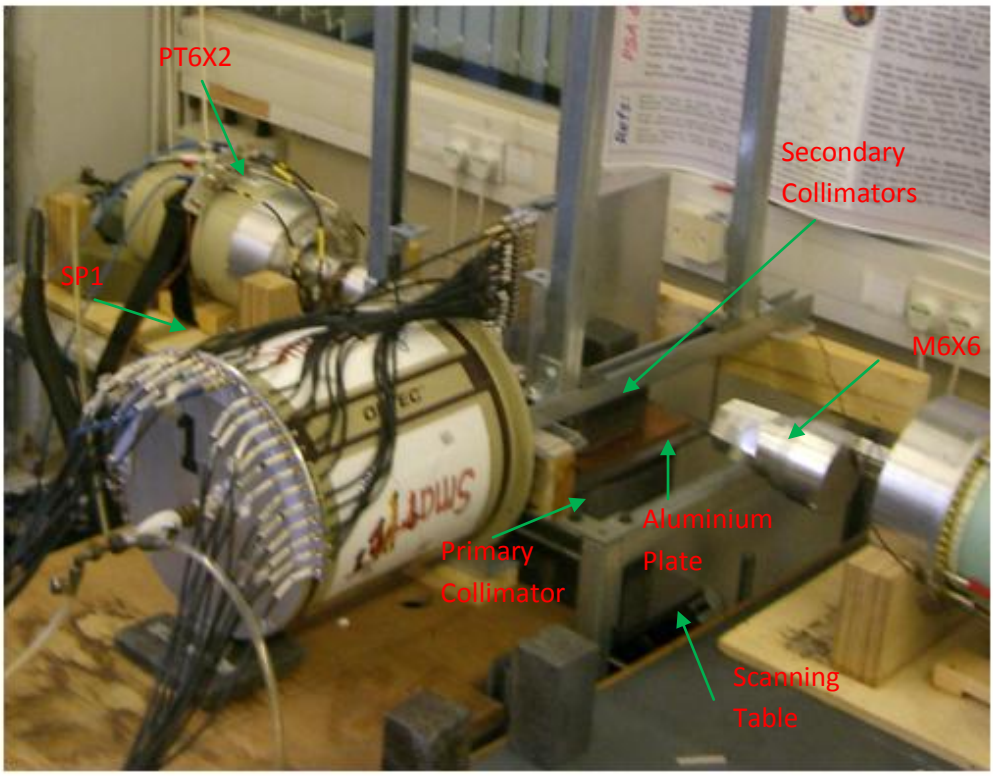

Figure 3.6: Photograph of actual experimental set-up including SP1 and the auxiliary detectors. From the bottom up, one can partially see the scanning table and its stepper motor housing. Next sits the primary lead collimator housing in which the tungsten collimator is embedded. Above the large lead cylinder rests the aluminium plate which is suspended from a uni-strut assembly. The aluminium plate is adjusted by four corner screw threads, one of which can clearly be seen. The secondary collimators sit between SP1 and the auxiliary detectors. This image can be compared with Fig 3.5 which is a schematic representation of this experiment.

FIFO buffer is not over written. One extra GRT4 card was required for the auxiliary detectors and all GRT4 cards read out their moving window deconvolution energies and digitised signals. These data were written to tape for offline analysis. Each recorded event consisted of 27 signals: 24 from SP1, 2 from the PT6X2 and 1 from the M6X6. Online analysis can be performed with MTsort [Sam00], another 'in-house' software solution.

3.5.1 Data Acquisition Triggering

The triggering system was set-up to record data from all detectors provided that SP1 and at least one auxiliary detector each sensed a single event in coincidence. Fig 3.7 shows a schematic block diagram of the triggering system and DAQ. The patch panel splits all SP1 AC contact signals, and all core signals from the auxiliary detectors. One of the resulting signal branches from this node is connected directly to a corresponding GRT4 channel, whilst one

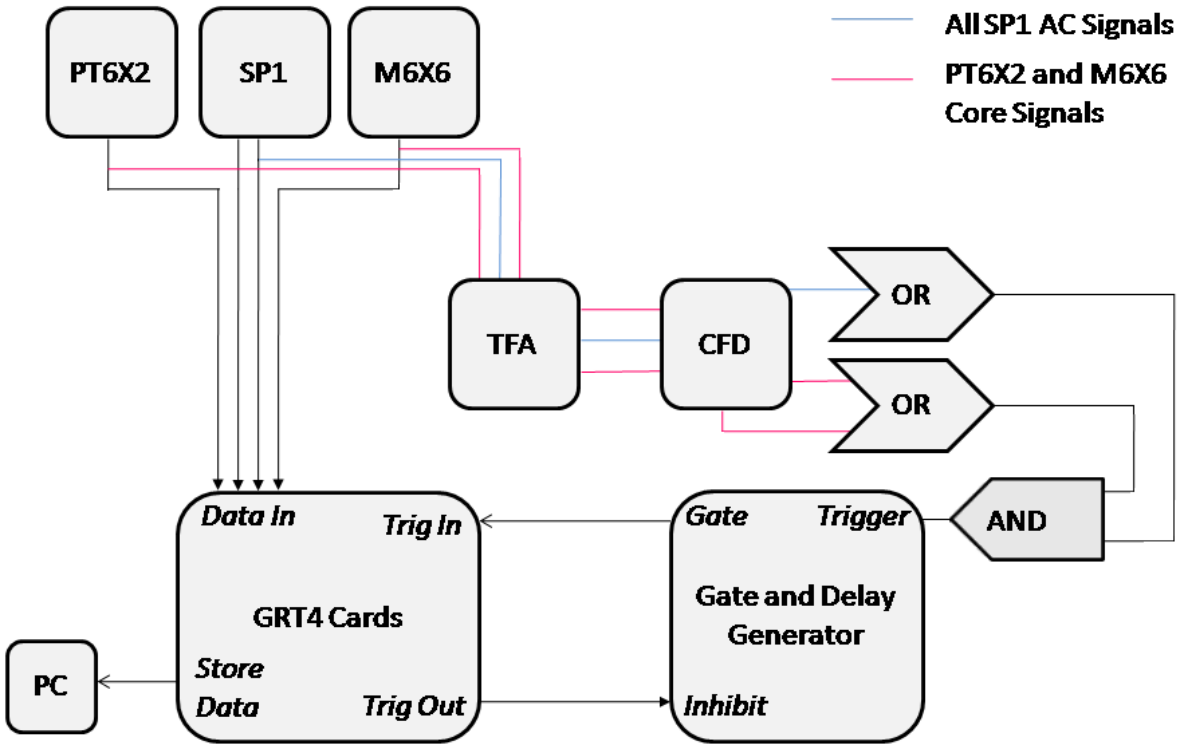

Figure 3.7: A schematic of data acquisition for the coincidence measurements. SP1 AC signals are split and go in the triggering system, whilst DC signals go straight to the GRT4 cards. All auxiliary detector core signals contribute to the trigger signal. If one or more SP1 AC electrodes fire in coincidence with one or more auxiliary cores the final trigger is true. If the system is free, all GRT4 channels are saved to a disk file.

signal branch is directed to a circuit for external triggering. SP1 DC signals bypass the triggering circuit and are connected directly to their corresponding GRT4 input channels. Signals which contribute to the trigger signal are subjected to processing by timing filter amplifiers (TFA), which amplify the signals and preserve their leading edges. The fast leading edge is then fed into a constant fraction discriminator (CFD). An appropriate CFD threshold of ~60keV was chosen in order to minimise triggering from background, providing a logic output signal whenever the threshold was exceeded. The output of the CFD for each individual signal is then received by a logic unit which generates a pulse that is dependent on the condition of the CFD state. A logic state of 1 at this stage indicates the collection of charge by an individual electrode.

All logical expressions from the CFDs for the AC signals from SP1 are tested by one single OR gate. Therefore, if a single SP1 AC electrode fires, the output from SP1's logic unit is true. The CFD output from each auxiliary detector core also gets digitised and tested by one OR gate. Therefore, if a single auxiliary core fires, the output from the auxiliary detectors

composite logic unit is also true. Finally, these two states are then logically tested by one single AND gate so that if one or more SP1 AC electrode fires and one or more auxiliary core fires in coincidence, the final logic trigger is set to true. The system is then tested for busy with the inhibit signals that create system dead time. If the system is free, digitised data were recorded by the GRT4 cards and sent to a SDLT.

3.6 Experimental Measurements

The principal focus of the coincidence experiments is to characterise the response of SP1 to radiation interactions which are well-defined in three dimensions. Ideally, high counting statistics would be available from ninety-degree scatters at all points from within the detector active volume. Unfortunately, this is not the case and a compromise has to be struck. The critical objective is to quantify detector response with single site interactions. This can be achieved without secondary collimators (section 3.4). A simplifying assumption must be made here, namely that real charge response is not affected by lateral interaction location and is only a function of depth. The validity of this assumption, and the quality of the data collected in this fashion can be verified with more intricate data that are sampled at well-defined positions in the detector with the aid of secondary collimation. The experimental procedure is then a combination of two distinct stages. Stage one can provide replete and excellent characterisation data that can be compared against previous work, and perhaps more importantly, it provides data that can be used for a basis data set[2]. Stage two comprises of a coincidence scan which only accepts ninety degree scatters through secondary collimators. These data are also utilised in chapter 5 to test a new digital Compton rejection technique.

3.6.1 Experimental Notation and Pre-Sorting

All data are pre-sorted prior to analysis for the purpose of categorising events. This introduces new notation and very basic signal analysis. Each signal must be checked for

[2] A basis data set contains average signal response from well-defined interaction locations and will be presented in the following chapter.

content in terms of real charge, transient-induced charge or noise. This requires a baseline[3] difference calculation. An average of the signal offset is calculated using the signal elements before the interaction occurred, usually 1000ns before the leading edge. This is then subtracted from every sample in the signal, and the standard deviation of the signal noise is calculated over the same 1000ns division. A second average of the signal over the latter time divisions is then calculated, if the signal is real, this would be the signals' 'baseline energy' or average pulse height. A comparison between the baseline energy and the standard deviation of the signal noise is used to classify the signal type. If the baseline energy is greater than three standard deviations of the signal noise, the signal is almost (99%) certainly a real charge otherwise it is transient-induced charge or noise.

Once all signals for a particular event from a single detector have been analysed, it is possible to use notation to classify that particular event so that pre-sort gates can be applied based on the number of real charges in that event. If a photon interacts via photoelectric effect, the response of the detector is the collection of a single charge cloud on a single AC strip and a single charge cloud on a single DC strip. This event can then be classified as a fold 1 event. This is also a multiplicity 1 event because only one interaction occurred. However, if a photon enters a single SP1 closed-face-pixel and scatters in that pixel only to be absorbed in the same pixel, the event is also said to be a fold 1 event, when the event is actually a multiplicity 2 event because two interactions occurred.

The fold of the event is therefore classed as simply the number of closed face pixels which collected real charge e.g. one AC electrode and one DC electrode triggering is fold 1, two AC electrodes and one DC electrode triggering is fold 2, *et cetera*. The multiplicity of the event is simply the number of interactions a photon undergoes in the crystal. Geant4 simulations (appendix A) have been performed to investigate the relationship between fold and multiplicity at 662keV. It has been found that 60% of multiplicity 2 events are wrongly identified as fold 1 events. This is assuming that the only way to identify a scatter is to analyse the trigger pattern of the electrodes. False event identification will clearly affect Compton camera performance and a new method of identifying Compton scattering in single closed-face-pixels is needed (chapter 5).

[3] If a preamp has not fully discharged from a previous interaction the next signal will sit on a very small offset, hence the signal has a variable baseline.

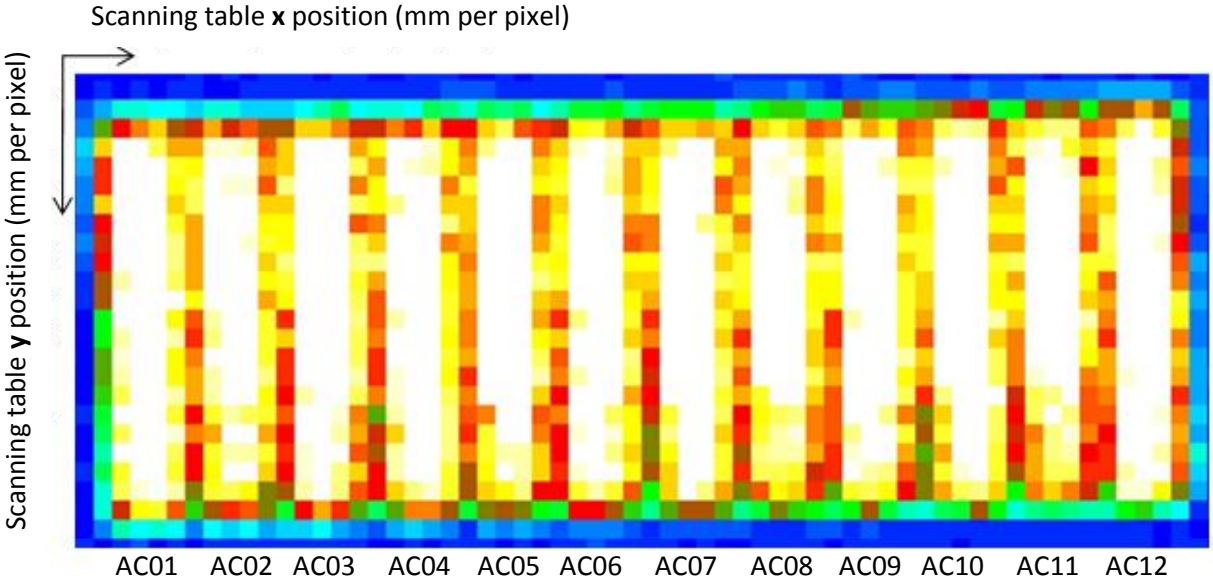

Figure 3.8: Intensity matrix (most intense element shown in yellow, least intense element shown in blue) from the singles scan in which the number of fold 1 events per scanning table position is shown. The beam was shone across DC strips and along AC strips. Scattering in AC strips is therefore a function of collimator position and as a result AC electrode segmentation is clearly visible. The scanning table position was incremented in 1mm steps along both the x and y axis. Each pixel represents 1mm^2 and the depth of interaction is represented by the y axis.

3.6.2 Singles Scan

Before the coincidence measurements can proceed, it is necessary to scan the detector in singles mode, which simply involves firing collimated photons into the crystal of SP1 over a range of positions. Events are recorded as a function of scanning table position and an intensity matrix of the number of events per position is generated. The scanning table x-y step size was 1mm and only fold 1 events were recorded, hence the moniker 'singles', in which only 'single' interactions are of interest. There is actually no scientific definition of a singles scan and the term *singles* can equally be attributed to the use of a single detector. However, keeping these two key points in mind, the resulting intensity matrix is crucial for the calibration of the scanning table position against the crystal position. The matrix shows the relative scanning table positions at which the crystal is being exposed to the primary collimator beam and not the absolute positions in the crystal. This also shows whether or not the crystal is aligned along the x and y axes of the scanning table.

A ^{137}Cs source was used, and additional gates around the 662keV photopeak were applied. Fig. 3.8 shows the resulting intensity matrix. Interpretation of the matrix requires a brief reference to Fig 3.5, in which it can be seen that the beam is shone along the AC strips and across the DC strips. The closest DC strip to the primary collimator aperture was DC01.

Compton scattering across strip boundaries is significantly more probable when the first interaction occurs near a strip boundary. This affect results in a drastic reduction of fold 1 events when the collimator is shone along AC strip boundaries. Scattering across DC strips is not a function of collimator position, which explains why only the AC electrode segmentation is visible in Fig. 3.8 and DC segmentation is not.

Crystal misalignment and crystal size are two other key features that can be extracted from Fig. 3.8. The crystal is misaligned by 1mm in 120mm, representing a rotation of 0.47^{o} about the corner of a crystal. This does not have an appreciable effect on the primary collimator's travelling distance through depth at a fixed translation, or through a single strip translation at a fixed depth. Alignment along the scanning table y axis was performed manually by rotating SP1 about a wooden pivot placed underneath the dewar (Fig. 3.6). The rotation error was minimised by repeating attempts to align the dewar. However, this does not necessarily translate into crystal alignment, given that the crystal might not be aligned with the cryostat casing. Ultimately, the alignment error is within the beam diameter and shall be neglected in all subsequent work. The crystal also appears to be larger than it physically is (20x120 pixels in x and y). An explanation of this effect is given in previous work [Gro05] as the beam divergence, this is a feasible explanation backed up by the intensity of events through depth, which consists of only 21 significant pixels (21mm). Crystal orientation is presented again in chapter 4, including a quantitive assessment of the crystal location and matrix intensity. Fig. 3.8 simply represents the best attempt to align the crystal.

3.6.3 Uncollimated Coincidence Scan

Data acquisition now incorporates the auxiliary detectors triggering in coincidence with SP1 without secondary collimators restricting the scattering angle. This condition is true for all runs recorded during the uncollimated coincidence scan. This scan is justified by the relatively large count rates and high probability of single site interactions. All x-y scanning table positions for which the collimator shines into the crystal have been scanned, even positions for when the collimator was slightly beyond the crystal have been scanned. The positions recorded include all of the x-y positions displayed in Fig. 3.8. The same 1mm step size per position has been used so that 1 pixel represents $1mm^2$. A direct comparison with

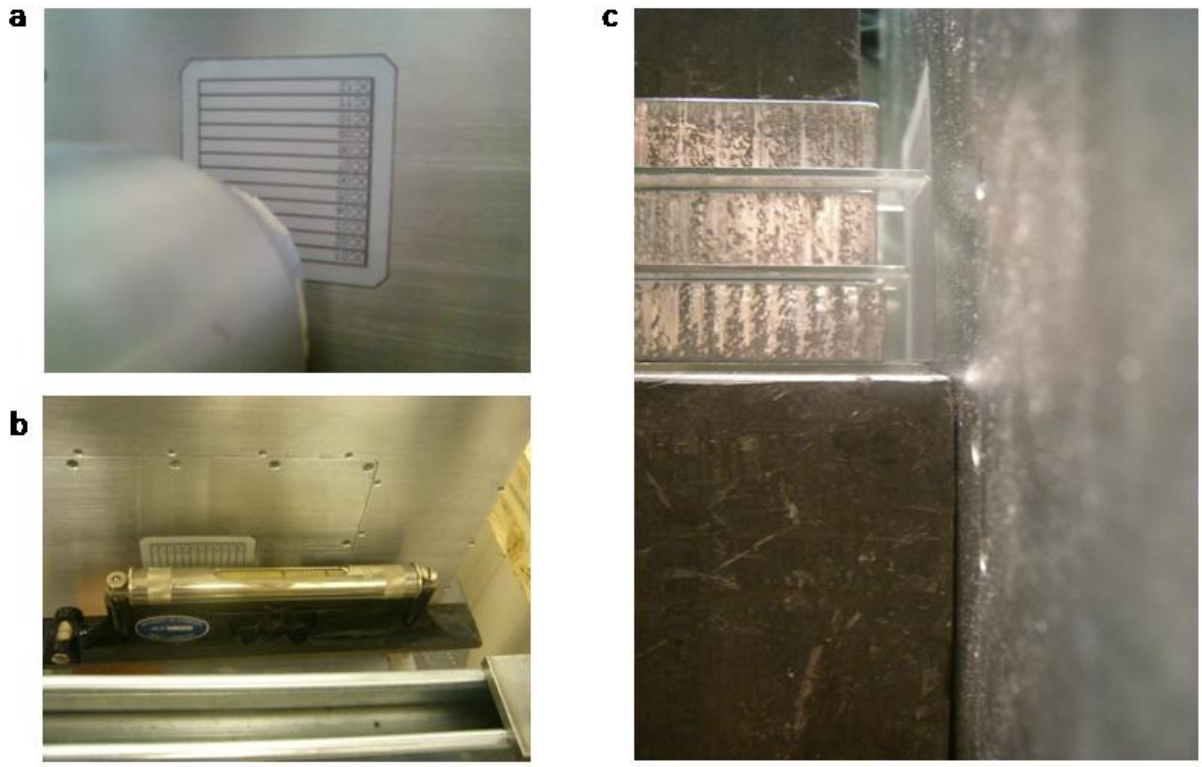

Figure 3.9: Images taken during the experimental set-up of the coincidence scan. Image (a) shows the PT6X2 directly facing the DC electrode face of SP1. Image (b) shows the engineering spirit level used to align the secondary collimators with the crystal edges of SP1. Image (c) shows the secondary collimators forming a stack of different sized lead blocks, separated with shims. This secondary collimator stack sat between SP1 and an auxiliary detector.

previous work, that also scanned all positions in 1mm steps, is possible by performing such a comprehensive scan. The crystal was aligned for the singles scan and remained static for every other experiment. Only the auxiliary detectors needed experimental adjustment during the uncollimated scan. See Fig. 4.9a for images of the PT6X2 facing the cryostat aluminium window of SP1. Only the PT6X2 sat tight against the cryostat, whilst the M6X6 sat 60mm away due to obstructive structures. A ^{137}Cs source was used for the primary beam, and the data were gated on fold 1 events which 'added-back' to 662keV. Two other gates were applied and are explained in chapter 4. A total of 1320 positions were scanned at 147 seconds per position resulting in 128GB of raw data. See section 4.4 for analysis results.

3.6.4 Collimated Coincidence Scan

Data acquisition varied from the uncollimated scan only because secondary collimators restricted scattering angles to ninety degrees. Both the PT6X2 and M6X6 sat 75mm away

from the cryostat of SP1 behind a stack of lead bricks. A number of runs were recorded in this configuration and are partially analysed chapter 4. The same fold 1, add-back gate and extra gates apply as in section 3.6.3. Each run was composed of a selected number of scanning table positions at fixed secondary collimator positions. A new run was started if the secondary collimators were adjusted vertically in the z direction. The secondary collimators were moved across the face of SP1 so that induced transient charges could be examined as a function of lateral position. A total of 6 runs were performed, each with various scanning table positions, but with a common count time of 7200 seconds per position. Only a small amount of data were generated which was drastically reduced when the gates are applied. This was not surprising given the separation of the crystal of SP1 and the auxiliary detectors.

3.7 Initial Performance

Energy resolutions, coincidence spectra and 662keV add-back event rates have all been investigated as initial parameters of the coincidence experiments. Subsequent work relies on good performance for each of these critical features. The Compton camera requires good energy resolution and efficiency, whilst the coincidence data that are used to calibrate SP1 for spatial resolution requires sufficient statistics and narrow energy gates.

3.7.1 Energy Resolution

Detector energy resolution measurements have been performed with sealed ^{137}Cs, ^{60}Co and ^{57}Co point sources, the results of which are presented in Tab. 3.1. The detectors were operated at manufacturer-recommended voltages (SP1 = -1800V, PT6X2 = +3200, M6X6 = +4000). For statistical purposes a total number of 10000 counts were recorded in each photopeak. DC11 had exceptionally poor energy resolution due to a known *charge sharing* problem. Individual energy resolutions for SP1 are not quoted but the average energy resolution improved from 1.71keV to 1.32keV at 122keV when DC11 was excluded from the measurement. DC11 had an individual energy resolution of 4.6keV at 122keV. In previous work [Tur06] it has been excluded, but it is not neglected at any other point in this work.

The M6x6 has good spectroscopic properties and it is a little unfortunate that this detector could not be mounted tightly against the cryostat window of SP1 due to mechanical constraints. The PT6X2 has good average energy resolution from its core signals considering the large neutron flux it was exposed to. It did however have low-energy tailing indicating incomplete charge collection, possibly due to lattice damage. The FW.1H is included for the PT6X2 to assess this tailing, which is actually the only study of its spectroscopic properties since it was neutron-damaged. However, avoiding a tangential study, the energy resolution of the PT6X2 indicates that it is a suitable auxiliary detector.

Detector	Energy (keV)	FWHM (keV)	Resolution (%)	FW.1H (keV)
SP1 (Avg.)	1332	3.95	0.29	
	1173	3.33	0.28	
	662	2.15	0.32	
	122	1.71	1.4	
PT6X2 (Avg.)	1332	2.91	0.22	6.54
	1173	2.79	0.24	6.62
	662	2.41	0.36	4.41
	122	2.07	1.7	3.19
M6x6	1332	2.37	0.18	
	1173	2.25	0.19	
	662	1.72	0.26	
	122	1.22	1	

Table 3.1: The initial performances of the primary and auxiliary detectors are presented. It can be seen that the neutron damage to the PT6X2 is not significant in terms of its energy resolution. SP1 will need optimising for work in subsequent chapters.

3.7.2 Coincidence Spectra

An initial experimental run was performed to check count rates, DAQ, scanning table software control and the amalgamated detector performances under coincidence conditions. This involved controlling the scanning table by moving it underneath SP1. Only twenty-four arbitrary positions in total were scanned, at 160-minutes per position. A total of 1,617,544 events were recorded, of this 574,890 met the fold criteria. Therefore, 2.4 counts

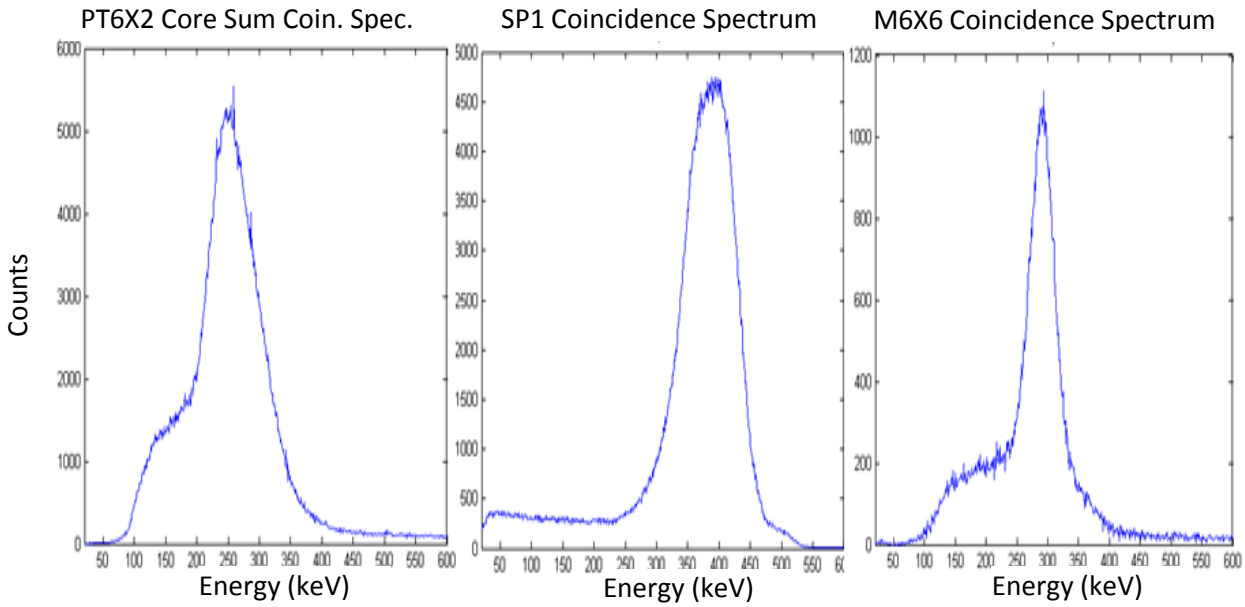

Figure 3.10: These three spectra represent the coincident energy depositions in SP1 and the auxiliary detectors. The central peaks in all images correspond to scattering between SP1 and the auxiliary detectors. The strange plateau in the PT6X2 spectrum and M6X6 spectrum represent events which have scattered in the auxiliary detectors in combination with multiple scatters in SP1, represented by greater than 475keV energy deposition in SP1.

per second without secondary collimation were recorded. The individual energy spectra from each detector are shown in Fig. 3.10.

The energy distributions in Fig. 3.10 are all broad which is an effect of the lack of secondary collimators; a broad range of scattering angles is possible. The PT6X2 has a greater number of counts than the M6X6 which is what would be expected from the geometry of the experiment, in which the M6X6 was further away from the cryostat. Median energy deposition in SP1 does not correspond to 90^{o} scattering. This is explained by the position of the PT6X2 which was placed at ninety degrees to the cryostat at an awkward angle so that the PT6X2 crystal axis was not normal to the face of the crystal of SP1. Hence, favoured scattering angles would not have been symmetric about ninety degrees, but offset. Another key feature in Fig. 3.10 is the slope on the tail of the PT6X2, this can be attributed to the high energy appendage in the SP1 spectrum. Single scatters have a maximum energy deposition in SP1 of 475keV, events above this energy must scatter at least twice. These types of events would deposit less energy in the PT6X2. This is compounded by the fact that events scatter out of the PT6X2. The FWHM is therefore not a valid measure of energy resolution because the peaks do not relate to discrete energies.

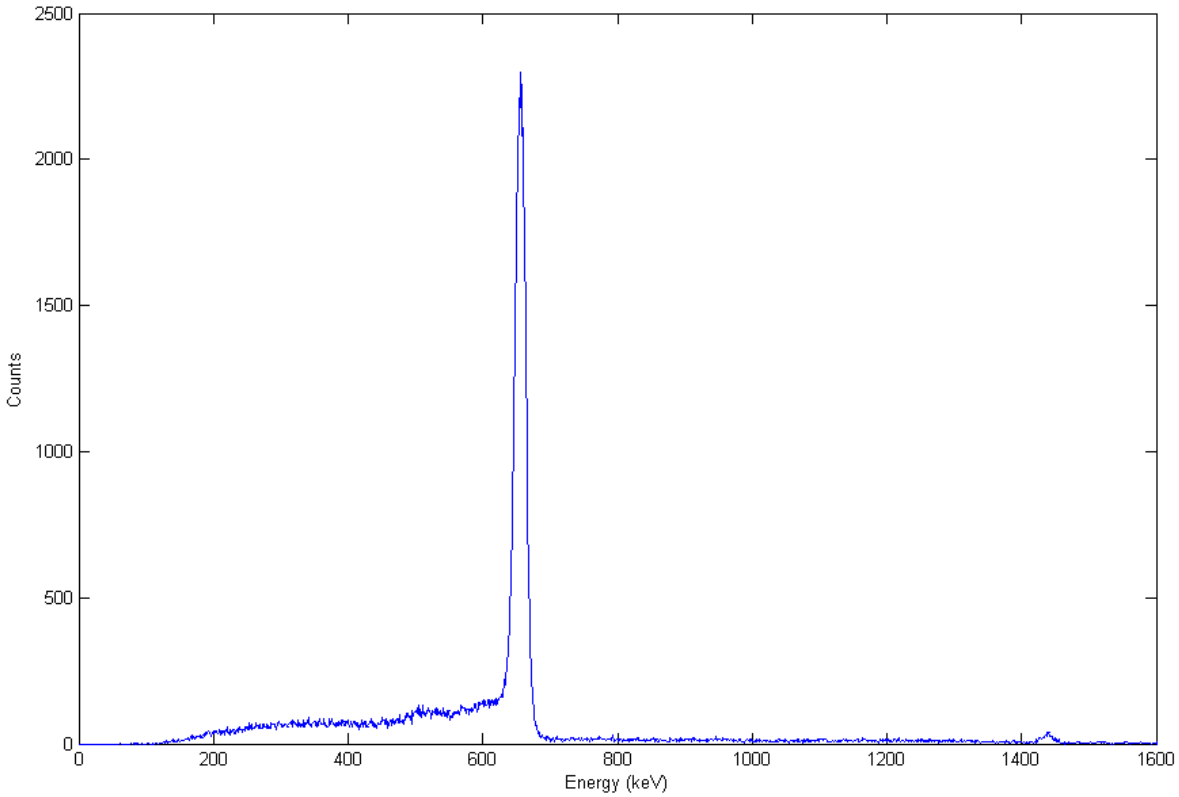

Figure 3.11: Add-back spectrum from the initial test of the coincidence experiment. The scanning table was not included in the DAQ and neither were the secondary collimators. The primary beam energy was 662keV which has clearly been reconstructed. The tail from the 662keV peak consists of scattering events. The 1460keV peak arises from ^{40}K.

3.7.3 Add-back Spectrum

The coincidence test measurement that was presented in section 3.7.2 has been used to produce an add-back spectrum which is shown in Fig. 3.11. The gates used for the spectra of Fig. 3.10 were applied. But not all scanning table positions have been included. This gives an indication of the count rate of useable counts. However, it is clear from Fig. 3.10 that a small fraction of SP1 fold 1 events are actually multiplicity 2, and the analysis proper, presented in chapter 4 requires additional energy gates so that not all events in an add-back spectrum are analysed. Reconstructed 662keV events can be seen in the 'photopeak' of Fig. 3.11. A 1460keV peak can also be seen, which results from the occurrence of ^{40}K in concrete. The FWHM of the 662keV peak is 11keV; this is optimised in chapter 4. Although energy resolution is clearly a primary concern from the point of event selection, it does not have a great significance for the analysis of detector response. Signals are normalised to unity early in the analysis chain and the signal shape becomes the only point of interest. The experimental measurements discussed in this chapter are now analysed in the next chapter.

Chapter 4

Coincidence Scan Analysis for Spatial Calibration

Analysis of the experimental data arising from the previously described coincidence measurements is presented in this chapter. Statistics hugely favoured the uncollimated scan and the analysis primarily focuses on this accordingly. The ultimate aim is to utilise the theoretical concept of the weighting field (section 2.7) to increase the effective granularity of the detectors. A semi-empirical pulse shape analysis approach is taken that identifies inherent signal characteristics which are unique to specific interaction locations from within the active volume. In addition, a partial experimental basis-data-set was constructed allowing a correlation coefficient to indicate the most probable interaction location of unidentified signals. The basis-data-set has also been used to reconstruct multiple interactions allowing a test of the technique presented in chapter 5, which can be used to identify scattering in single closed-face-pixels. Charge sharing events have also been reconstructed, which have important implications for detector sensitivity. Data analysis from the secondary collimated measurements provides a justification of the results derived from uncollimated data. The secondary collimated data is also used in chapter 5.

4.1 PSA Methods

The principal concept of at the heart of pulse shape analysis is the geometric dependence of a weighting field (section 2.5.2) which is reflected in the charge pulses that are generated by

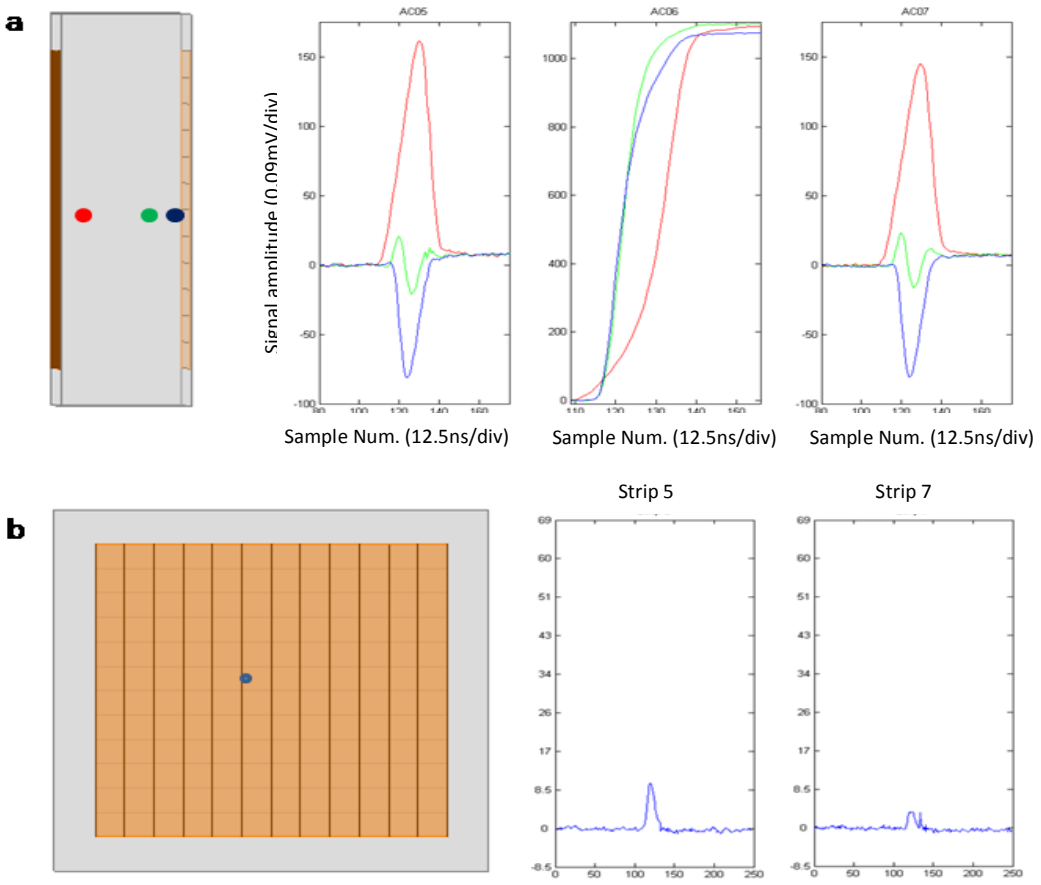

Figure 4.1: Diagram showing how the geometrical variation of the weighting field is reflected in signal shape. Image (a) represents signal changes through depth. Image (b) represents lateral interaction response on spectator electrodes, where the interaction that is in strip 6, is actually closer to strip 5 than strip 7.

ionising radiation. Analysis of detector signal pulse shapes thus increases the effective granularity of the detector. Example SP1 signals for a real charge and accompanying transient-induced charges from spectator electrodes are shown in Fig. 2.13. These signals are for a 'single' interaction event. Position sensitivity relies on signal variation between this interaction location and a different interaction location. Examples of signal variation through depth and lateral translation are shown in Fig. 4.1, in which only the response of the AC electrode is shown. Image (a) shows signal variation through depth for three positions. The majority carriers will dominate the charge collection process. Therefore, the slow initial rise of the charge pulse of the red signal can be interpreted as the resultant of charge liberation at a location in which the majority charge carriers have a large drift time to the collecting electrode. Similarly, the rapid rise of the green and blue signals would indicate an interaction at a location in which the majority carriers are close to the collecting

electrode, and the majority drift time is short. The response of the transient-induced charges on spectator electrodes, as shown in Fig. 4.1, is understood in reference to sections 2.5 and 2.6, in which the weighting field is extended through the crystal depth and has three distinct regions. Image (b) shows how the response of the transient-induced charge signals changes with translational variances at constant interaction depth, with weaker coupling between the weighting field and spectator electrode at greater lateral distance or stronger coupling at shorter distances. This can be seen in Fig 2.10 in which the field intensity drops rapidly as a function of distance at a constant interaction depth for a given spectator electrode. Four principal methods of extracting position information from detector signals are reported in the literature, two of which involve analysis of the current pulse and not the charge pulse as shown in Fig. 4.1. The first three methods described below are solely related to spatial resolution in depth. The use of transient-induced charges is relatively new and is the final method described.

4.1.1 Time-to-maximum

The time-to-maximum method analyses the current pulse which is directly affected by the motion of charge carriers in the detector. The current signal is experimentally obtained as the time derivative of the charge signals. Current flows through the electrode immediately after an interaction to keep the potential constant. The electron and hole clouds then drift towards their corresponding electrode. Electrons are the majority charge carriers in SP1. The electrons drift towards the AC side and the electrostatic coupling increases, leading to a continuously rising current. Holes drift away from the AC side and their current decreases as a function of time. Majority charge carriers dominate the signal and the final majority current (or minority current), i, is given as a function of drift time, t.

$$i(t) = Q\frac{E(r)}{V_{bias}}.v_d\big(E(r)\big) \tag{4.1}$$

where Q is the charge liberated by the interaction, V_{bias} is the applied potential, $E(r)$ is the electric field as a function of position and v_d is the drift velocity. If the drift velocity is constant then the current is basically a function of interaction location. A simulation of current pulses for SP1 is shown in Fig. 4.2. The current stops growing once the majority

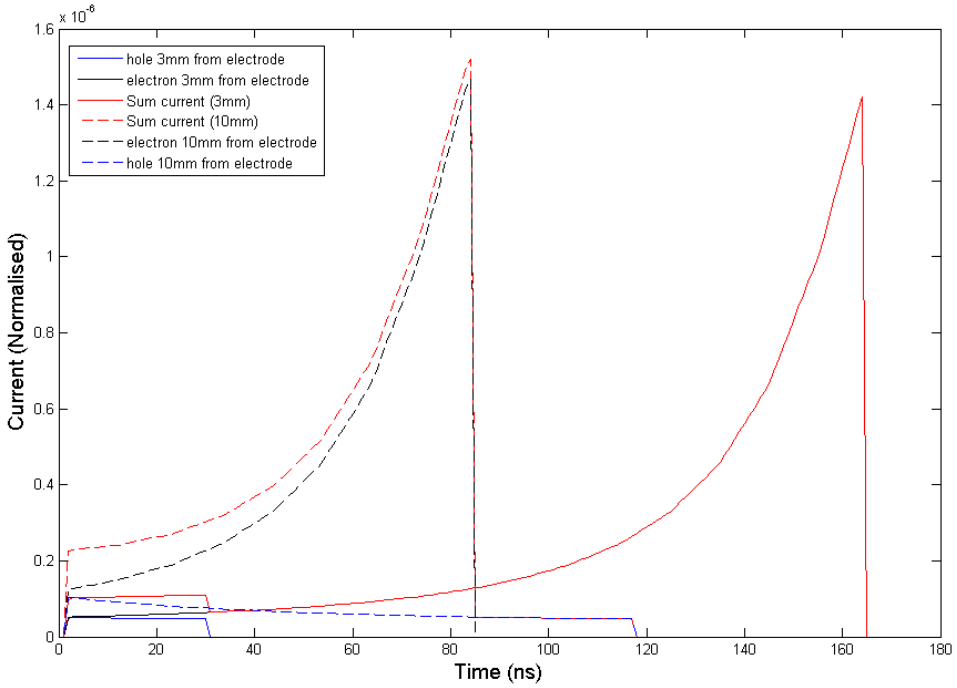

Figure 4.2: Simulated current pulses for two spatially separate interactions. The electron current (majority carrier in an n-type) is shown along with the hole current (minority carrier in an n-type) and net current. This demonstrates the time-to-maximum method.

carriers are collected. Therefore, the time-to-maximum of the current pulse is related to the distance of the initial interaction from the electrode. The practical implementation of this method resulted in a spatial resolution of ~8mm at 356keV in a 50mm diameter detector [Sch92]. However, the maximum was found offline by fitting the data and this method cannot realistically be used online, besides the resolution of a Compton camera needs to be significantly better than 8mm.

4.1.2 Steepest Slope Method

Another potential technique for determining the depth of interaction is the steepest slope method [Gam97]. The differential of the current pulse is calculated and the largest rate of change of the current pulse is then assumed to indicate the collection of the majority charge carriers has ceased. If the current pulse is composed of multiple interactions, then in theory this technique should also indicate the collection of a second majority charge cloud. The largest interaction would create the largest charge cloud, and therefore the largest rate of change would indicate collection of the largest charge cloud. Preamplifiers have been

specifically designed to test this method. A similar technique to this method in which the number of maxima or majority charge clouds in the current pulse indicate the number of interactions is currently under development for AGATA [Cre07]. This method has been tested on simulated data, and also in-beam data coupled with a Geant simulation. In both cases the method has shown promising results with approximately 80% success rates for simulated data. Attention is drawn to this method because on a fundamental basis it is strikingly similar, but developed independently, to a technique introduced in this thesis. However, although the ideas behind these two techniques are similar, the practical implementation is somewhat dissimilar. The technique developed in this thesis was driven by noise considerations, which is in contrast to techniques based primarily on current pulse formation.

4.1.3 Rise Time Analysis

Although the majority carriers dominate the detector current pulses, the minority carriers also make a significant contribution, and the entire pulse shape is considered for rise time analysis in the form of a real charge pulse, as described in the opening of this section. Depth of interaction information is contained in the rise time of the signal and how to best utilise this information is the subject of a number of papers describing different parameters. Because the response of the preamplifier is complicated it is simpler to analyse the final charge pulse than dissociate the complicated response of the preamplifier. The depth of interaction can be determined by the *rise time* difference between both real charges from the collecting cathode and anode; the time taken to reach 50% of the signal magnitude is taken as the reference point [Vet04]. This method has already been successfully applied to SP1 [Gil07].

Other parameterisation involves individual real charge analysis in which a time parameter is used to characterise the rise time of a single signal. A common parameter is $T90_x$ which is the signal *rise time* between some reference fraction of the signal amplitude, x, (usually 10% to avoid noise) to 90% of the signal amplitude (usual notation is t_{10} for 10% of the signal amplitude and t_{90} for 90%). Because the fastest charge collection times occur in the central depth due to almost equal collection times for holes and electrons, or to be precise

slightly off centre because carrier mobility is not equal, the resulting $T90_x$ distributions have an ambiguity resulting from symmetry about this point. $T90_x$ *rise times* fall towards the depth of fastest charge collection and then increase so that two different depth positions may have the same *rise time*. The ambiguity of the signals' partial *rise time* can be resolved by sampling $T90_x$ and $T30_x$ as first described in [Kro96]. Each parameter is then plotted in a matrix containing unique features for individual depths.

4.1.4 Asymmetry Analysis

Rise-time analysis is generally accepted as the simplest method that can be utilised to extract the first coordinate for the position of interaction within the active volume, namely the depth of interaction. The transient induced charges can then be used to extract lateral position information using the asymmetry parameter for the remaining two coordinates (section 2.7.1). This information is only relative to the two next nearest neighbouring spectator electrodes of the collecting electrode, and needs to be calibrated relative to the spectator strip boundaries with the collecting electrode. Additionally, equation 2.38 is adjusted so that spectator electrode comparison is performed using transient induced charge area. This is solely based on an evaluation of the noise in SP1. It has not been feasible to accurately define single signal amplitudes if the signal is convolved with high frequency noise. Therefore, the asymmetry parameter is:

$$R = \frac{A_{left} - A_{right}}{A_{left} + A_{right}} \tag{4.2}$$

where A is now an area placed around elements of interest, which are expected to contain the transient induced charge signal. This is simply a 125ns window placed around the centre of a signal trace. Further simplifying assumptions are made, building upon the material in section 3.6.1, that if a real charge is identified and the event is fold-1, then the next nearest neighbours explicably contain transient induced charge and should be analysed accordingly.

4.2 Intrinsic Limitations

Empirical calibration of the system for spatial resolution has a number of fundamental limitations. Understanding these limitations is important if the results are to be interpreted sensibly. For example, the collimator position does not always reflect the x-y position of interaction within the active volume due to collimator penetration, and caution should be taken in assuming the position of interaction is absolutely well-defined. The collimated beam also diverges as a function of distance from the collimator aperture, and interaction location is less well defined for DC strips away from DC01. More intrinsic spatial resolution limitations are inherent due recoil electron ranges, which is 0.3mm at 662keV.

4.3 Experimental Pre-processing

Raw charge signals require pre-processing before partial rise times can be extracted from the leading edge, principally because it is difficult to calculate the maximum signal amplitude from a single signal peak, and therefore it is also difficult to calculate t_{10} or any other time parameter. Once baseline energy calculations are performed (section 3.6.1), the chain of pre-processing begins with an energy calibration of each electrode used in the coincidence scan. Pre defined gain coefficients are used for the calibration and the fold of an event is subsequently determined. Reliable classifications of event types are made, and each 'good' event is passed through to the remaining experimental pre-processing chain. Only fold 1 events are processed further, all other folds are rejected by the analysis codes.

4.3.1 Decay Correction

The Signals are corrected for the exponential decay of the charge sensitive preamplifiers. This is only necessary for SP1 signals because auxiliary signals are not used in the analysis. The decay correction equation is given by:

$$x(t) = x(t)\left(1 - e^{-t/\tau}\right) \tag{4.3}$$

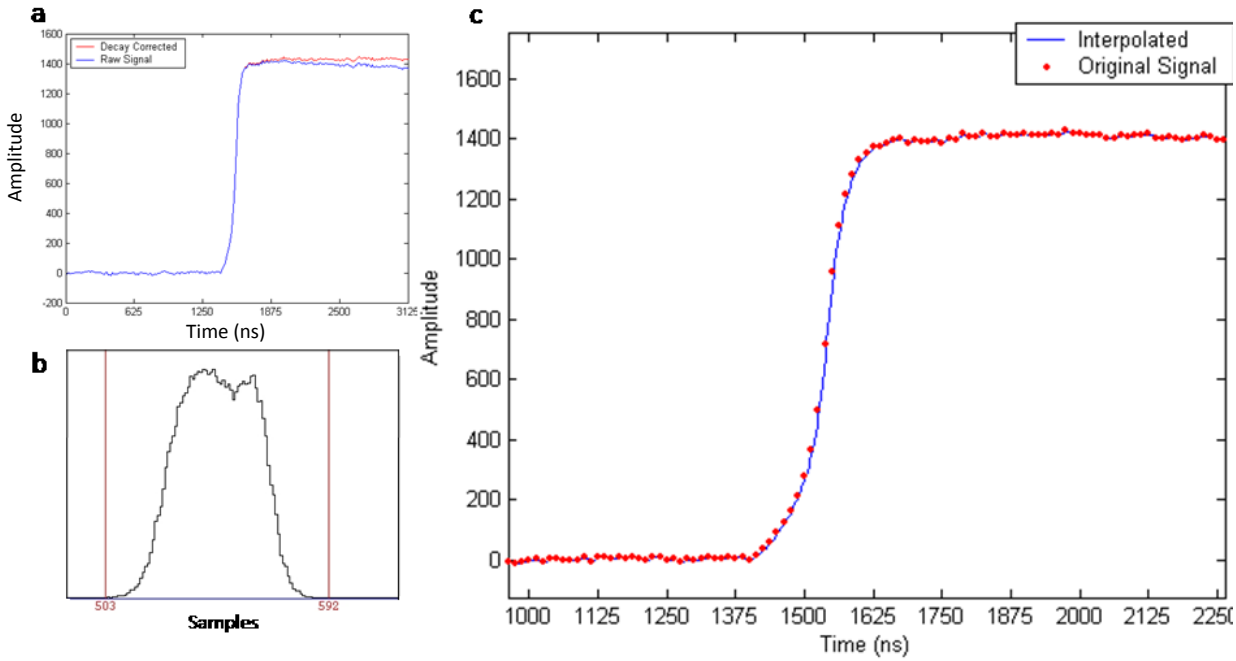

Figure 4.3: Pre PSA processing. Image (a) shows the decay correction necessary to determine the signal amplitude. Image (b) shows a histogram of t_5 (time coordinate when signal crosses 5% of the signal maximum) signal element numbers for individual signals from the uncollimated scan. The t_5 values drift over 60 signal elements, which translate into 175ns. This drift can be attributed to a combination of CFD and GRT4 walk. Image (c) shows an example of the interpolation. The red dots are the original values; the blue line is a linear interpolation between the values.

where $x(t)$ represents the signal at increment t (every 12.5ns) and τ is the decay constant of the preamplifier, calculated to be 43µs. The resulting signal 'flat-top' makes an estimate of the signal amplitude (t_{100}) more accurate and hence gives better parameterisation of partial rise times. A decay corrected signal is shown in Fig. 4.3a.

4.3.2 Interpolation

The discrete nature of a signal clearly provides two possible candidates when sampling t_{10} or any another time parameter, between which the 'true' value of t_{10} can be found. One value is greater than the true t_{10} value and the other is less than the true t_{10}. Therefore the signal is interpolated with a linear fit, expanding the number of data points by a factor of five, or reducing the uncertainty by a factor of a fifth. The original 250 sample signal representing 3125ns is now represented by 1250 sample points, so that each sample covers 2.5ns. An example interpolation is shown in Fig. 4.3c. The red dots represent the original signal and the blue line represents the interpolated signal. The interpolation function is

called directly after the decay correction function in the C code. A linear fit was chosen because it is the easiest to implement.

4.3.3 Time Alignment

During data collection, the triggering signals from the CFD walk so that two identical interactions at the same interaction location will trigger at slightly different times. A contributory factor to this effect can be attributed to the variation in signal shapes from SP1 and the auxiliary detectors. The resulting signals are not aligned in the reference frame of a fixed signal window. A spectrum of the variance of t_5 for individual SP1 signals for a particular scanning table location can be seen in Fig. 4.3b. This is easily compensated for in respect to real charge analysis. A standard reference point for t_5 is arbitrarily chosen as the 545^{th} signal element. All individual values of t_5 are then calculated and shifted so that they overlap with the standard reference point. All transient-induced charges are then shifted by the same number of elements as their corresponding real charge.

Although real charges are now well aligned, it cannot be assumed that the same shift aligns the transient-induced charges with the same precision. This is the result of another important source of signal walk, and it is generated by the architecture of the internal clock within the GRT4 cards. When a global trigger signal is received by the GRT4 cards, each channel is recording according to the time of that particular channels clock. Unfortunately, each clock is slightly out of sync and therefore each signal is slightly out of sync. The real charges are forced around a standard reference point. However, this is impracticable to do for the transient-induced charges. No correction can be made for this drift until the new electronics, which have a master clock, are used for DAQ. No attempt has been made to quantify this source of drift, but it is a few nanoseconds in magnitude. It is worth noting that t_0 could be estimated by summing all SP1 electrodes if the channels had a synchronomous master clock, because all electrodes respond simultaneously and the mean noise is zero.

4.3.4 Average Response

At this stage all signals have been stamped with their energy so that it is possible to normalise all signals to 1, making their analysis energy independent. The final stage before analysis is then to sum all signals which have passed selection criteria. The purpose of this stage is to create destructive interference of individual noise, thus reducing the standard deviation of the noise in the final average signal. One final criterion is applied to the data before the signals can be summed, this critical function is built into the pre-processing C codes and restricts summation based on a comparison between the primary collimator position and the triggered strip. If the collimator is preventing gamma rays from illuminating a particular AC strip which then triggers, then the event is discarded because the interaction location is clearly unknown. A picture of the average response of the detector to interactions at specified locations is then built up. All initial analysis is performed on average signals but the methods are eventually applied to individual interaction signals.

4.4 Uncollimated Scan Results

Results and analysis from the uncollimated scan described in section 3.6.3 are now presented. As described, the crystal of SP1 was scanned through depth using all x-y scanning table positions defined by the primary collimator. The resulting intensity matrix is show in Fig 4.4. The number of fold-1 events which add-back to 662keV and trigger SP1 in conjunction with just one auxiliary detector are shown for each collimator position; this is a total of 715894 events. The scanning table was incremented in 1mm steps along both axes. The primary collimator approaches the M6X6 detector with increasing y scanning table position, in reference to section 3.6.3 it can be seen that this detector is situated further from the detector crystal than the PT6X2. Hence the count rate is inversely proportional to the distance of the primary collimator on the y axis. The highest count rates are seen in the crystal for positions close to the PT6X2, which sat tightly against the cryostat of SP1. The analysis is primarily concerned with the response of the AC electrode, whilst all DC strips contributed towards the intensity matrix. Further energy gates are required to remove multiple interactions in SP1 from the final analysis.

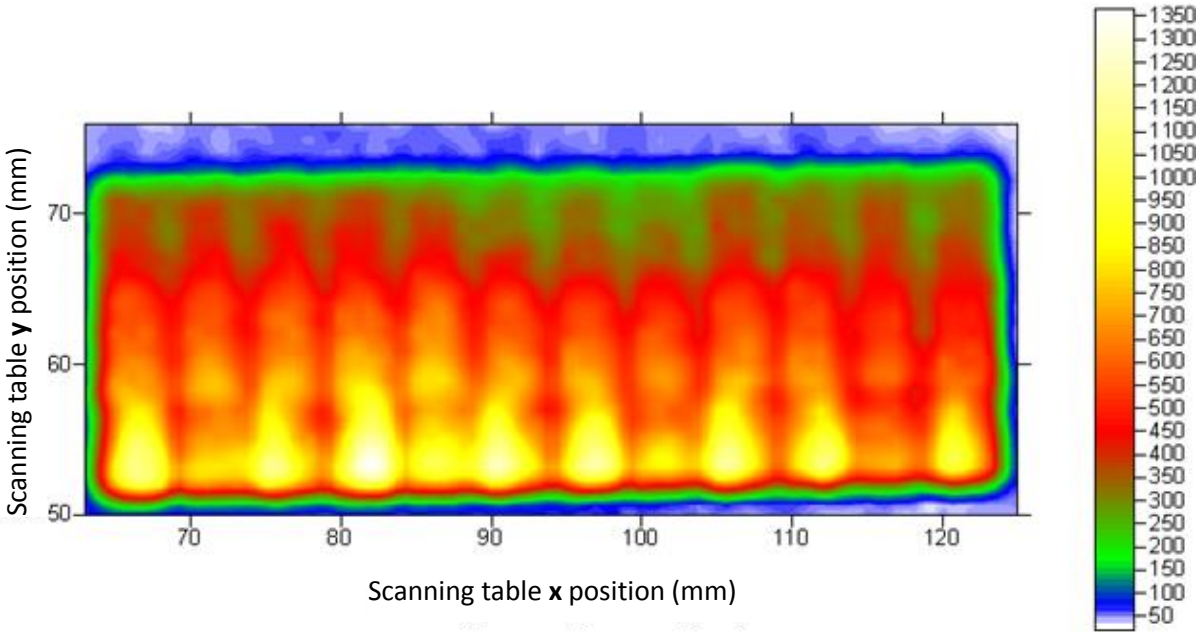

Figure 4.4: Intensity matrix showing the positions scanned during the uncollimated scan; all x-y positions for which the collimator was under the detector crystal were scanned. The scanning table travelled 63mm in the x direction and 21mm in the y direction before the outer corner of the crystal was reached. The 1mm misalignment of the crystal can be seen. Crystal depth is along the y axis. The crystal appears thicker than its actual true thickness of 20mm, but this can be explained by beam divergence. The crystal depth should be interpreted for intensities greater than 400. Strip boundaries are represented by a drop in intensity. It can be determined that AC01 begins at x=64, AC02 at x = 69, AC03 at x = 74, *etc*.

4.4.1 Energy Selection

A coincidence energy matrix containing the energy deposited in the auxiliary detectors indexed against the energy deposited in SP1 for each individual event has been produced to show how further gates can be applied to further increase the integrity of the data. The new criteria require that the energy deposited in SP1 and the auxiliary detectors are within the range expected from angular considerations of the experimental set-up. The position of the PT6X2 detector permits scattering over an opening angle of approximately 140^{o}. Assuming this angle is centred on the normal from SP1, the scattering angles would range from 160^{o} to 20^{o} and energy deposition would range from 474keV - 47keV. The PT6X2 active volume available to these extremes of scattering angles would not be as significant as the volume available for 90^{o} degree scatters, and the efficiency for detecting these scattering angles is small. The actual experimental geometry of the PT6X2 favoured larger scattering angles. This can be seen in Fig. 4.5, in which the majority of energy deposition in SP1 lies between 350keV – 450keV. Events which deposit energies inconsistent with single site interactions are vetoed.

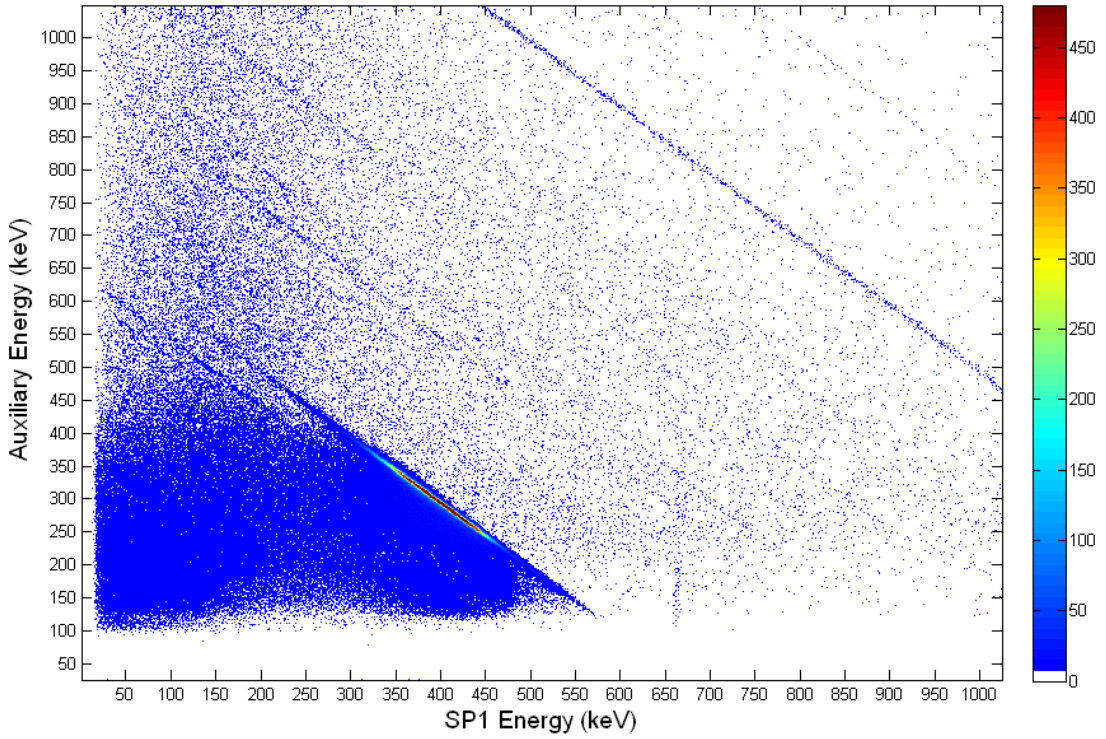

Figure 4.5: Coincidence energy matrix of energy deposition in the auxiliary detectors against the energy deposited in SP1. Useable events appear in the central distribution of the 662keV diagonal line. Other notable features include a large number of scattering coincidences, a vertical 662keV line from random coincidences and the 1460keV line from true ^{40}K coincidences. The maximum number of counts in a single matrix element corresponds to 6841 and not 480 as indicated by the colour bar. The colour bar range has been adjusted to show salient features.

The matrix shown in Fig. 4.5 contains other features which are not present in simple add-back spectra. Events which add-back to 662keV are distributed about a diagonal line that stretches between 662keV on the SP1 energy axis to 662keV on the auxiliary energy axis. Another obvious diagonal line is the 1460keV peak from ^{40}K, which is expected given the intensity of concrete in the laboratory. Other distinguishable true coincidences are present in the energy matrix, these are probably pollution from other experiments. The counts in these peaks are insignificant and do not warrant investigation. A vertical line originating at 662keV on the SP1 energy axis indicates events which trigger in random coincidence with scattered events in the auxiliary detectors, but this effect is negligible.

The mode energy on the 662keV diagonal line is 391keV which corresponds to a scattering angle of $\sim 96^{o}$. A drastic reduction in the total number of counts on this line occurs for SP1 energy deposition below ~310keV and above ~470keV, corresponding to $\sim 71^{o}$ and $\sim 152^{o}$ scattering respectively. In total, 95% of events on the 662keV line lie between these two

energies which fall well within the maximum opening angle for true scatters. The 662keV diagonal continues past 470keV on the SP1 energy axis until ~574keV. Single scattering events are limited to ~477keV at the backscattering angle and therefore cannot be detected in the auxiliary detectors. However, it is possible for an event to scatter twice in a single closed-face-pixel in SP1 and deposit ~554keV rising to ~586keV for a triple scattering event. A total number of 1,042,602 events are binned in the coincidence energy matrix, of which only 429,554 events have been identified as probable single-site interactions. This provides ~350 events per scanning table position which translates as ~2.4 events per second in the DAQ; as expected. Average detector response is well defined with such a large number of events at each collimator position.

4.4.2 Typical Average Response

Fig. 4.6 shows a typical average response of all the strips of SP1 that has been chosen at an arbitrary scanning table position; the scanning table position is actually 76mm along the x axis and 63mm along the y axis. In reference to Fig. 4.4 this position corresponds to collimator shining into AC03. Over 1300 such responses have been measured. The response of every electrode is recorded and stored in a sequential array segment. The first array segment holds the number of events in the mean response and also the AC strip number that was directly exposed to the primary collimator at that scanning table position. All signals are processed in accordance with the processing described in section 4.3. Therefore each array segment is 1245 elements long. By inspection of Fig. 4.6 it can be seen that AC03 is indeed exposed to the primary collimator. Further inspection of the transient-induced charges shows that they are almost equal indicating that the primary collimator was shining almost into the centre of AC03. The insert figure shows the real charge and transient-induced charges in greater detail. The spike which leads the real charge is an artefact of real charge time alignment. Other interesting features show that all DC strips were allowed to contribute to the average response and the total number of interactions falls from DC01 – DC12 exponentially. The poor performance of DC11 is represented by a notable drop in counts on this strip. However, using the number of counts in each DC strip as a function of position allows a determination of the mean free path in germanium (section 2.1). This has

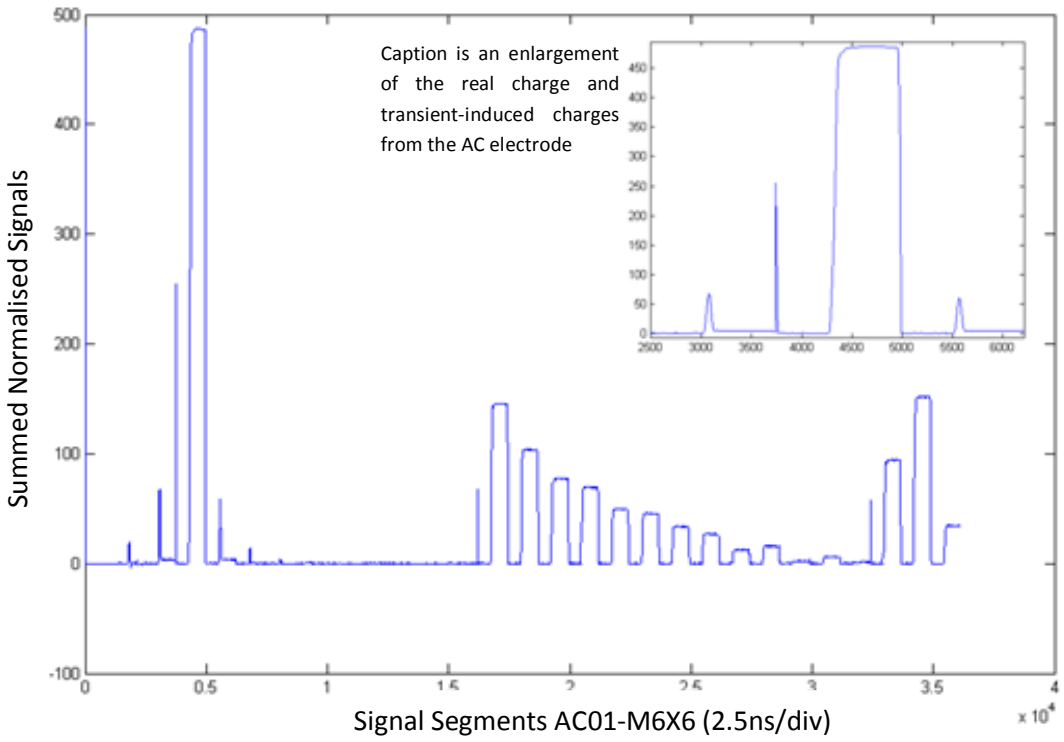

Figure 4.6: Average response from all strips at the scanning table position x = 76mm and y = 63mm. The first array segment (1245 elements) of the 'pulse train' contains the number of events in that average response and the AC strip number that fired. The next 12 segments are the AC strip responses from AC01 through AC12, followed by the next 12 segments which are the DC strips from DC01 through DC12. The remaining four array segments are the guard ring, PT6X2 back contact, PT6X2 front contact and the M6X6. The insert is an enlargement of the AC electrode responses.

been calculated as 20mm, which is close to the expected value of 23mm for 662keV photons. Although this calculation neglects photoelectric absorption, it does imply that the response is not uniformly represented.

4.4.3 Rise Time Analysis

Section 4.1.3 notes that a reference point of t_{10} is usually used to take measurements of a signal partial *rise time* between this point and t_{90}. Although this is true for previous work, this reference point is clearly not fixed and other reference points are investigated in this section. The most desirable reference point would be t_0 because the entire signal rise time could then be analysed, but t_0 is impossible to measure experimentally. The method described in section 4.3.3 should give a reasonable estimate of t_0 but requires the new electronics. Other methods involve a fit of the real charge to find a unique solution of t_0. However, a unique fit of the real charge supersedes the need to find t_0 because a unique

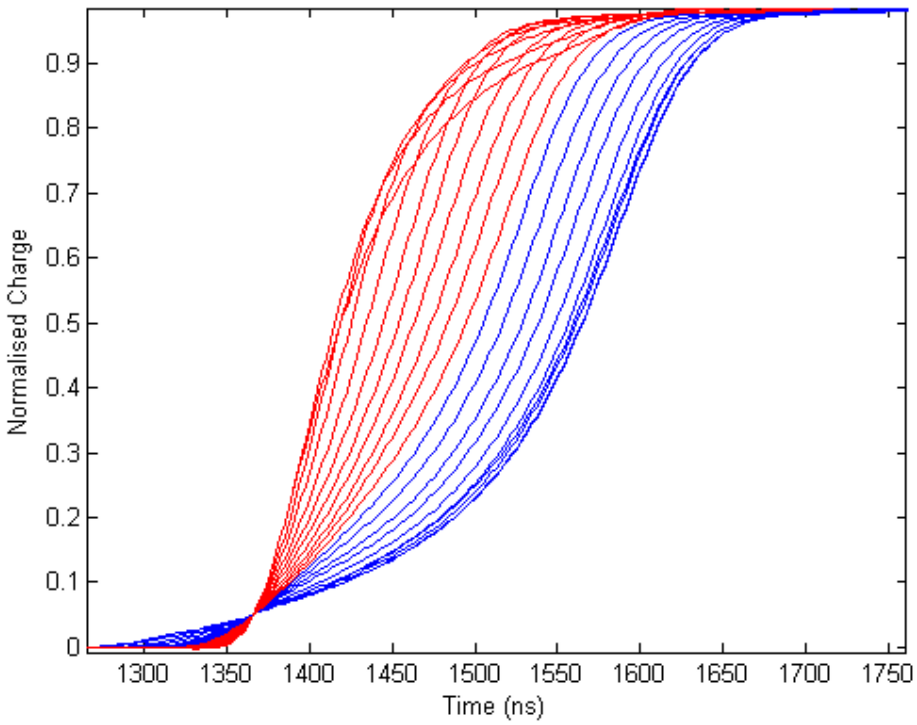

Figure 4.7: Pulse shape variation through 20 depths for a constant lateral position (constant x coordinate in Fig. 4.4) in the crystal of SP1. The variation implies that PSA (section 2.7) can be exploited for SP1. The constant lateral position is x = 91mm, which is equivalent to the centre of AC06.

depth would be calculated by default. However, if PSA is to be applied experimentally to Compton camera data then low energy scatters will need to be analysed for depth information, and t_{10} is a sufficiently large enough threshold to avoid discrepancies due to noise. It is worth noting that t_5 was used as a point of reference to align all data analysed in this chapter. This is justified by the relatively large energy depositions of ninety degree scatters, for which t_5 corresponds to 19keV. The standard deviation of the noise has been measured as 10keV which only implies that ~5% of noise samples could be falsely identified as t_5. However, t_5 is not determined on an independent basis, but is found by moving backwards through the signal until the first candidate of t_5 is found.

An example of real charge variation through depth is shown in Fig. 4.7. The collimator was positioned central to the AC06 strip pitch and scanned from the DC electrode to the AC electrode. The ten depths closest to the AC side are shown in red, depths closer to the DC side are shown in blue. The effects of time alignment can clearly be seen by the appearance of a common coordinate. All signals have also been normalised and interpolated as described (section 4.3). Total rise times vary from 150ns – 350ns as expected. $T90_x$ partial

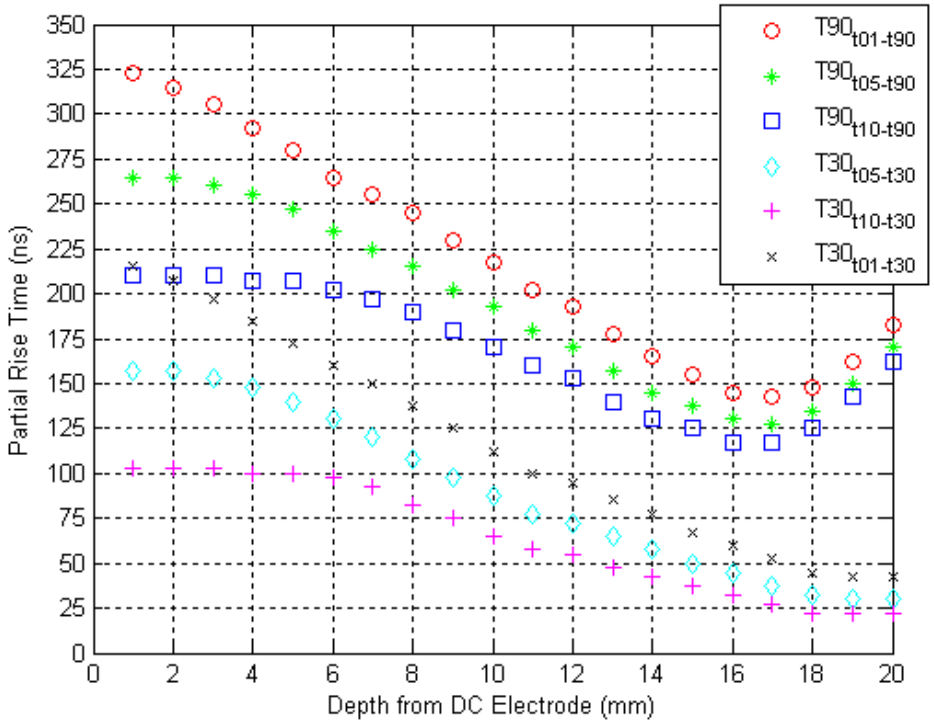

Figure 4.8: Partial *rise times* (section 4.1.3) determined from the real charges shown in Fig. 4.7. T90 for a range of time parameters is shown. T30 is shown for the same parameters.

rise times are characterised relative to three time parameters: t_1, t_5 and t_{10}. Fig. 4.8 shows how the resulting partial rise times vary through depth for the signals shown in Fig. 4.7. $T30_x$ partial rise times are also shown in this plot.

An immediate comparison with previous work [Tur06] shows that the minimum of $T90_{01}$, which is determined as (142±2)ns, is in good agreement to the previous value of ~(140±3)ns. However, rise time values at the crystal faces have been determined as 322ns and 182ns, ~10ns faster and ~10ns slower than previous work. The simplest explanation which would appear likely is that the crystal boundary has been taken at different collimator positions. The beam has a 1mm diameter, and it is possible to locate the crystal boundary at a discrete 1mm location, when in reality only a 0.5mm radius of the beam, or less is probing the crystal. This effect results in the observation of a substantially thicker crystal. The true crystal depth lies within a 20mm range in this apparently thicker crystal. Therefore, it is a simple assumption that two different 20mm ranges have been taken. This is supported by almost identical rise time values at identical 1mm increments away from the minimum rise time right up to the crystal boundary e.g. the fourth increment to the left of the minimum is (175±3)ns compared to ~(175±3)ns in previous work. This is further supported by an

apparent shift of the location of the fastest partial rise time; 17mm compared to 16mm. The disparity between the two results is explained by the crystal location in respect to the scanning table, and no other reasons will be sought.

Other partial *rise times* show the same trend. The similarities between these two different experiments would indicate that *rise times* are only a function of depth and not energy deposition because two different energies were used (374keV versus 662keV). More significantly, these two results prove that the previous work was not affected by Compton scattering as previously hypothesised. This remarkable result suggests that Compton scattering did not occur in previous work, or it was simply undetectable in the analysis. However, Compton scattering was the most probable interaction in previous work and the data would unavoidably be polluted with such events. According to the Klein-Nishina distribution the scattering angle was most probably forward. The beam was shone along the AC electrode in both experiments. For scattering not to have an impact on the analysis would suggest that forward scattering cannot be discriminated from a single photoelectric event providing that scattering is along a plane which is parallel to the electrode face.

This is a very important result which indicates that certain event types will be wrongly identified regardless of the complexity of the analysis that is used to identify them. Any analysis which can identify a signal trait when one does not exist is simply flawed. However, in relation to scattering events, this result permits a subdivision of Compton scattering into two distinct categories: those which scatter along a plane parallel to the electrode face and those which scatter in a direction normal to the electrode face. These shall be termed in-plane scatters and in-line scatters respectively.

A further, more tenuous conclusion can be drawn about the scattering distance. Considering that scattering angles are symmetric about the forward scattering angle (Fig. 2.3), it was originally thought that this symmetry would show an appreciable effect near crystal boundaries. A fraction of scatters could escape and an equal fraction could travel towards the centre of the crystal; photons which escaped would not affect the detector response. This effect is not seen which suggests that a 1mm collimator is not sufficiently sensitive to see this effect, and suggesting that scattered photons are absorbed a very short distance

from the scattering site. Indeed, simulations (appendix A) show that the majority of scatters deposit their energy with a radius smaller than 2mm.

Returning to the analysis of the results obtained as an individual experiment, it can be seen in Fig. 4.8 that the slowest and fastest partial *rise times* vary from 325ns - 180ns respectively. This is what is expected in relation to carrier drift velocities (section 2.4.2). The minimum *rise time* occurs away from the central depth because the carrier drift velocities are not equal. The experimentally-derived depth at which this occurs is 17mm, but this is based on knowledge of the crystal location which appears partly arbitrary. However, a good variation of partial *rise times* is evident in Fig. 4.8, which ultimately permits the use of pulse shape analysis to determine the depth of interaction.

The most unambiguous parameter is $T30_{01}$ which does not present one single *rise time* for two depths of interaction. Unfortunately, it would be experimentally impracticable to measure t_1 on a real signal and t_5 would be a more secure measurement. To avoid the ambiguities introduced by using partial *rise times* based on t_5, for which two depths can have the same *rise time*, it is necessary to compare one partial *rise time* against another. Both axes are now defined as time and each individual event can be cross-referenced against a database of *rise times*. The parameters plotted against each other are $T90_{05}$ and $T30_{05}$. The singles scan was used to produce this plot on an event-by-event basis (section 4.4.5) to see if the relationship held experimentally; results are shown in which the average partial rise time results are plotted alongside event-by-event partial rise time results derived from the singles scan using 662keV events.

4.4.4 Asymmetry Parameter

The transient induced charges fully describe the position of interaction for a single interaction. However, they are only a fraction of the real charge amplitude and are difficult to analyse in noisy signals. The average transient induced charges from the spectator electrodes that correspond to the average real charges shown in Fig. 4.7 can be seen in Fig. 4.9. Although these signals were subject to the same alignment as the real charges, they are not aligned with respect to each other before they are summed. As noted in section 4.3.3,

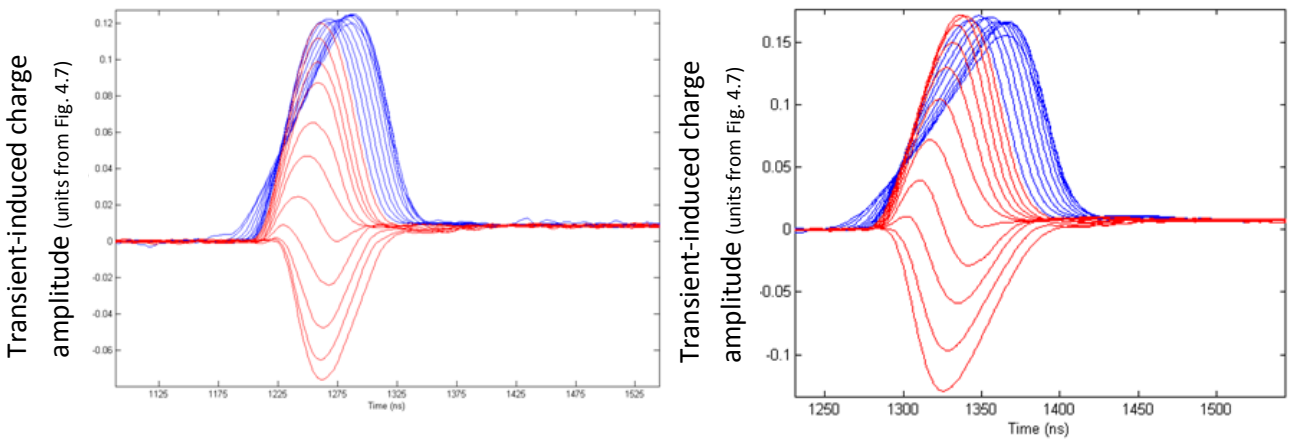

Figure 4.9: Transient induced charges as seen on the next nearest neighbour spectator electrodes in relation to the collecting electrode (AC06) as shown in Fig. 4.7. Red signals are for the interactions that are closest to the AC electrode, whilst blue represents interactions closer to the DC electrode. AC04 is the response shown in the left image. AC07 is the response shown in the right image.

this walk will be neglected. Red signals correspond to interactions closet to the AC electrode, whilst blue signals correspond to interactions closer to the DC electrode. The transient-induced charges can be seen to vary as a function of depth, but this sensitivity is only through the section of depth closest to the AC electrode; amplitudes are uniform close to the DC electrode. The bi-polar region occurs approximately 3mm from the AC electrode and covers no more than 2mm of depth. This was predicted by the weighting field concept (section 2.7). The depth of interaction will be determined by real charge analysis so that the only information that is required from the transient-induced charges is the lateral location of interaction. The lateral sensitivity of transient-induced charges is not shown in Fig. 4.9 for reasons of clarity. However, the lateral sensitivity is shown for two depths of interaction in Fig. 4.10.

Fig. 4.10 shows how the weighting field coupling between strips and spectator electrodes affects the response of the transient-induced charges. Interactions close to the spectator strip induce a large response, whilst interactions far from the spectator electrode induce a small response. The two constant depths, 5mm and 18mm as measured from the DC electrode, have been chosen to demonstrate the effects of interaction depth on polarity. It can be seen that the depth of interaction has an effect on the polarity, but the overall relative magnitude between the two strips is still related to lateral interaction location. It is this relative magnitude between the two next nearest-neighbour spectator electrodes that is utilised to extract lateral position information from the interaction (Equ. 2.38). The exact

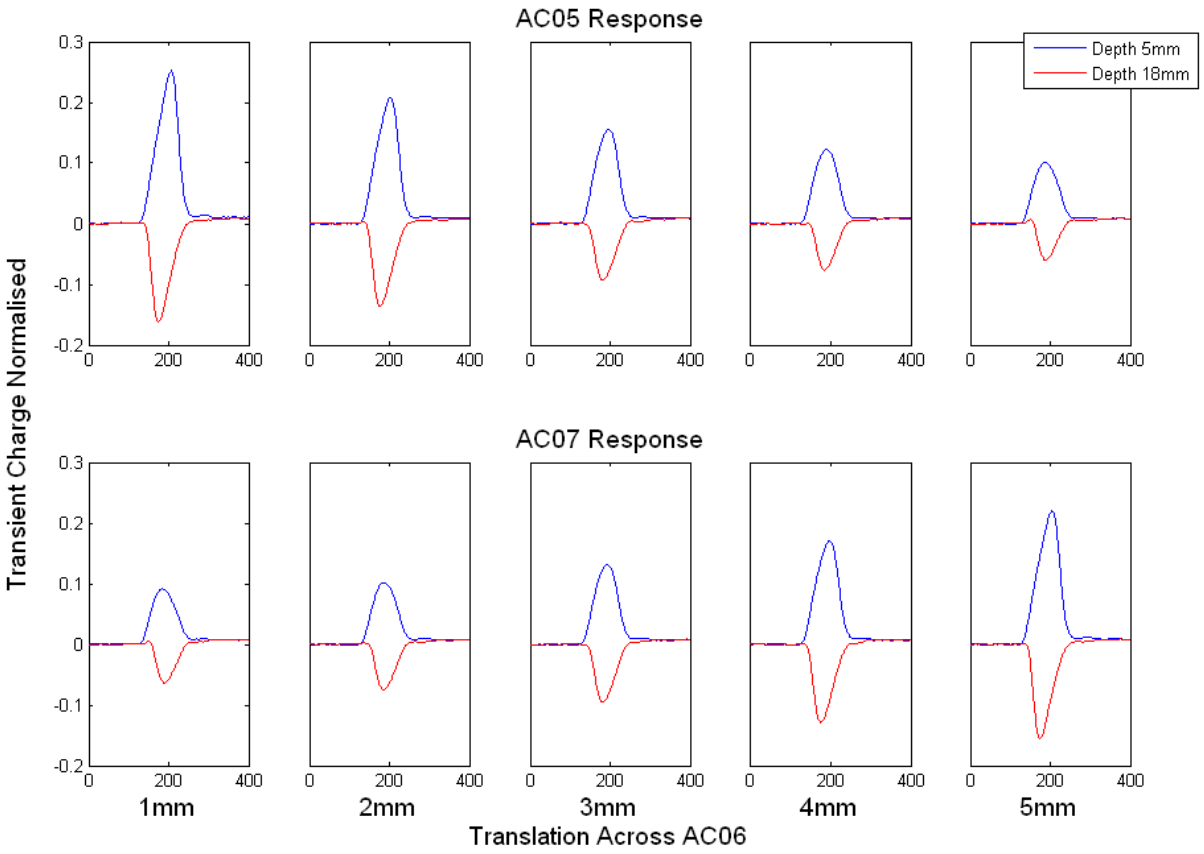

Figure 4.10: Transient-induced charge responses for AC05 and AC07. The collimator was shone across AC06, in 1mm lateral increments, at two constant depths, from the strip boundary with AC05 to strip boundary with AC07.

effect of interaction depth can be corrected for if the depth is calculated prior to the *asymmetry parameter*. However, if no correction is made, it should be assumed that the *asymmetry parameter* (Equ. 4.2) will give exceedingly small values in the bi-polar region and opposite polarity values for interactions close to the DC or AC electrodes. Fortunately, the lack of interaction depth sensitivity for interactions close to the DC electrode should allow a naïve application of the *asymmetry parameter* over this region, because the relative magnitudes will be independent of interaction depth.

Fig. 4.11 shows the *asymmetry parameter* calculated with equation 4.2 for interactions through all depths and all translations in strip AC06. The plot shows, as expected, that for the first 13mm away from the DC electrode the *asymmetry parameter* is fairly uniform at specific collimator lateral positions. However, for interactions towards the AC electrode, where the transient-induced charges invert, the *asymmetry parameter* has a poor sensitivity to lateral interaction location because there is no variation between different lateral positions. The 2mm' through depth, closest to the AC electrode, has good lateral sensitivity

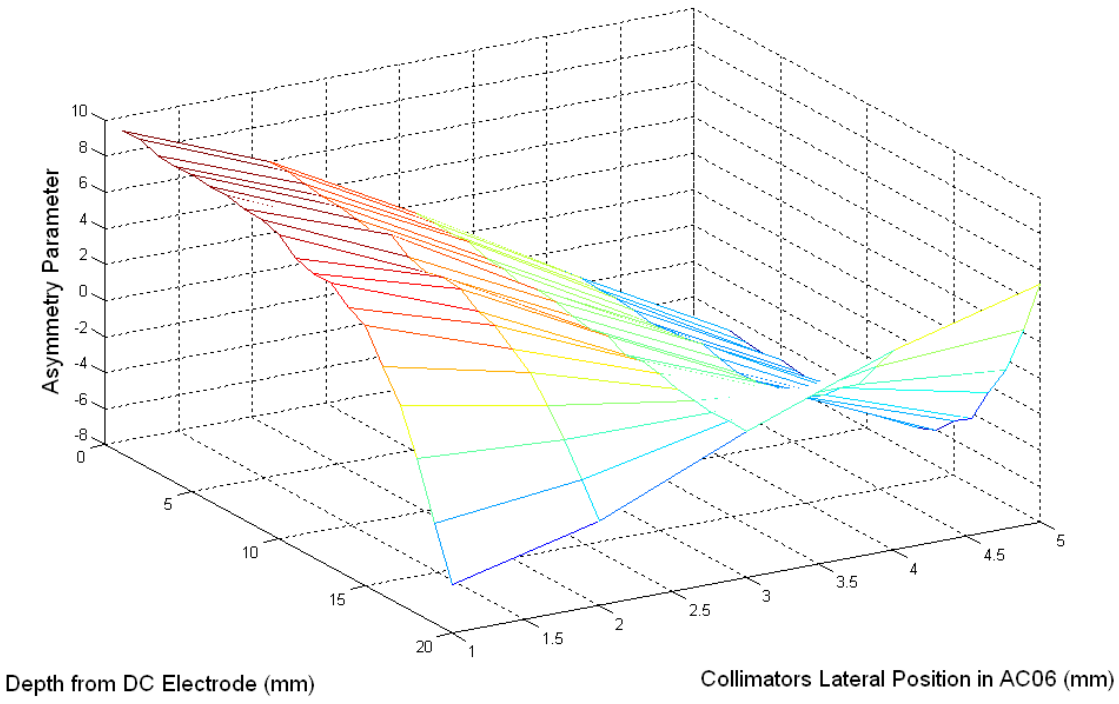

Figure 4.11: *Asymmetry parameter* calculated (Equ. 4.2) for each scanning table position through depth and translation in AC06 from the average response. The 1mm lateral position coordinate represents a primary collimator position near to the strip boundary of AC05. The *asymmetry parameter* follows the expected trend.

but opposite polarity to the previous interaction depths towards the DC electrode. It is clearly apparent that interactions in the bi-polar region suffer from low-amplitude transient-induced charges. The spatial resolution obtained for interactions in this region should be used with caution. It is advantageous to use a reasoned approach towards the *asymmetry parameter* which includes consideration of the depth of interaction to deliver reliable results. This makes determining the depth of interaction a priority. Indeed, the depth of interaction carries the biggest potential errors with a possible 20mm range; lateral position determination errors are inherently limited to 5mm.

Fig. 4.12 replicates Fig. 4.11 with average data from the singles scan. The *asymmetry parameter* was calculated for each individual interaction and summed to the total *asymmetry parameter* for that position. The final value was divided by the total number of interactions that passed the gates at that position. Normal fold-1 and full energy deposition gates were applied. The important feature of this figure is the close match with Fig. 4.11. Critically, this indicates that once the signals are normalised in the C code, all subsequent PSA is energy-independent. Although this was expected, it is a reassuring to confirm that the *asymmetry parameter* is energy-independent, just as *rise time* analysis is energy-

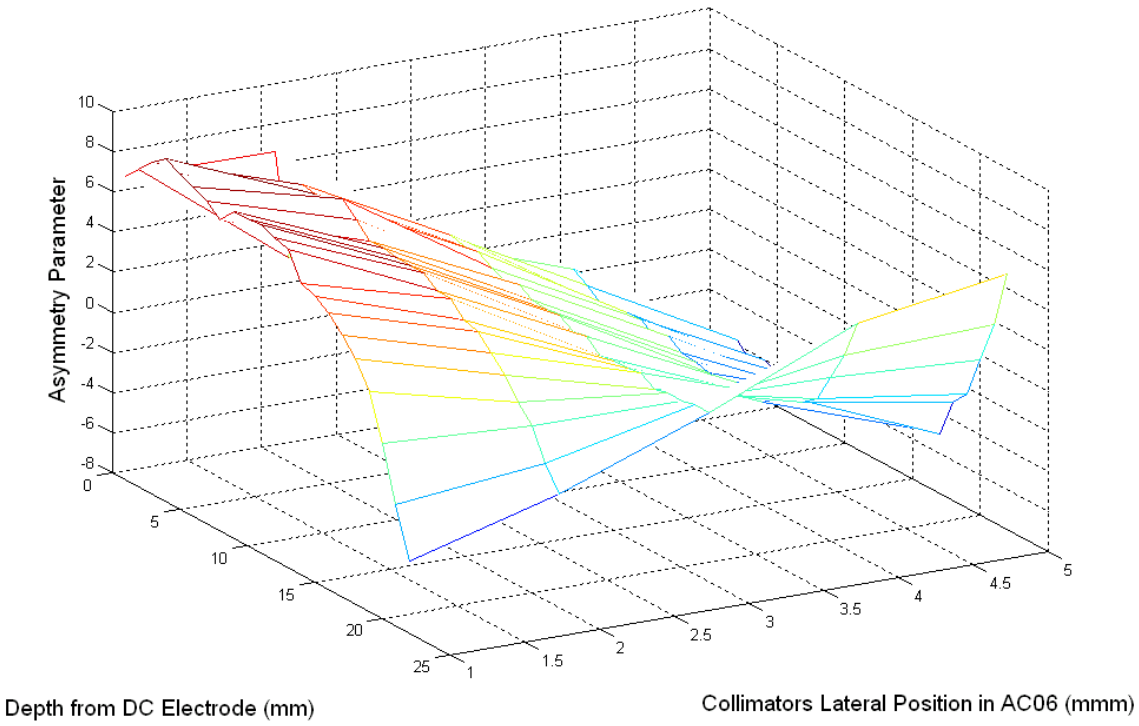

Figure 4.12: Reproduction of Fig. 4.11 using the singles scan (section 3.6.2). The similarity indicates that the asymmetry parameter is energy independent after real charge normalisation.

independent. PSA can now be applied on a true event-by-event basis as a test of sensitivity. This type of test is usually accompanied with quotes of position resolution performance, but the stated values are normally determined by average distributions of PSA parameters. This is misleading and the ultimate results are far more significant, as demonstrated by [Lee07].

4.4.5 Event-by-Event PSA

Rise time analysis of average real charge response has been performed in section 4.4.3. It was found that *rise times* are sensitive to interactions originating at different locations through depth. Fig. 4.13 presents the two parameters $(T90_{05}, T30_{05})$ chosen in section 4.4.3 to characterise the real charges. The first image is a plot of $T90_{05}$ against $T30_{05}$ derived from the average signals presented in Fig. 4.7. The second image contains values of $T90_{05}$ against the corresponding $T30_{05}$ values as determined from individual signals. The singles scan was used for the second image. All AC real charge responses for all fold-1, full energy deposition events have been analysed; a total of 286724 events. Therefore, all of the x-y scanning table positions described in section 4.4 have been used. The remarkably close

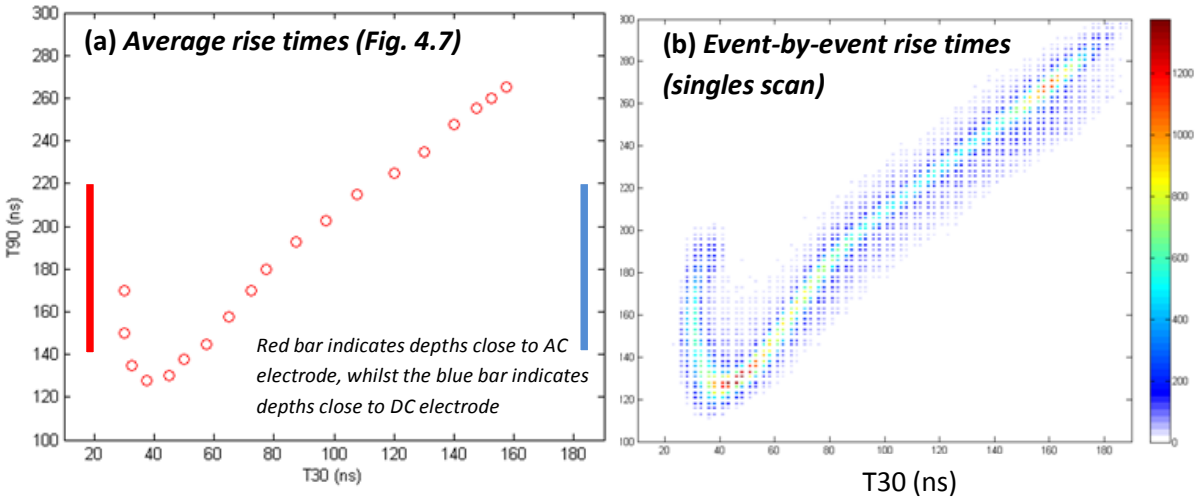

Figure 4.13: Partial *rise times* plotted against each other for average and event-by-event data. Image (a) was created using the average data presented in Fig. 4.7; blue bar represents blue in Fig. 4.7, red bar represents red in Fig. 4.7. Image (b) was created using event-by-event data from the singles scan. All x-y scanning table positions described in section 4.4 and seen in Fig. 4.4 were allowed to contribute datum in image (b).

match of these two plots supplements the argument that forward scatters, scattering in a direction parallel with the electrode plane, have no distinguishing features that can be used to identify them as a scattering event.

Another conclusion can be drawn from the close agreement. The deviation of individual responses from the average responses is small. Average responses from a single line through depth (x = 91mm) have been used in image(a) whilst individual responses from all depths (across all AC strips) have been used in image(b). Therefore, the deviation between real charges from edge strips or centre strips is small, indicating that real charges are only a function of depth. It would then be possible to describe the depth of interaction with just 20 simulated signals which disabuses the notion that electric field simulations should be simulated for all possible interaction locations.

Performing this analysis for a given experimental run should permit a calibration for depth by gating around particular regions. These regions can then be compared and identified in the look-up table of Fig. 4.13. Position sensitivity through depth is then clearly related to the number of partitions used. No more than 5 partitions would be recommended which limits the position resolution to no greater than 4mm in depth. A possible test of position resolution through depth would be to reconstruct the depth of the primary beam and compare this against the actual known depth of the primary beam [Lee07]. This has not

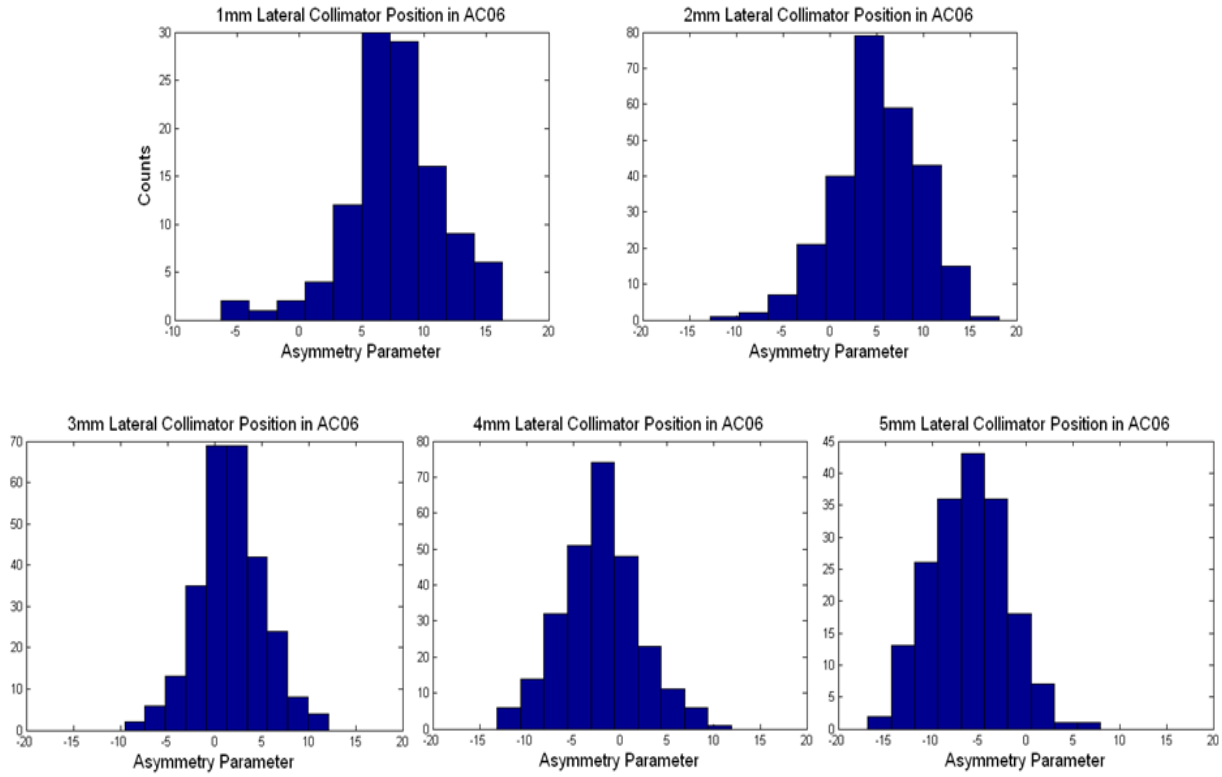

Figure 4.14: *Asymmetry parameter* calculated for a constant depth but variable translation across AC06. The 1mm lateral position starts close to the strip boundary between AC05 and AC06. The 5mm lateral position ends close to the strip boundary between AC06 and AC07. The mean values for the *asymmetry parameter* are the various translations are: 1mm = 7.52 (111 counts), 2mm = 5.13 (268 counts), 3mm = 1.73 (272 counts), 4mm = -2.13 (266 counts), and 5mm = -6.22 (183 counts).

been performed for rise time analysis but has indeed been performed for a superior method presented in section 4.6. Rise time analysis has simply been used to image radioisotopes.

The *asymmetry parameter* has also been calculated individually from the singles scan. Usual gates were applied and the beam depth was fixed at y = 58mm. The primary collimator location was then in the region for which the asymmetry parameter is uniform throughout 13mm of depth. Histograms of the *asymmetry parameter* for five lateral locations across AC06 are presented in Fig. 4.14. The 1mm data represent the strip boundary with AC05, whilst 5mm represents the strip boundary with AC07. Comparison of Fig. 4.14 with Fig. 4.11 shows that the general trend of the individually-calculated *asymmetry parameters* is close to that expected from the average responses. This implies that PSA can be exploited for lateral sensitivity to increase spatial resolution. This method is utilised for image reconstruction in chapter 6.

4.5 Collimated Coincidence Scan Results

The collimated coincidence scan analysis used the same gates and pre-processing as the uncollimated scan. Due to the dramatic drop in statistics, resulting from the use of secondary auxiliary-collimators, only a limited number of positions where scanned. Ultimately, SP1 should be scanned for a greater number of positions with secondary collimation, which would be far superior to the uncollimated scan, but due to time pressures this did not occur. The scanning table and electronics were required for a new AGATA capsule and less than 1 month in total was allocated for all measurements including testing the detectors and experiment set-up; if there were enough data then *rise time* analysis could be performed for a number of depths at fixed DC electrode translations, and *asymmetry parameters* could be determined for the DC electrode. The main purpose of the secondary collimated scan is then to validate the uncollimated scan results and the new technique presented in chapter 5. The biggest assumption made for *asymmetry parameter* analysis, which has not yet been acknowledged, is that the transient-induced charges vary as a function of translation along one axis only. Specifically, it is assumed that it is insignificant how far along AC06 an interaction occurred and only where in relation to the AC05 and AC07 strip boundaries this interaction occurred. Transient-induced charges can now be compared at various locations up-along the AC electrode.

4.5.1 Positions Scanned

The only AC strips exposed to the primary collimator were AC05 and AC06. The secondary collimators that were positioned between the PT6X2 and SP1 allowed 3 DC strips to be 'scanned'. These strips were DC01, DC04 and DC07. The secondary collimators positioned between the M6X6 and SP1 allowed 5 DC strips to be scanned. These were strips DC01, DC02, DC04, DC05 and DC08. More strips were 'scanned' by the M6X6 because more collimator slits rested on strip boundaries, so that a 1mm movement along the z axis then collimated a new DC strip. It was a necessity to scan the lower indexed DC strips because these had the higher number of interactions, and the allocated time was short. However, this edge region is where the uniformity of the electric field could be warped, if indeed it does warp in the active region. It would therefore have been advantageous to scan the

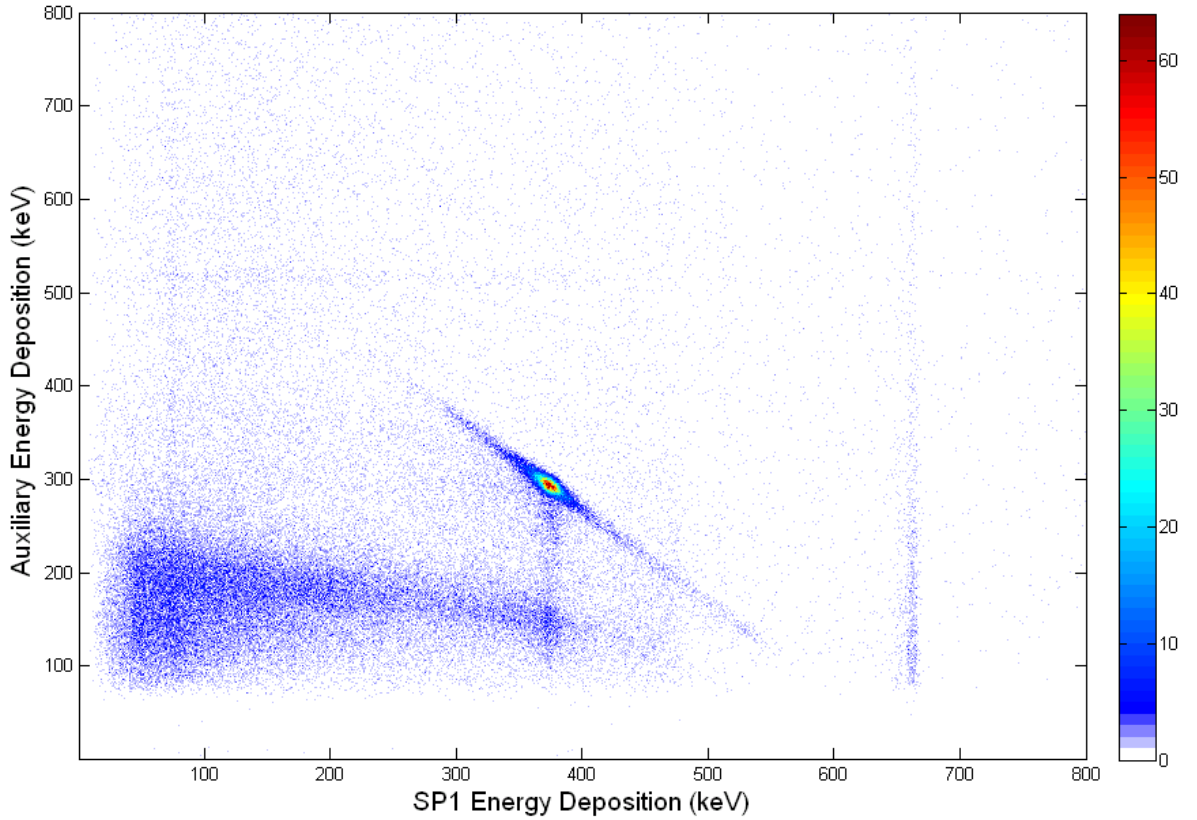

Figure 4.15: The energy matrix containing energy deposition in the auxiliary detectors indexed against the energy deposition in SP1. The data were collected with the secondary collimators. The maximum intensity is located at the coordinates (375,293). The 662keV diagonal line has a large number of counts in the immediate vicinity of 375keV, corresponding to scattered photons which have passed through the secondary collimation. The limited range of scattered energies can be contrasted with Fig. 4.5. Other notable energy 'lines' are a vertical 662keV line which arises from random coincidence, and a 375keV vertical line which corresponds to incomplete energy-collection in the auxiliary detectors.

central region. A total number of 4 runs were performed during this experiment, with the secondary collimators moved for each run. The primary collimator scanning positions also varied between each run. However, the time that the primary collimator was static at each x-y position did not change between runs; this was 7200 seconds per position. The most comprehensive run was the first (RUN1), which scanned AC05 completely through depth and half of AC06 through depth. All other runs focused on AC05 exclusively.

An energy matrix containing all of the events collected over all positions with secondary collimation is shown in Fig. 4.15. A total number of 18662 events passed the usual energy and fold 1 event selection criteria. These are spread over 1668 x-y-z interaction locations resulting in an average of 11 events per position, or a count rate of just 1.5×10^{-3} useable events per second. Such a low number of counts clearly restricts any interpretation and comparison with the uncollimated scan. However, the number of counts per position, close

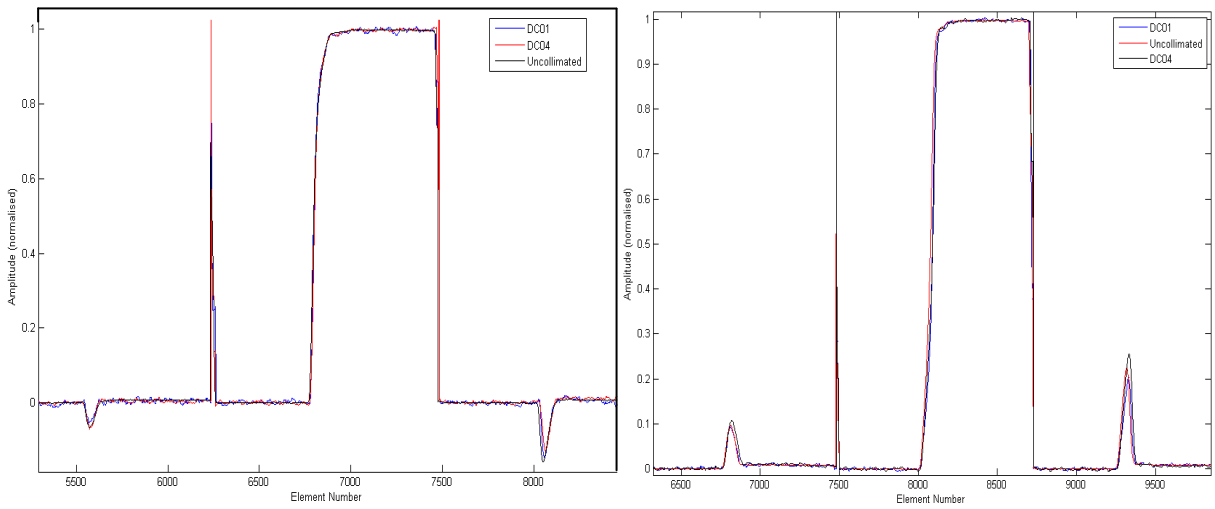

Figure 4.16: Example comparisons between the average responses from the uncollimated and collimated scans. Image(a) shows the response from position X88Y72 (AC05) including the spectator responses; DC01 and DC04 are two of the secondary collimator positions. Image(b) displays the response from position X93Y62 (AC06) including the spectator responses. It is apparent by inspection that the responses agree, which would indicate that AC response is indeed only a function of x-y scanning table position.

to the crystal edges, will be significantly greater than 11 and it is possible to draw conclusions regarding both scans and to reconstruct Compton-scattered events. The reconstruction is important to test the digital Compton suppression technique presented in the next chapter.

4.5.2 Analysis

The first run (RUN1) was the most comprehensive in terms of positions scanned (191 x-y positions) and events recorded. A total of 14203 events were recorded during RUN1 compared with 3484 during RUN2, 934 during RUN3 and 31 during RUN4. The average number of counts per position for RUN1 is 38. RUN1 is the only run to have significant counts, and the analysis in this section shall be restricted to RUN1 accordingly. However, the results gained from the coincidence scan have proved extremely fruitful and the experiment is being considered with a greater allocation of time in future. Restricting analysis to RUN1 also restricts the DC strips which triggered to DC01, DC02 and DC04. Examples of the signals which have been extracted from identical x-y positions are shown in Fig. 4.16. Two x-y positions have been compared, these are at the scanning table coordinates (88,72) and (93,62), which were predicted to give opposite polarity transient induced charges. The response of DC01 and DC04 have been chosen because they lie the furthest apart and are

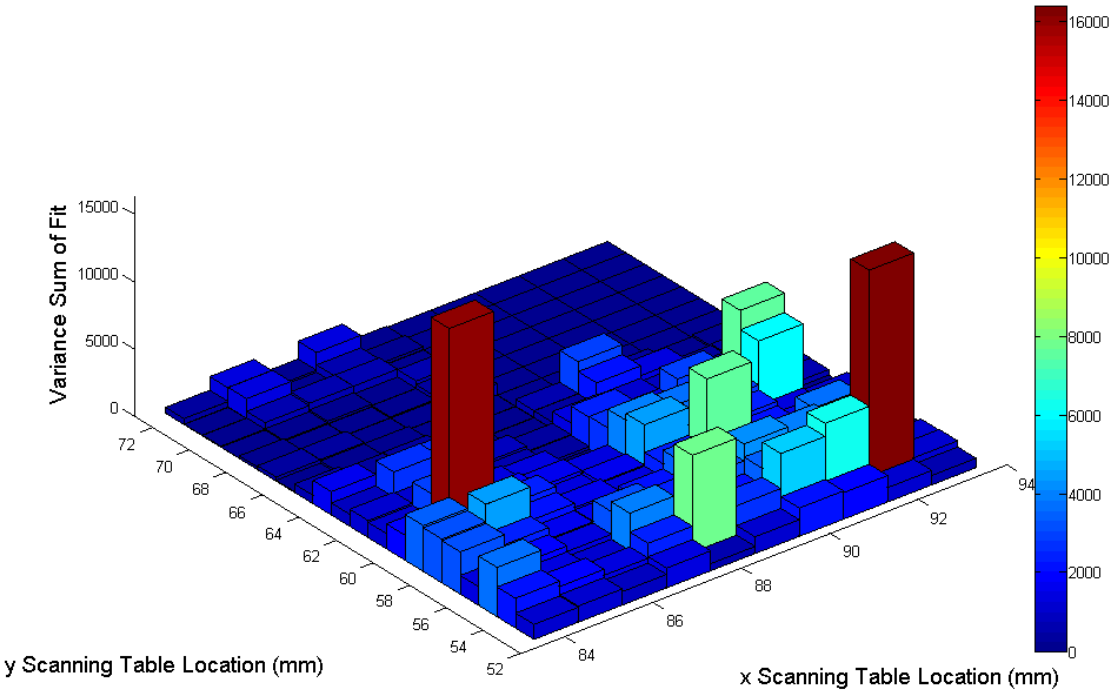

Figure 4.17: Results from fitting uncollimated data with secondary-collimated data from DC01. The sum of squares at each collimator location is shown on the grid. Large values correspond to a bad match at that x and y location. Small values correspond to a good match.

therefore a good test of the hypothesis that transient induced charges on the AC side are only a function of depth and translation across the AC face. A good match between all signals can be seen. The sum of squares can be used to quantify the match between the uncollimated scan and the secondary-collimated scan. This has been performed for all positions in RUN1 which are located in DC01, and DC04. There are too few counts to compare the secondary-collimated scan in other DC strips with the uncollimated scan.

Figure 4.17 shows the sum of squares resulting from a match between the uncollimated scan and the secondary collimated scan. The secondary collimated data used in this figure were collected using the PT6X2 and triggering on DC01. The collimator slit width between the PT6X2 and DC01 was 1.2mm. This slit covered the very first 1.2mm of DC01 in relation to the primary beam, see Fig. 3.5 for clarity. The sum of squares was calculated over 5000 signal elements, resulting in large values compared with a sum of squares for a smaller data set. The average signal, at a particular x-y location, from the uncollimated scan was fitted against the average corresponding signal from the secondary-collimated scan. The smallest value corresponds to the best fit and the largest value corresponds to the worst fit. The best fit and worst fit as determined by the sum of squares method can be seen in Fig. 4.18. The

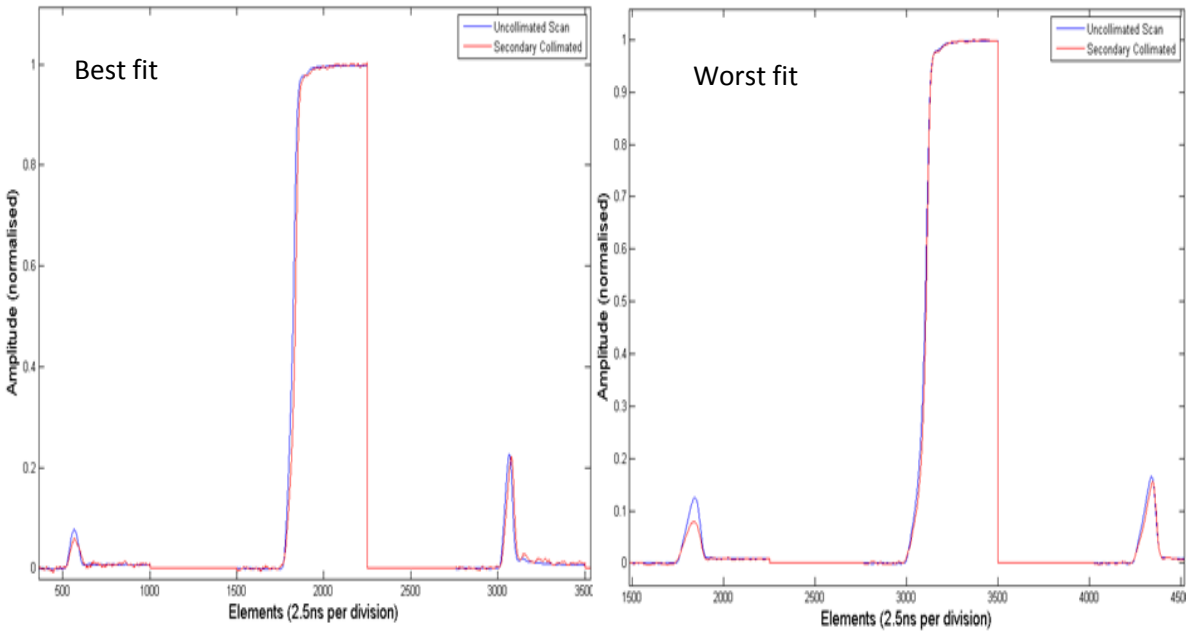

Figure 4.18: Uncollimated and secondary collimated average signals from two positions. The first image shows the signals from x = 88, y = 64. This corresponds to the best match. The second image shows the signals from x = 92, y = 54. This is the worst match.

worst fit was found at the primary collimator location x = 92mm, y = 54mm and a good fit was found at x = 88mm, y = 64mm. However, it can be seen by inspection that both signals actually appear to be an approximately good match. The worst match arises from the rather large transient-induced charge in the uncollimated scan result. Although the real charge and the other transient-induced charge both appear to be a good match. Overall the general trend appears show that both scans are well matched.

The equivalent sum of squares matrix for DC04 is shown in Fig. 4.19. A slit width of 1.2mm was created by the secondary collimators and ran along the centre of DC04. It is immediately apparent that the secondary-collimated scan for DC04 is in general better agreement with the uncollimated scan than that of DC01. There is only one salient bad match in Fig. 4.19 compared with a number of positions showing a bad match in Fig. 4.17. The primary beam position for this match is x = 87mm, y = 65mm. This position has been investigated and it was found that an unusual pulse appeared to precede the real charge. Indeed, the real charge itself carried an unusual form. It is suspected that a single anomalous event was recorded and summed to create the mean response. Neglecting this single position it can be assumed that the response of the uncollimated scan is close to that

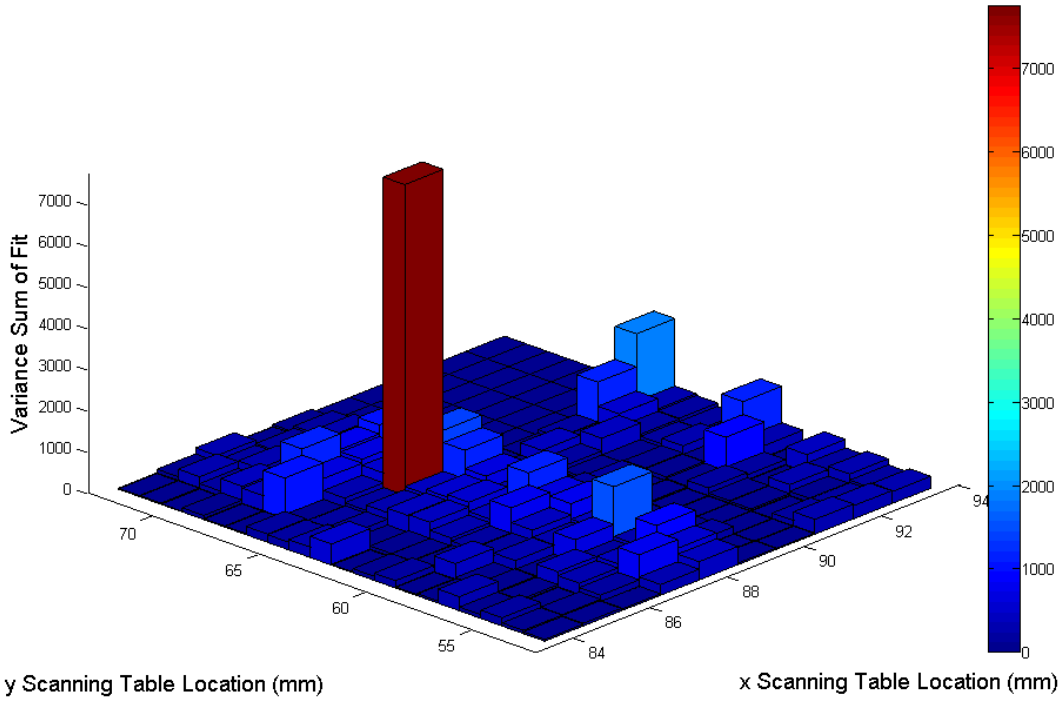

Figure 4.19: Results from fitting uncollimated data with secondary collimated data from DC04. The worst match is when the primary collimator is at x = 87mm, y = 65mm.

of the collimated scan indicating the warping of the electric field near the crystal edge is not highly significant for simple parametric PSA. Alternatively, advanced PSA can be developed.

4.6 Basis-Data-Set

In consideration of the previous sections, it can be assumed that the response of the AC electrode is sufficiently well defined along two axes to characterise the detector. One of these axes represents depth of interaction, and the average experimental pulse shapes from the uncollimated scan can now be used to build an experimental basis-data-set. This is a library of detector responses to single site interactions at well defined x-y locations. Events of an unknown interaction location can then be compared against this library and the most likely position of interaction determined. The principles behind this method have been suggested and tested for the GRETA and AGATA projects. It has been shown for simulated detector responses that this method provides an increase in spatial resolution over simple parametric PSA. Indeed, the real potential of this method is realised in respect to more complicated interactions. In theory, complex signal compositions can be reconstructed and

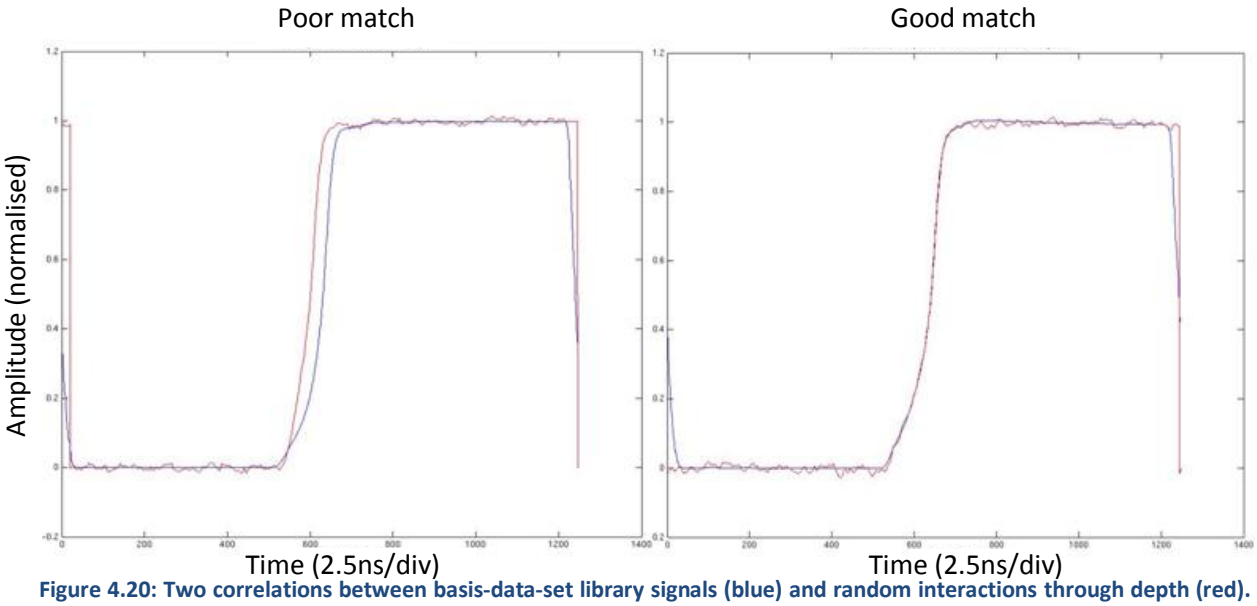

Figure 4.20: Two correlations between basis-data-set library signals (blue) and random interactions through depth (red). Image(a) shows a poor match, as determined by the correlation coefficient. Image(b) shows a good match, as determined by the correlation coefficient. The basis-data-set library signals are from a known depth in SP1, and therefore this method can be used to assign a depth of interaction to any random signal.

then compared against actual real complex interaction responses so that the signal can be decomposed and the multiple interaction locations defined. However, an entire library of detector responses for all interaction eventualities is beyond the time constraints of this research work and requires a full collimated-coincidence-scan.

4.6.1 Partial Basis-Data-Set

The mean response of the detector to radiation interactions at a particular location is known within two dimensions; x and y which represent crystal translation across the AC electrode and depth respectively. However, the immediate use of the partial experimental basis data set is to compare the library of average responses to individual interactions from unknown locations using only the real charge. This restricts the results to one dimension but provides a good test of the method. A correlation coefficient determines the most likely position of interaction through depth. The singles scan (section 3.6.2) has been used for the test and is therefore a different energy than that used to build the library. However, the real charges are normalised and assuming that rise times are independent of energy and only dependent on interaction location then comparing these signals serves as a good test of the usefulness of the partial basis data set across a range of energies.

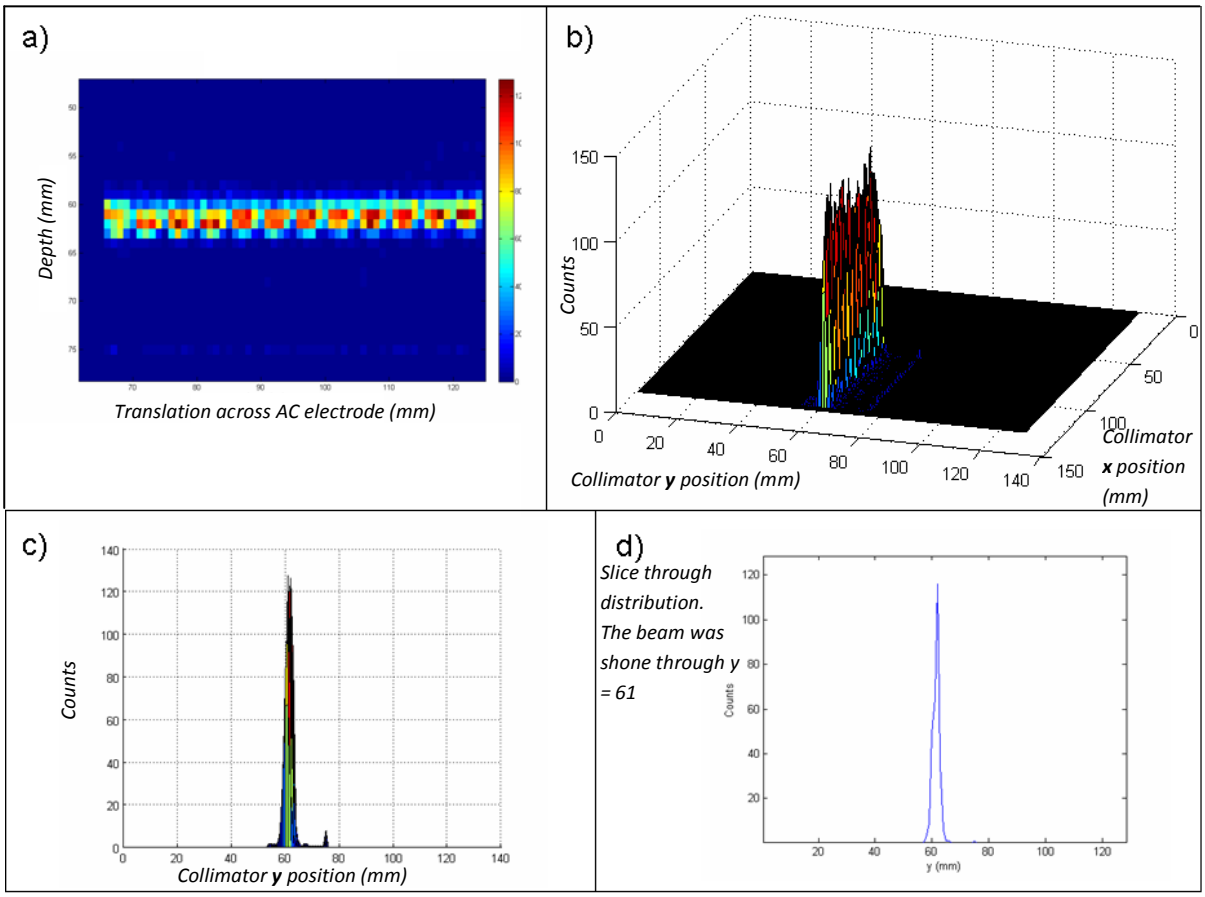

Figure 4.21: Image (a) displays a histogram which bins the interaction depth, of random signals, as determined by the goodness of fit on the depth axis. The translation axis is binned according to the primary collimator translation. The actual crystal depth that the primary collimator was scanned through corresponded to the scanning table position y = 61mm. Image (b) is a 3D representation of image a). Image c) is a side view of image b). Image d) is a slice through the distribution so that the FWHM can be calculated.

The actual test was conducted in such a manner that the primary collimator position was effectively held at a constant depth (y) in software and scanned directly through the crystal long axis (x); see Fig 4.4 for clarity. The program then takes individual interactions that meet fold-1 and full-energy gates and compares the AC electrode response to every possible response in the partial basis data set. A chi-square test for goodness of fit is performed and the fit with the lowest chi-square is then deemed the most probable interaction depth. Random examples of a good match and a bad match for a static collimator position are shown in Fig. 4.20. This method is a good blind test because the chi-square function does not access information relating to the collimator position; all interaction depths are possible results. Fig 4.21 shows good agreement between the actual primary collimator depth and determined depth.

For the data in Fig. 4.21 the primary collimator was fixed at y = 61mm, corresponding to a central depth. Each event which passed the enforced selection criteria was then analysed, and the depth of interaction as the primary collimated moved along the x axis was determined by the correlation coefficient. Image (a) shows a histogram of the determined collimator 'depth'; and a remarkable straight line running through the central depth of the detector has been reconstructed. Image (b) is a 3D representation of the image (a) which clearly shows the number of counts at each depth. Image (c) is a side view of image (b) allowing an inspection of the position resolution. Image (d) is a single slice through image (c). A brief analysis of image (c) is possible in MATLAB, involving an estimate of the FWHM and the FW.1H (full width at tenth maximum). This process has been repeated for all other collimator positions, in 1mm increments, along the y axis (crystal depth) that are deemed to be in the crystal, the results of which are presented in Tab. 4.1. It is worth noting that depth is the most important measurement to make correctly because large errors (upto 20mm) can propagate into an image, it is also the least accurate measurement because it is based on only single sample points that are taken from signal leading edge.

Table 4.1: Position resolutions as determined by the partial experimental *basis-data-set* through depth, for all depths. The FWHM and FW.1H have been determined by inspection in MATLAB.

Collimator Depth (mm)	FWHM (mm)	FW.1H (mm)	Collimator Depth (mm)	FWHM (mm)	FW.1H (mm)
52	2.3	5.3	**62**	1.6	4.8
53	1.8	4.9	**63**	1.7	5.6
54	1.9	5.8	**64**	2.4	4.7
55	1.5	5.1	**65**	2.2	4.9
56	1.3	6.18	**66**	2.0	5.5
57	2.3	5.9	**67**	1.8	5.2
58	1.6	5.2	**68**	1.9	5.0
59	2.0	5.5	**69**	1.6	5.9
60	1.7	6.1	**70**	2.0	5.2
61	1.8	6.0	**71**	2.5	5.7

The FW.1H has been included for completeness and also because some distributions tend to be rather broad about the base. This does not account for the double peaking in Fig. 4.21, which represents depths outside of the crystal. However, Tab. 4.1 does in general represent good position resolution of the primary beam through depth (1.9mm avg. FWHM). This would require 10 divisions to be established in Fig. 4.13 which is unfeasible. Therefore, Tab. 4.1 also represents a progression of the attainable spatial resolution of interactions in SP1. This method is also relatively simple to implement and can be optimised in future work.

4.7 Event Reconstructions

The partial experimental basis-data-set can be utilised to reconstruct multiple events to demonstrate how complex events can be decomposed, or indeed simply identified in the subsequent chapter. Event reconstructions also demonstrate that not all multiple interactions need to be considered as a complex composition of two interactions, but can indeed be considered as two single interactions so that simple PSA can be used to extract position information from a multiple interaction. Fig. 4.6 shows a typical response from coincident interactions for a static x-y primary beam position. All strips, including the guard ring are shown along with the auxiliary detectors. By simply summing another interaction it is assumed that this summation replicates the superposition of multiple interactions in the detector, and the summed detector response is then representative of a true scatter from the first site to the second site. This has been done for a number of combinations, one of which is shown in Fig. 4.22. This reconstruction involves two interactions which are 7 strips apart. The red signal represents the reconstruction and shows virtually no apparent effects from one interaction on the other. This would indicate that simple PSA can be used to analyse the response of the collecting and spectator electrodes without special considerations if the collecting electrodes are 7 strips apart. This should not be surprising given the small weighting field coupling over large distances (Fig. 2.10). However, the two interactions need to be sequenced and it would be sufficient to assume that the shallowest interaction occurred first for a particular energy; see the Klein-Nishina distribution Fig. 2.3.

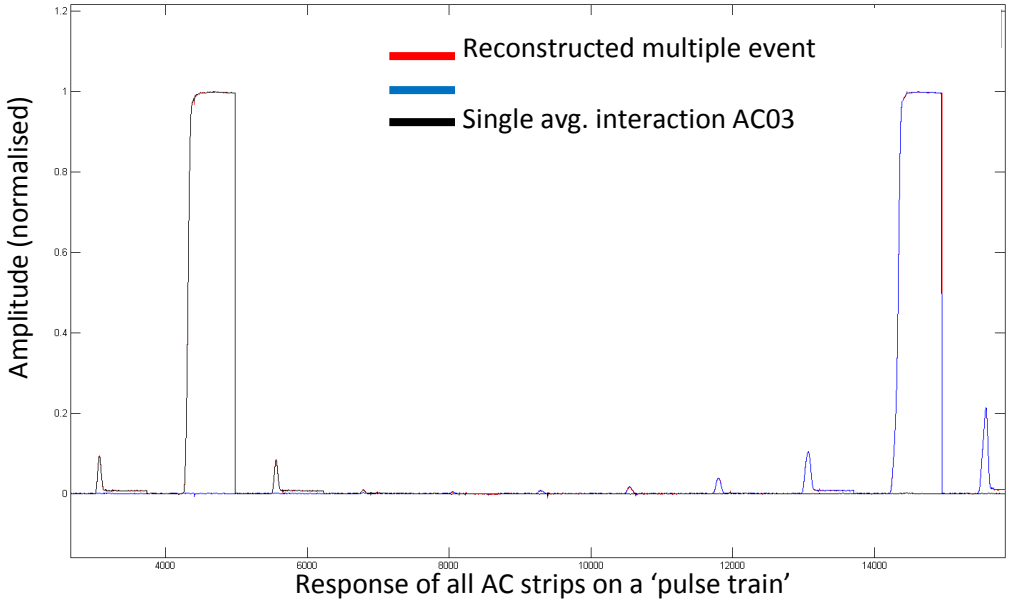

Figure 4.22: The library created from the uncollimated scan has been used to reconstruct the AC electrode response of SP1 to a multiple interaction. Central positions in AC03 and AC10 have been selected as the locations of two interactions. The multiple interaction response is shown by the red line; this cannot be seen and is masked by the individual interactions. Therefore, it can be assumed that these interactions are too far apart in terms of the weighting field to affect the respective responses of the single electrode strips, when the triggering strips are AC03 and AC04.

Reconstructing events which are closer together highlights the problem of multiple interactions. Reconstructing two interactions in a single closed-face-pixel is postponed until the next chapter. However, a common fold-2 event has been reconstructed in Fig. 4.23. These interactions are the average response of AC08 and AC09. They have been selected to represent charge sharing so that the average response from these two strips varies by 1mm on the AC08/09 strip boundary only, the depth was fixed. The similarity of the leading edges and the transient-induced charges can be seen. The effect of the transient-induced charges from the opposing interactions is also seen by inspection to be almost identical. This permits the introduction of another classification of event; if the real charges for a fold-2 event closely match then the event is a possible charge sharing event. Unfortunately, this event could also represent a Compton scatter. However, a single position on the strip boundary at that particular depth can be assumed, because the Compton scattering distance is assumed small (appendix A).

The principles of a full data base for scattering can now be defined. The advanced algorithm should match the most likely combination for the measured response based on a priori information from simulated single interactions. The possible number of combinations for

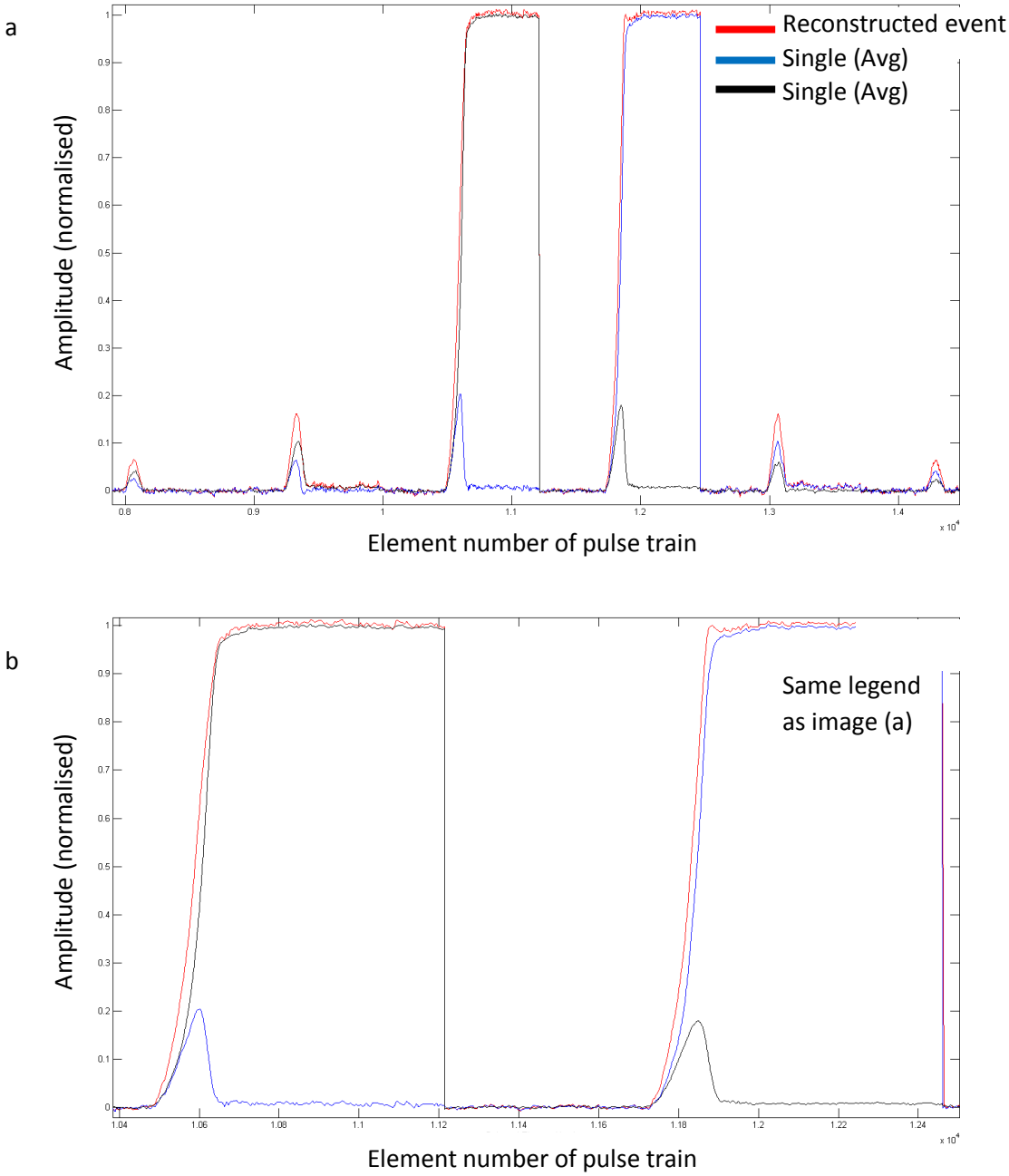

Figure 4.23: A reconstruction for two interactions close together. This event constitutes a charge sharing event or a Compton scatter. This multiple event is in contrast to that of Fig. 4.22 because both interactions adversely effect each other. Image (b) is an enlarged view of image (a).

this scenario if only the AC side is analysed is 10,000, derived from 100 possible sites in the first strip and 100 possible sites in the second strip. This neglects energy considerations and each combination has 4 strips that need comparing, requiring a large amount of computing power. However, the gain in sensitivity justifies the expense in computation.

Chapter 5

Digital Signal Processing

The suitability of using wavelet analysis to strip noise from detector signals has been investigated [Scr07]. The motivation behind this work was to ascertain if a signal's rise time could be characterised more accurately than if it was left in its original form. This work was commissioned before SP1 had actually arrived and earlier PSA had proved difficult on another planar germanium detector (GREAT) [Dob05]. Wavelet analysis has now been used with various degrees of success to represent noiseless signals. However, as the project evolved it was clear that wavelet analysis was not absolutely necessary, partly due to the large time requirement of processing, but also because of the excellent performance of SP1 relative to the GREAT planar. Although wavelet analysis has been shown not to be absolutely necessary in the common application of PSA, it quickly became apparent that it was in fact a naturally suited technique for picking out signal discontinuities. This is exactly what would be expected from a Compton scatter within a single pixel in which two or more majority charge carriers are collected (section 4.1.2). This new technique has indeed proven capable of identifying certain scattering events. As this novel technique allows the rejection of Compton scattering it will be referred to as Digital Compton Suppression (DiCS).

5.1 Time Domain

SP1 signals relate to the measurement of a current at fixed time intervals. This mathematical function of time is said to contain information in the time domain, and the state of the signal at any given time or over a specified time range is used to describe the

interaction; energy is given by the signal amplitude and geometrical interaction location is described by signal properties over a specified time range. A time domain representation is ideal if the signals are noiseless, whilst a noise component adversely affects signal characteristics. Although noise is not a significant issue for the PSA methods described in the previous chapter, when dealing with 662keV event-by-event interactions (section 4.4.5), it will inevitably be an issue for lower-energy interactions for which it will be difficult to gauge the amplitude of real charges. A common digital signal processing technique used to combat noise, which has proved successful, is to transform the signal into the frequency domain in which individual frequencies are now distinguishable. This technique can be used to extract relevant signal features and circumvent the analysis of superimposed noise. The power of this approach is easily demonstrated by concentrating on a conversation in a noisy room, frequencies of interest are singled out and analysed whilst the background frequencies are ignored by the brain.

5.2 Transformations

A transformation maps functions onto other functions, such that a transform decomposes a function in the time domain, into its frequency components in the frequency domain. A signal in the frequency domain is composed of base coefficients. An inverse transform, if one exists and under certain conditions, synthesizes a function from the frequency domain components and reproduces the original signal in the time domain. Transformations are the initial mathematical operation in any signal processing task. A common transform is the Fourier transform. Fourier showed that any periodic function may be expressed as an infinite sum of periodic complex exponential functions, provided that the function has finite energy.

$$\hat{f}(\omega) = \int_{-\infty}^{+\infty} f(t) e^{-i\omega t}\, dt \tag{5.1}$$

The Fourier coefficient $\hat{f}(\omega)$ is obtained by correlating a function $f(t)$ with a sinusoidal wave $e^{-i\omega t}$ over all times, where $\omega = 2\pi f$. The transform supports all times and therefore every spectral component is simply assumed to exist at all times in the signal, which is only

true for stationary signals. Gabor solved this dilemma by proposing windowed Fourier transforms in which the signals are decomposed over elementary atomic waveforms, g, translated through the signal at given frequencies [Mal99].

$$g_{u,\xi}(t) = g(t-u)e^{-i\xi t} \tag{5.2}$$

The energy of the Gabor atom is localised near its time and frequency translations u and ξ respectively. This atom forms a rectangle centred at the coordinate (u, ξ), with a time width, σ_t, given by the standard deviation of the atomic waveform in the time domain, and a frequency width of σ_ω, given by the standard deviation of the atomic waveform in the frequency domain. By effectively segmenting the signal, frequency information is known in parallel with time information. However, the uncertainty principle dictates that spectral components cannot be known at precise instances of time. A wide window (wideband transform) gives good frequency resolution but poor time resolution. Conversely a narrow window (narrowband transform) gives good time resolution but poor frequency resolution. The resolution is fixed for any given transformation as a consequence of a fixed window width; more commonly known as a fixed support. Multiple resolutions are required for non-stationary transient signals with short burst of high frequency. SP1 signals are one such example of these types of signals and wavelet analysis can be used to satisfy the multiple resolution condition. Wavelet analysis has been investigated for use on HPGe signals for exactly this reason [Mih00], with special attention placed on pattern recognition.

5.3 Wavelet Transform

A wavelet is simply an oscillatory function with a zero mean, allowing the synthesis of lines with no net area, and finite energy. Like a windowed Fourier transform, a wavelet can measure the time-frequency variations of the spectral components a signal. However, the crucial difference is that wavelet analysis has various time-frequency resolutions; resolution is not uniform across the spectral range. Multiresolution analysis is usually designed to give good time resolution coupled to poor frequency resolution at high frequencies, and good frequency resolution coupled to poor time resolution at low frequencies. This treatment is

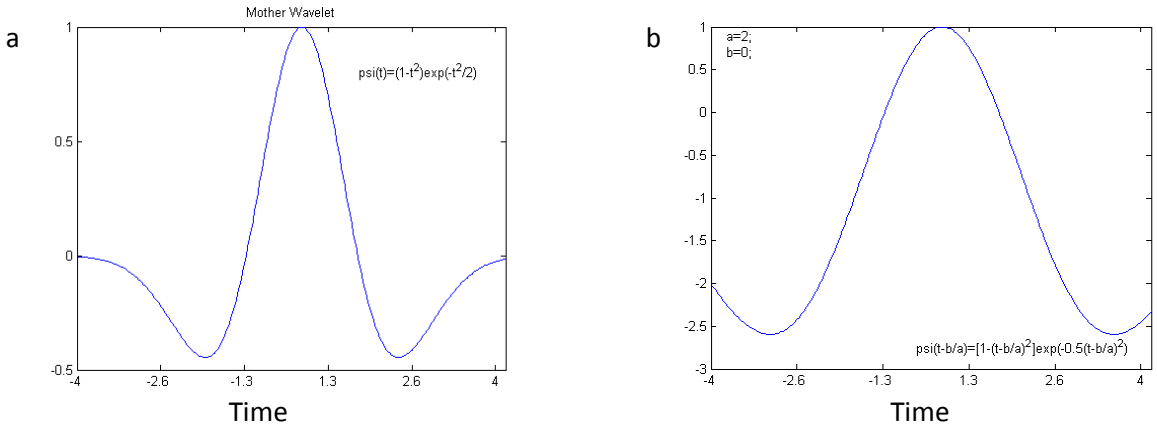

Figure 5.1: Image (a) shows the mother wavelet for the Mexican hat wavelet family. Image (b) shows a dilated version of the mother wavelet. Both functions can be used in a transformation to convert a signal from the time domain into the frequency domain. Image (a) gives good temporal resolution, whilst image (b) gives good frequency resolution. The displayed units of time are arbitrary.

ideal for non-stationary transient signals. The term *transient signal* does not refer to *transient-induced* signals as defined in section 2.5.2. Two example wavelet functions are shown in Fig. 5.1.

Mathematical implementations of a wavelet transform proceed in a similar fashion to a short-time Fourier transformation. The frequency integral is computed over discrete signal segments (windows) of the time domain signal. However, unlike the short-time Fourier transform, the width of the wavelet is scaled. A wavelet is a function $\psi \in \boldsymbol{L}^2(\mathbb{R})$ satisfying the zero mean criteria:

$$\int_{-\infty}^{+\infty} \psi(t)dt = 0 \tag{5.3}$$

The wavelet $\psi(t)$ is centred in the neighbourhood of $t = 0$ and is normalised such that $\|\psi(t)\| = 1$. The original function acts as a prototype for a family of scaled and shifted functions and is appropriately termed the *mother* wavelet. Translation and scale are controlled by the following equation:

$$\psi_{\tau,s}(t) = \frac{1}{\sqrt{s}}\psi\left(\frac{t-\tau}{s}\right) \tag{5.4}$$

where τ is the translation parameter and s is the scale parameter, whilst the $1/\sqrt{s}$ term is included for energy normalisation. There are a large number of mother wavelets available;

the derivatives of a Gaussian function form one such collection of wavelet families. The 'Mexican hat' is the second derivative of a Gaussian function and was originally designed to detect signal discontinuities. 'Mexican hat' functions are given below for the mother (Equ. 5.5) and a scaled or translated version (Equ. 5.6). These functions are also shown in Fig. 5.1.

$$\psi(t) = (1 - t^2)e^{-t^2/2} \tag{5.5}$$

$$\psi\left(\frac{t-\tau}{s}\right) = \left[1 - \left(\frac{t-\tau}{s}\right)^2\right] e^{-\frac{1}{2}[(t-\tau)/a]^2} \tag{5.6}$$

The transformation is a convolution between the original mathematical function of interest and a scaled wavelet translated throughout the original signal, such that a complete wavelet transformation is given by:

$$Wf(\tau, s) = \langle f, \psi_{\tau,s} \rangle = \int_{-\infty}^{+\infty} f(t) \frac{1}{\sqrt{s}} \psi^* \left(\frac{t-\tau}{s}\right) dt \tag{5.7}$$

where $Wf(\tau, s)$ is the coefficient resulting from the transformation, and $f(t)$ is the original signal. The transformed signal is now a function of two variables, translation τ and scale s. The translation parameter corresponds to time information, whilst frequency information is retained in the transform domain through a direct inverse relationship between scale and frequency. Frequency is simply the inverse of scale, such that a small scale gives a compactly supported wavelet and thus relates to high frequency. The wavelet transform is a two-dimensional representation of a one-dimensional signal and can be symbolically represented by rectangles tiled together with constantly varying height and width. This tiling scheme indicates the existence of redundancy based on parameter sampling in which the triangles overlap. The transform coefficient at a particular scale and translation measures the variation of $f(t)$ in the neighbourhood of τ whose size is proportional to s, such that large variations on consecutive transforms would indicate irregularity of $f(t)$ in the neighbourhood of τ. This irregularity identification is commonly used for edge identification in image processing and is exploited later in this chapter to identify signal discontinuities. The Mexican hat is a real wavelet and is the wavelet of choice to identify sharp signal transitions. In contrast, complex analytic wavelets can separate amplitude and phase information making them useful for measuring the time evolution of frequency transients.

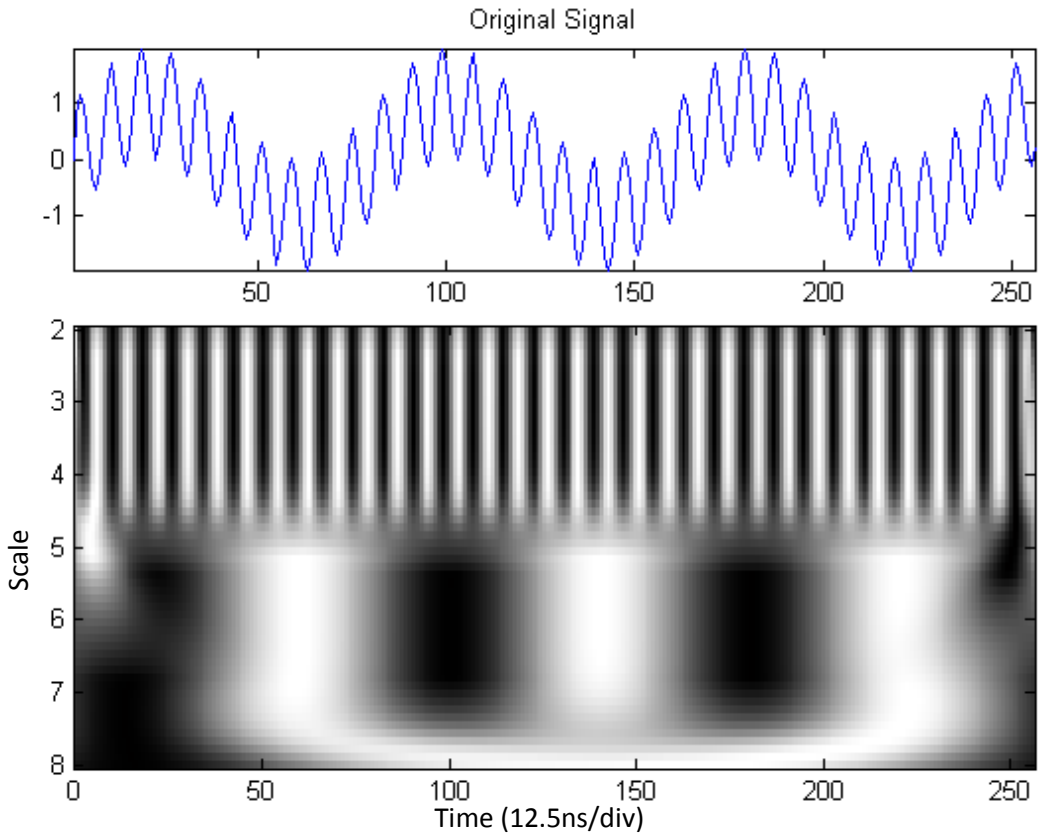

Figure 5.2: Continuous Wavelet Transform (CWT) of the convoluted signal shown at the top of the figure. A Mexican hat wavelet was used to compute the transformation. The individual frequencies are clearly separable in the transform plot.

5.3.1 Continuous Wavelet Transform

Actual computation of the transform begins with wavelet selection. This is then continuously scaled for all values smaller and larger than 1, which is clearly impossible, and thus finite scale iterations are used. The transformation begins with compact support and shifts through the signal with increasing scale. Transforms performed with this continuous increase in scale are known as the continuous wavelet transform (CWT). The results of a continuous wavelet transform using a Mexican hat wavelet and a 256 element signal of two superposed frequencies can be seen in Fig. 5.2. Assuming the signal was captured by an 80MHz, 14bit FADC then the signal shown in Fig. 5.2 would represent a 1MHz signal convolved with a 10MHz signal. These frequencies could represent noise and characteristic signals from SP1. The wavelet coefficients clearly show the presence of two individual frequencies which can now be analysed separately in the transformation, whilst the time domain representation makes analysing individual frequencies an almost impossible task. Because the CWT samples the signal over continuous scale and translation parameters it is

very computer intensive. The processing time for just one 256 element signal takes approximately 10 seconds on a relatively modern laptop and poses a limitation when dealing with millions of signals in a single run.

5.3.2 Discrete Wavelet Transform

Discrete sampling of the signal provides a huge computational gain. The signals of interest are discrete and thus only a finite number of transform convolutions are needed to completely transform the signal. The subsampling used in the discrete wavelet transform (DWT) is flexible so far as the analysis of the signal is concerned, but for signal reconstruction purposes the sampling must be restricted (section 5.5). To remove redundancy the transform tiling usually forms a dyadic grid $\{2^j\}_{j \in Z}$ in which the translation is parameterised with respect to the scale parameter. This subsampling is expressed in mathematical terms as the discrete wavelet transform.

$$\psi_{j,k}(t) = 2^{-j/2}\psi\left(\frac{t - 2^j k}{2^j}\right) \tag{5.8}$$

where j and k are integers defining wavelet scale and translation respectively. The availability of mother wavelets in the discrete case is restricted because sampling continuous wavelets does not necessarily produce a discrete orthonormal basis, which is required should the signal be reconstructed. However, the synthesis of a family of discrete wavelets such that they form an orthonormal basis of $\boldsymbol{L}^2(\mathbb{R})$ is possible. The wavelet series transform (Equ. 5.7) becomes:

$$Wf(j,k) = \int_{-\infty}^{+\infty} f(t)\psi_{j,k}^{*}(t)dt \tag{5.9}$$

This transform is practical and considerably faster to compute for large experimental runs containing millions of signals. Signals are now compactly represented on a dyadic grid. If a suitable orthogonal wavelet basis is chosen, this representation allows data to be compressed. This procedure is actually used for JPEG 2000 format and other prominent compression formats. An algorithm described in [Hol89] is implemented in [Mal99] and offers a fast algorithm based on a quadratic spline wavelet and a scaling function. All

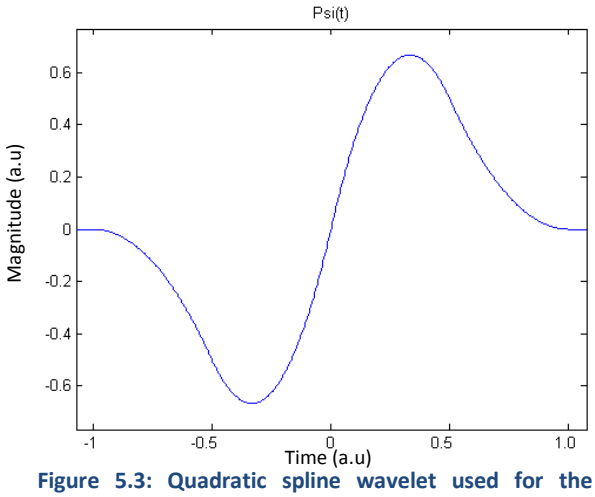

Figure 5.3: Quadratic spline wavelet used for the discrete wavelet transforms performed in this thesis.

remaining wavelet work in this thesis is based on an adaptation of this algorithm written in C for speed of execution, and specifically written to run on 256 element signals. See Fig. 5.3 for the quadratic spline wavelet. Another useful tool for exploring the theory of wavelet analysis over a range of different basis functions is Wavelab [Buc95].

5.3.3 Algorithm Implementation

Performing the transform on a dyadic grid requires a signal length of an integer index of base two. In the case were the signal does not have a length $L = 2^N$, an extension can be made by zero-padding, symmetric or anti-symmetric reflection, or periodic extension. SP1 signals are 256 elements long but only 250 elements contain the signal, the other elements contain a time stamp and the moving-window deconvolution energy. The signals are therefore extended and the algorithm begins by analysing a signal using the DWT with compact support. The most compactly supported wavelet on the dyadic grid assumes a scale of 2^1. This is equivalent of analysing the high frequency components first. This stage also acts to filter the high frequency components, and according to the Nyquist rule half the signal samples can be eliminated, since the signal does not have its highest frequency components any longer. The wavelet is then scaled to the next lowest support, which is scale 2^2 on the dyadic grid, and the remaining signal is analysed over this frequency range. The signal length is again halved and the wavelet scale increases to 2^3. The process repeats until the wavelet scale reaches the maximum size of the signal array (2^8). It is clear that

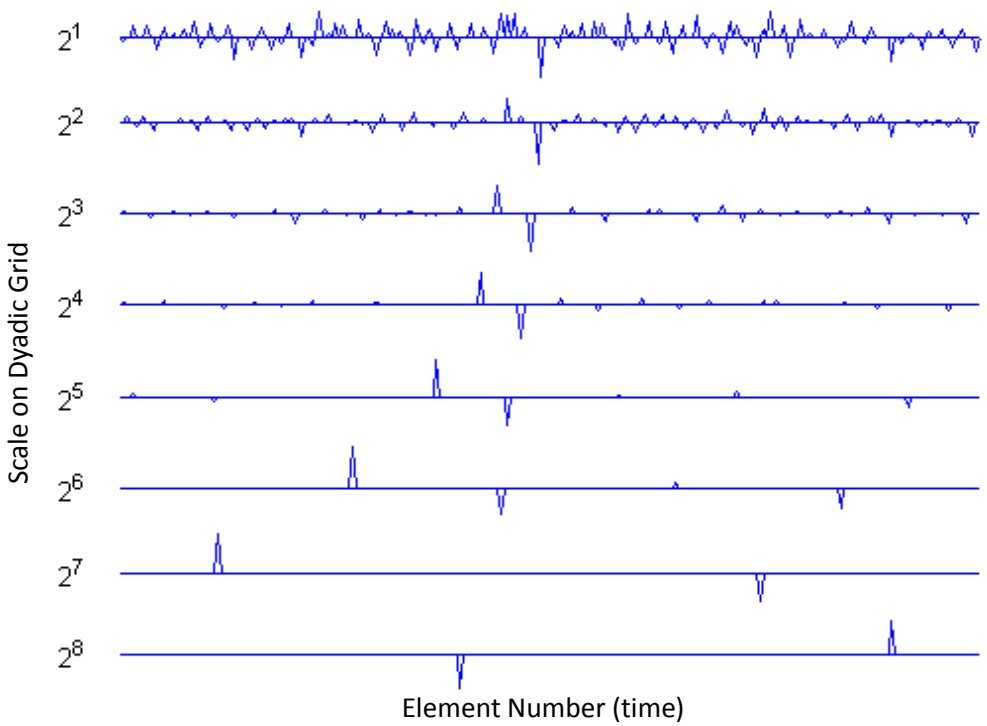

Figure 5.4: Discrete wavelet coefficients for transformation of an SP1 real charge. The wavelet scale is shown in the vertical column and the translation is represented along the horizontal direction.

there will be 128 coefficients related to high frequency after the first scale has passed through the signal. 64 coefficients after the second scale and 32 coefficients after the third until there are only 2 coefficients relating to low frequencies in the signal. An example discrete wavelet transform is shown in Fig. 5.4, which displays the coefficients individually for each scale, the scales are clearly shown on the left column. These coefficients result from a real charge from SP1 that has been transformed into the frequency domain. Interpretation of this transform can be made with special emphasis on the large coefficient which propagates through all scales. This clearly indicates a signal feature which begins suddenly in the high frequency components of the signal and rises significantly without decaying in the same signal trace. This transform can be represented in 3D which gives a clearer understanding of the signal features. Fig. 5.5 shows the 3D transformation, in which it becomes apparent that the wavelet has indeed crossed a significant feature as it is translated through the signal. This feature is the smooth leading edge of the real charge. During periods of signal uniformity the coefficients are close to zero as the mean of the wavelet is zero. During the leading edge transition, coefficients result in net negative or positive area.

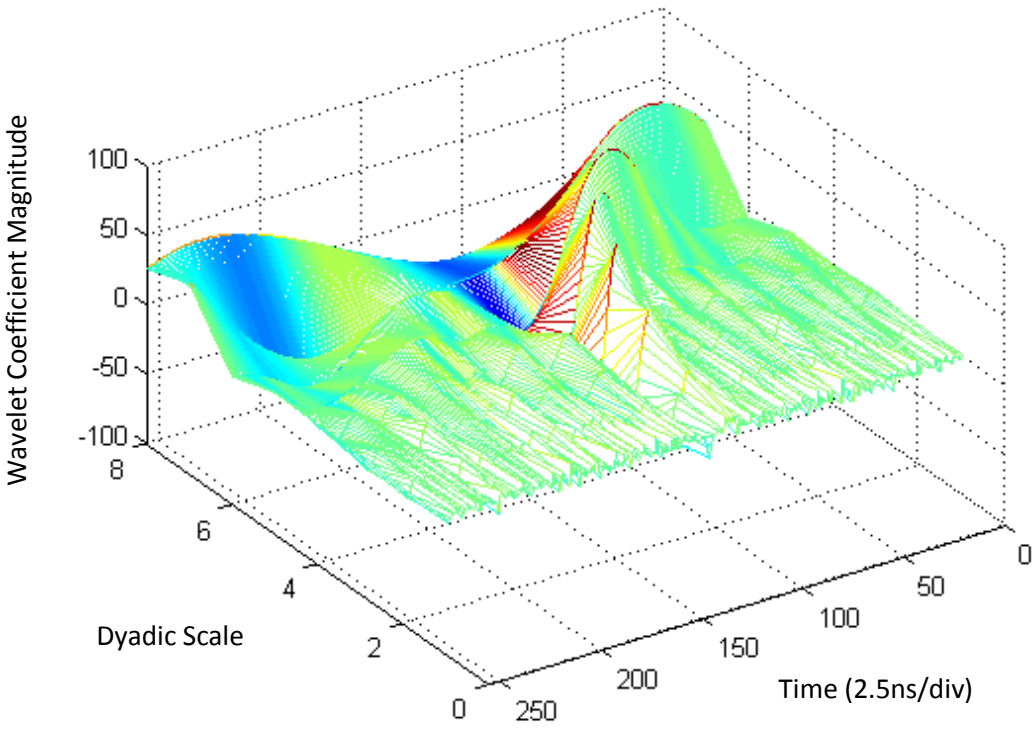

Figure 5.5: 3D representation of transformation presented in Fig. 5.4. It is easier to visualise the influence of coefficients at one scale on the subsequent coefficients. Thus signal discontinuities propagate through scale.

5.4 Transform Thresholds

The coefficients in the transform represent the signal in the time domain. These coefficients can clearly be changed, which would result in a different signal representation in the time domain. This is the fundamental principle of signal de-noising and many coefficient selection criteria have been investigated to recover signals from noisy backgrounds [Don94]. Only one thresholding technique has been considered simple enough for implementation for the SmartPET project. This applies the universal threshold [Mal99] which is a form of hard threshold based on the variance of the noise. This is calculated only once with the following and applied to all signals in an event:

$$T = \tilde{\sigma}\sqrt{2\log_e N} \tag{5.10}$$

where T is the hard threshold, $\tilde{\sigma}$ is the noise variance and N is the number of elements in the signal. Coefficients below the hard threshold are determined to belong to noise and are removed before reconstruction. This clearly also removes coefficients belonging to high

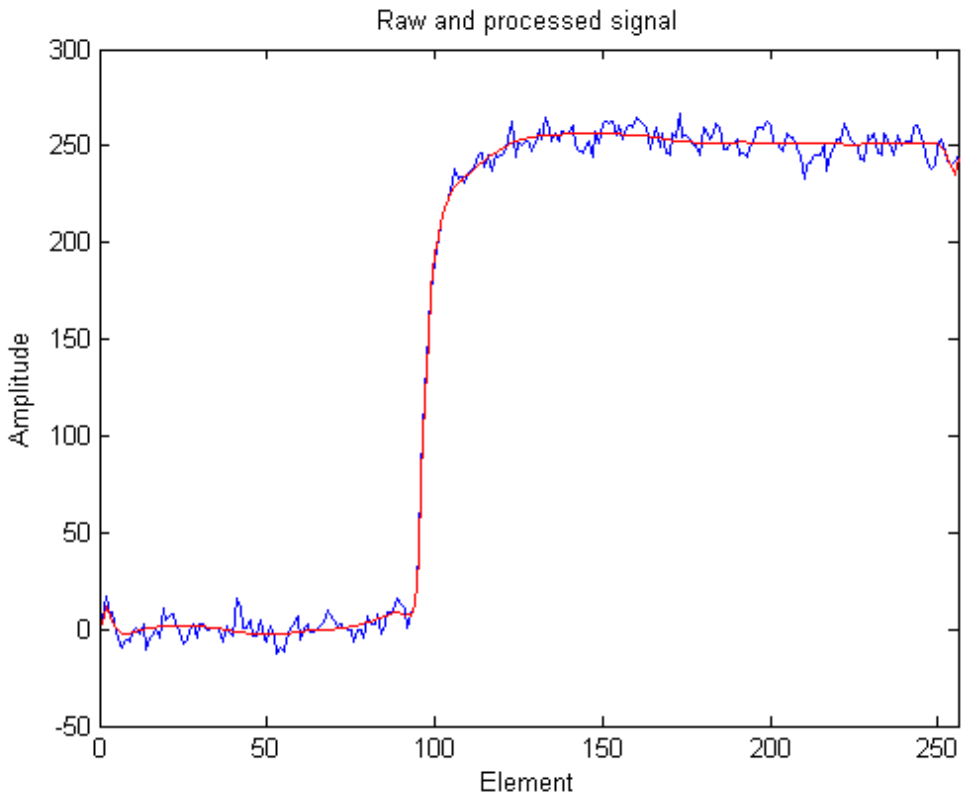

Figure 5.6: An example of a reconstruction for an SP1 real charge. The reconstructed signal is shown in red whilst the raw signal is shown in blue. The edge effects, at the beginning and end of the signal, appear because the wavelet 'crosses' a boundary. These can be removed with a mirror extension that would then require greater processing power.

frequency components of the real signal. Other transforms are available which do not remove coefficients but merely suppress likely noise coefficients. This increases the strength of singularities but introduces complexities which are beyond the needs of this project. Each coefficient would need to be analysed and a single, hard threshold is much faster to implement.

5.5 Signal Reconstruction

If the wavelets used for the transformation form an orthonormal basis set then the transform is reversible. In reality this is a very non-restrictive requirement for the continuous wavelet transform. It is the subsampling of scale and indeed translation that defines complete signal representation from linear combinations of wavelet atoms and discrete wavelets do not offer exact reconstructions. However, it is indeed possible to

recover signal approximations from wavelet maxima in the transformation. These signal approximations can define a complete and stable signal representation [Kic97] if the wavelet has a compact support. A possible reconstruction formula is given by [Mal99]:

$$f(t) = \frac{1}{C_\psi^2} \int_s \int_\tau Wf(\tau, s) \frac{1}{s^2} \psi\left(\frac{t-\tau}{s}\right) d\tau ds \tag{5.11}$$

where C is a wavelet-dependent constant, and all other terms have already been defined for the initial transform. Given the double integral it is not surprising that the reconstruction or inverse transform requires greater computational resources than the original transformation. For example, the forward discrete transform of a 256 element signal requires 11ms on a laptop running a Celeron 2.6GHz processor, whilst the inverse transform requires 356ms on the same laptop. This time is significantly reduced on a desktop running an AMD 3200+ processor, on which the reconstruction takes approximately 100ms, which includes the initial overhead of performing the forward transformation.

5.5.1 Reconstruction for a Range of Energies

Examples of signal de-noising are shown in Figs. 5.7, 5.8 and 5.9. The signals have been arbitrarily chosen to represent a range of energies that will commonly be encountered in the daily operation of the Compton camera. The effects of transform thresholding, resulting in coefficient removal, can clearly be seen in the smooth representation of signals. A user-defined hard threshold has been used in a number of the reconstructions. De-noising is not only relevant for the real charges, but also applicable to the transient-induced charges. The key group of signals which describe an interaction are therefore presented. The usual fold-1 and full-energy deposition gates were applied and the sources used were ^{241}Am, ^{57}Co and ^{137}Cs.

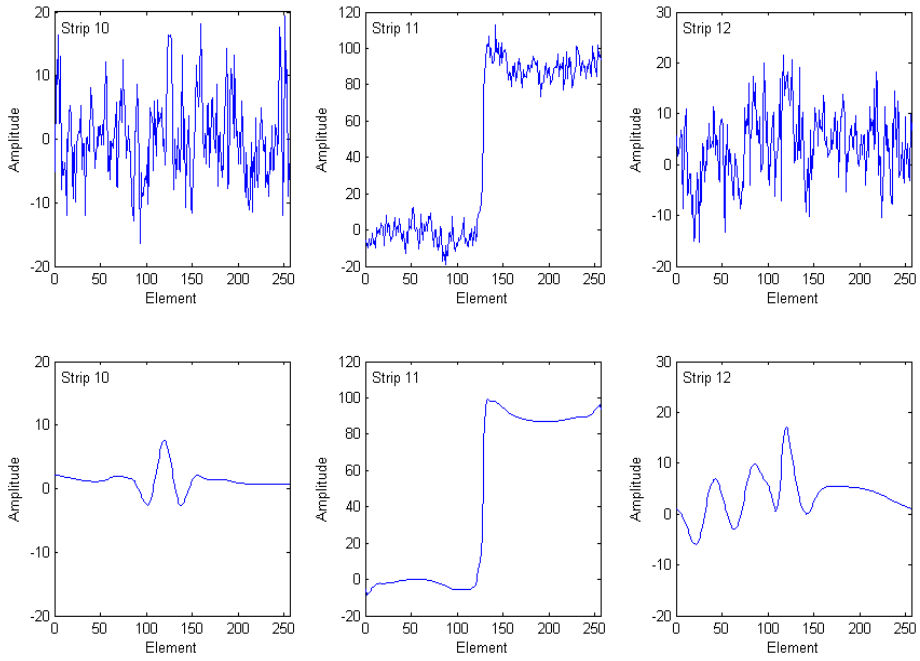

Figure 5.7: Detector response to a 60keV interaction. A universal threshold of 21 was applied to the real charge whilst a significantly greater threshold of 35 was applied to the transient induced charges to remove a greater number of coefficients. This was necessary due to the relatively large noise level on the signals. Reconstructed signals are smooth.

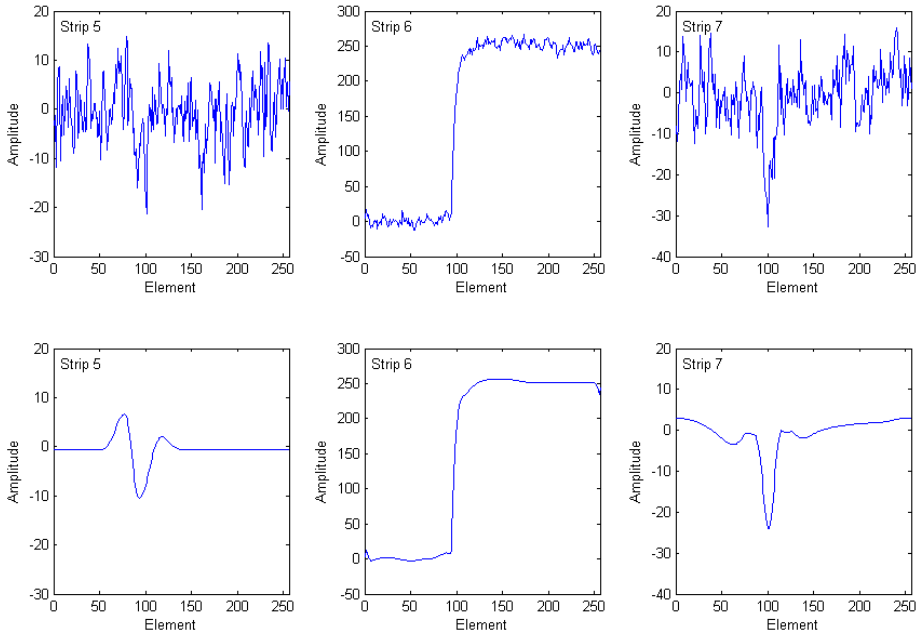

Figure 5.8: Detector response to a 122keV interaction. A universal threshold of 21 was applied to the real charge whilst a larger hard threshold of 30 was applied to the transient induced charges. The general shape of the smooth signal reconstructions show good visual agreements with the noisy signals.

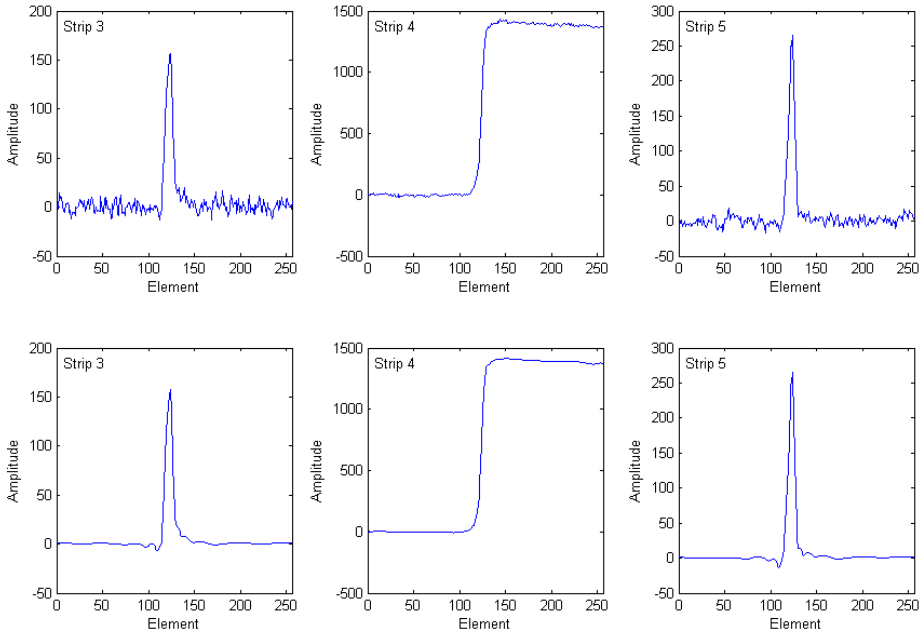

Figure 5.9: Detector response to a 'single' 662keV interaction. A universal threshold of 21 has been applied to all transforms. A very good visual agreement between the general shape of the original noisy signals and the de-noised signals can be seen.

Figs. 5.7, 5.8 and 5.9 all show a good correspondence between the smooth signal representations and what would be visually expected. The most dramatic results are for the 60keV interaction shown in Fig. 5.7. The number of charge carriers liberated in this interaction is relatively small compared with the higher energy interactions. The noise level is therefore comparatively more significant. By transforming the signal into the frequency domain, the high frequency signal components have small coefficients and are easily removed with a hard threshold. The reconstruction then contains lower frequency coefficients and the signal is smoothed. The reconstructed signal on strip 10 contains so few coefficients that the wavelet functions taken from the orthonormal basis used to reconstruct the signal have such prominence, hence the unusual signal shape. Strip 12 uses a greater number of coefficients and is therefore a more reliable reconstruction. The signal oscillation can be seen on the original signal and is well produced. The reconstructed real charge in Fig. 5.7 is a very close approximation of the original signal. The other two energies have no notable features and show very good signal approximations. The universal

threshold of 21 is calculated with Equ. (5.10) using a standard deviation of 10keV, which has been determined from a free GRT4 channel which was not recording a signal.

5.6 Pulse Shape Analysis with Processed Signals

The wavelet code used for reconstruction in the previous section can be applied on an event-by-event basis, and the results can be evaluated to determine the usefulness of performing such high-level processing on all detector signals. All wavelet analysis in this thesis was developed to coincide with parametric PSA. Hence, assuming that the analysis performed in section 4.4.5 is sufficient to increase the spatial resolution of the detector, the only requirement of wavelet analysis is to improve the sensitivity attained in section 4.4.5. The experimental basis-data-set had not been developed prior to this thesis' wavelet analysis and no testing will be performed with the basis-data-set in conjunction with wavelet analysis. The parameters produced by parametric PSA incorporating wavelet analysis are created with the same data for a fair comparison. This was the singles scan data, and therefore all results are implicit to 662keV interactions only. The usual fold-1 and full-energy deposition criteria were applied to the data so that exactly the same events were processed.

5.6.1 Real Charge Processing

Fig. 5.10 shows the *partial rise time* of $T90_{05}$ plotted against the corresponding $T30_{05}$ *partial rise time* for the same signal. All signals were de-noised with wavelet analysis before being analysed for partial rise times. A comparison of this figure with Fig. 4.13 is immediately possible. However, an important difference needs highlighting. All of the interactions that passed the experimental gates are analysed in Fig. 4.13, regardless of the triggering AC strip. Unfortunately, due to time constraints, only three AC strips were processed and allowed to contribute to Fig. 5.10; these strips were AC05, AC06 and AC07. These three strips represent 25% of the total number of AC strips and therefore a judicious comparison is still possible. There are a total of 38367 events in Fig. 5.10.

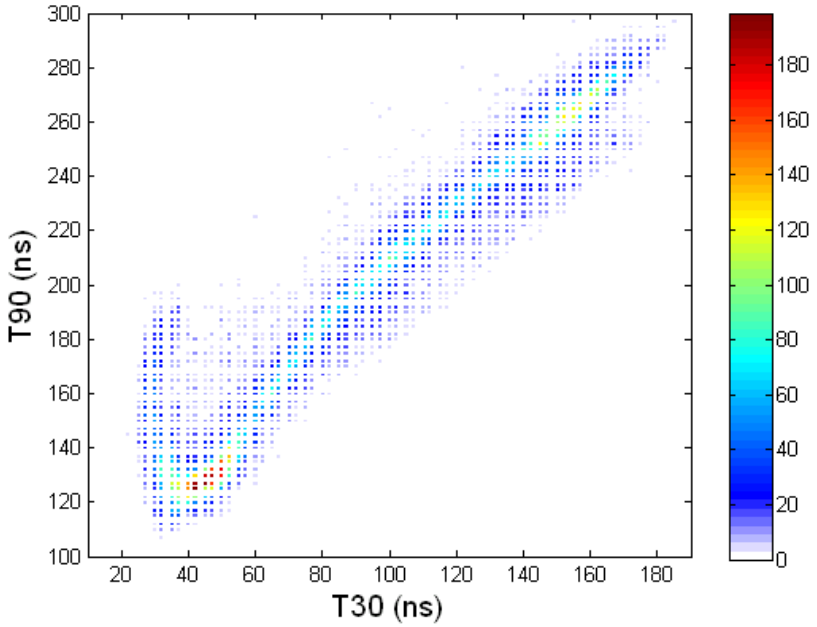

Figure 5.10: Partial rise times plotted against each other using the same data and C functions as those used for Fig. 4.13. The significant difference was the inclusion of the wavelet analysis functions. Additionally, only three strips have been analysed; a total number of 38367 events

The most apparent feature from the comparison is the strikingly similar *partial rise time* distribution. It is difficult to differentiate between the two distributions. Both distributions are narrow and turn at the coordinate (40,120). This indicates that there is no benefit gained from the large computational cost of processing. Alternatively, this also reassuringly indicates that there is no detrimental effect of signal processing. In reference to the close resemblance of original real charges and reproduced real charges for 662keV interactions (Fig. 5.9), this result is perhaps not totally unexpected. Wavelet analysis simply removes noise from a signal. However, parametric PSA uses an average value for the signal amplitude which insulates the method to a certain extent from noise because the average noise value is zero. Therefore, wavelet analysis can be deemed to be inappropriate for 662keV interactions, although wavelet analysis could yet prove beneficial for lower energy interactions. The final version of the wavelet code has been passed to project members who plan to utilise this method in the near future.

5.6.2 Transient Induced Charge Processing

The effect of wavelet analysis on the transient-induced charges can be seen in Fig. 5.11. The primary collimator was scanned in software through all x-y positions for which AC06

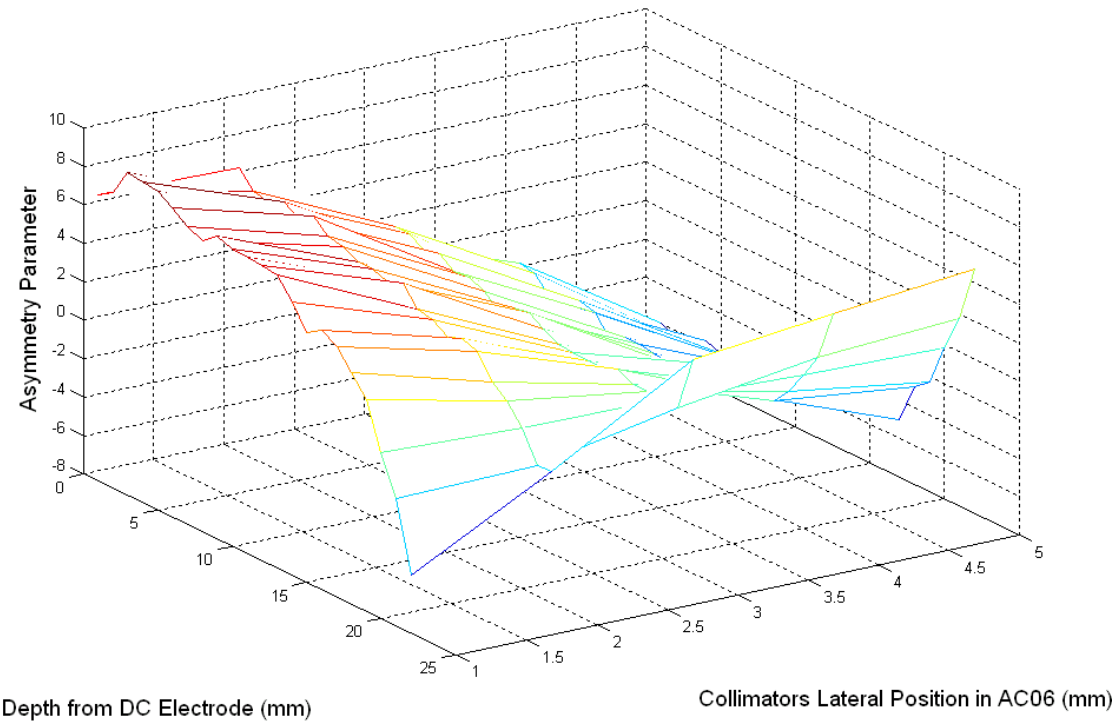

Figure 5.11: Asymmetry parameter as a function of lateral and depth of interaction. The data analysed in Fig. 4.12 has been processed with wavelet analysis and the average asymmetry parameter has been recalculated. A comparison of this figure and Fig. 4.12 shows subtle variation. Wavelet analysis does not appear to have affected the asymmetry parameter operating on 662keV signals.

triggered. The asymmetry parameter was then calculated on an individual basis for all interactions and the final average value was calculated. The singles scan was used and the usual fold-1 and energy gates were applied. The only difference between the data analysed for Fig. 5.11 and Fig. 4.12 is that the signals were processed before they were analysed for Fig. 5.11. On inspection, the processing of transient induced charges resulting from 662keV interactions appears to make very little difference. Again, the extra computational cost of processing does not appear to be justified for transient-induced charges because the asymmetry parameter does not appear to be affected. Hence spatial resolution will not be affected. Noise is dealt with in a similar fashion to the analysis of real charges. The area of the transient induced charge is calculated, to which the net contribution from noise should be zero. Indeed, a consideration of signal noise was the motivation behind using net area as a parameter. Although, if one was to revert to the method of analysing transient-induced charge magnitude [Equ.(2.38)], one would find wavelet analysis beneficial because the signal amplitude would be better defined by the smoothed signal; leading to a smaller variation for a given interaction location.

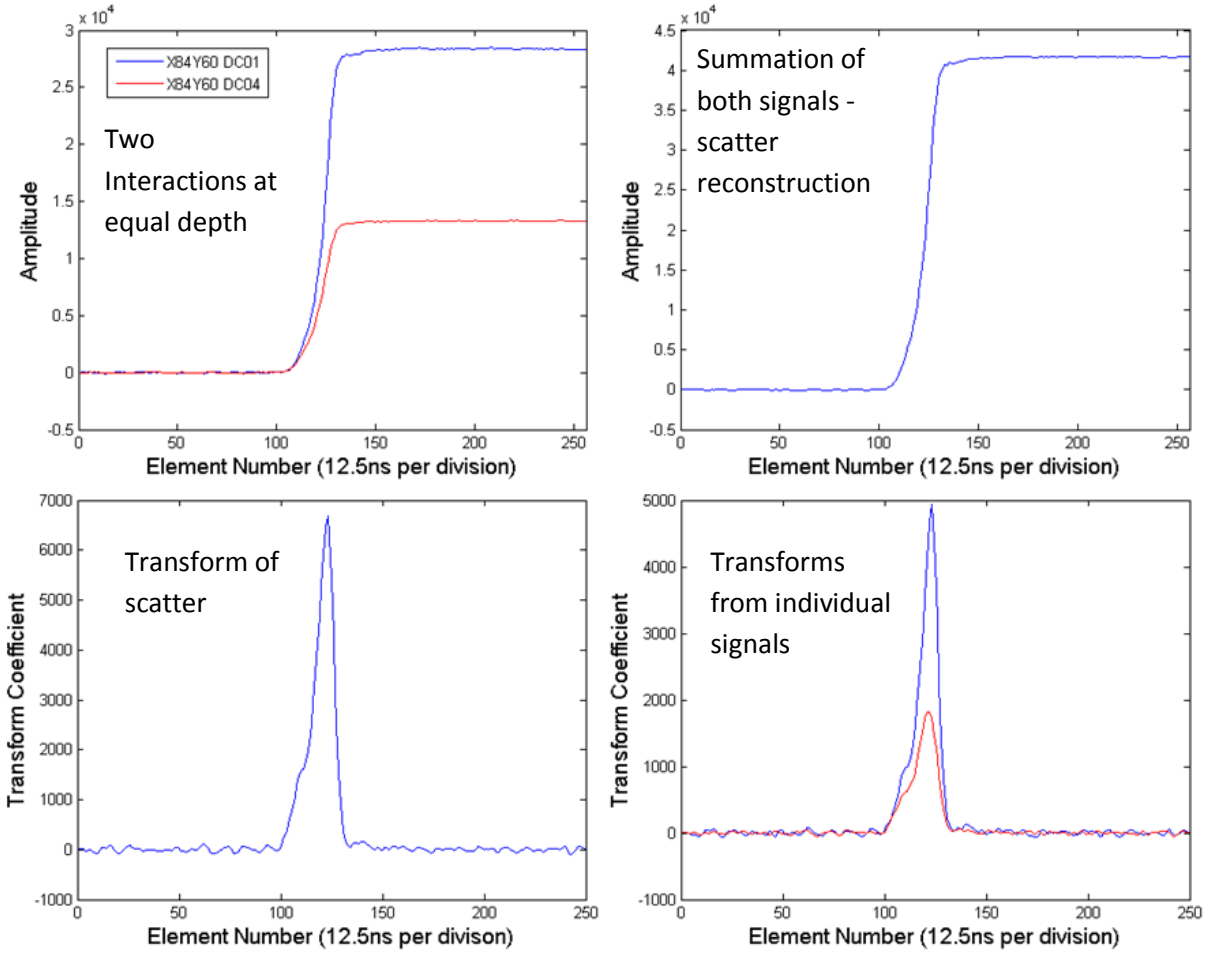

Figure 5.12: Reconstruction of in-plane scattering. Red and blue signals represent signals from the secondary-collimated scan. Both signals were recorded at a static primary collimator location (84,60). However, the signals were collected on separate DC strips (DC01 and DC04). Summing these signals together (top right) reconstructs an in-plane scatter. The bottom images represent the transform of the reconstructed signal and the individual transforms (red and blue) of the individual signals.

5.7 Identification of Multiple Interactions

An interesting application of wavelet analysis is the exploitation of the technique's ability to identify signal discontinuities. The discontinuity arises from the collection of two majority charge clouds (section 4.1.2) that are separable in time. The steepest-slope method analyses the current pulse and determines the location of the turning point, which corresponds to the collection of the majority charge carrier. Two majority charge clouds will result in two turning points on the current pulse. Now, the charge pulse is effectively the integral of the current pulse so that two majority charge clouds result in a signal discontinuity on the charge pulse. Scattering is ordinarily not a problem in spectroscopic measurements if the

full energy is deposited. However, Compton scattering is the most probably interaction in germanium for photons above 150keV (Fig. 2.1) and if germanium is to be used for imaging or gamma-ray tracking then attempts must be made to identify Compton-scattered events.

The significance of scattering on spatial resolution, is that simple parametric PSA can only identify a mean charge cloud inside of the detector active volume, so that a *single* interaction position is determined. Although fold gates can be applied to suppress scattered events, if multiple interactions occur in the same close-face-pixel then a single interaction position will be determined, which is clearly erroneous. These events need to be identified so that caution can be taken in image reconstruction, and poor quality events subsequently carry less significance than good events.

5.7.1 Compton Scattering Reconstructions

It is possible to reconstruct the response of SP1 to Compton-scattered events with data from the measurements made in the previous chapter. That is, of course, assuming that all of the recorded events in the previous chapter resulted from single-site interactions. These reconstructions can then be used to develop the technique which will be used to identify them. This has been performed and the technique has been tested on real data. The methods and example results are the focus of the remaining chapter. Compton scatter reconstructions have been performed using both the uncollimated and collimated scan. A Compton-scatter real-charge response has been reconstructed from each scan. Only the real charges have been employed in the reconstruction because the transient-induced charges are not used to identify scattering. One response reconstruction has been chosen for two random interaction sites that are disparate through depth (*in-line* scattering), whereas one reconstruction is purposely designed to represent *in-plane* scatters, for which it has been proposed that these types of event are unidentifiable (section 4.4.3).

Fig. 5.12 and Fig. 5.13 show both the *in-plane* and *in-line* reconstructions respectively. The individual signals are shown in red and blue. These are then summed to recreate a scattered event. The difficulty in determining t_0 has prevented any time alignment and the resulting summation is not a true reconstruction but only a best attempt. For the purposes of

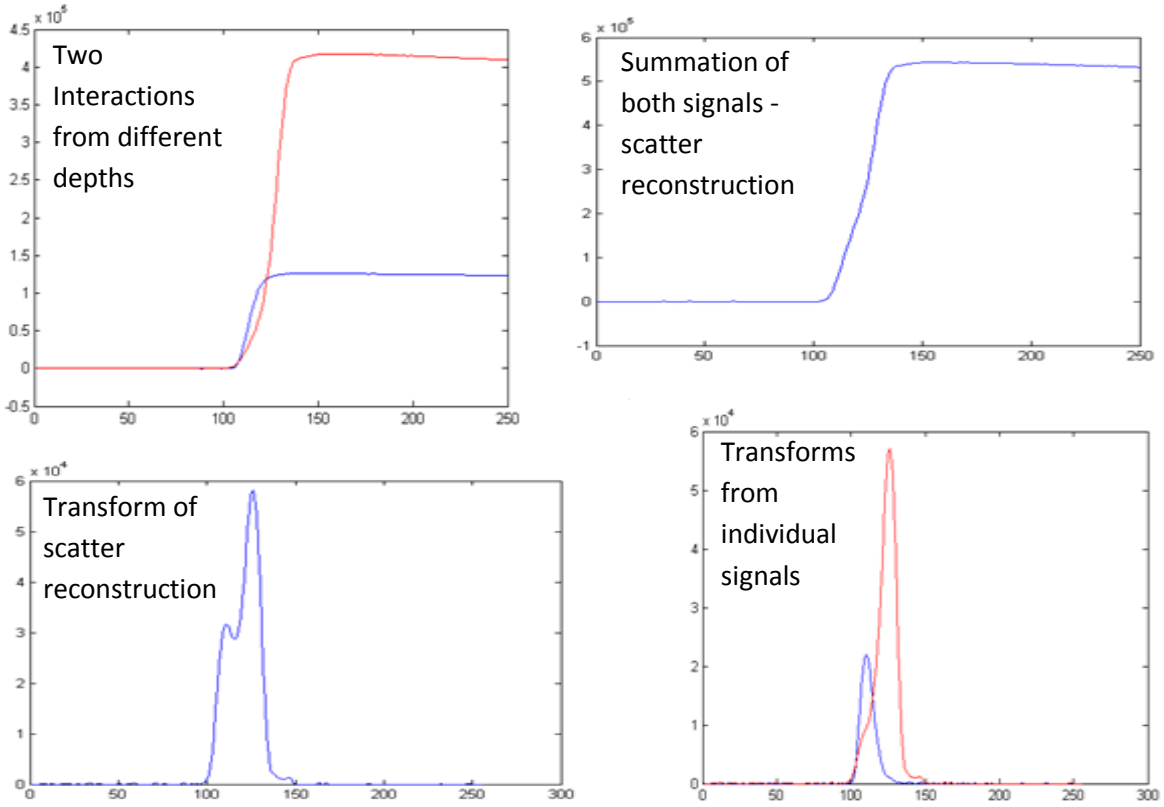

Figure 5.13: Reconstruction of *in-line* scattering. Red and blue signals represent signals from the uncollimated scan. Both signals were recorded at a different primary collimator locations (104,57) and (104,70). All DC signals contribute. Summing these signals together (top right) reconstructs an in-line scatter. The bottom images represent the transform of the reconstructed signal at scale 2 and the individual transforms (red and blue) of the individual signals. Note: axes are identical to Fig. 5.12.

creating a dyadic grid, the signals have been left in their original form without interpolation. They have also bypassed the normalisation C functions. This method is then ready to be directly implemented in the pre-processing chain, which would increase the operational speed of analysis by avoiding unnecessary analysis of scattered signals. The top left images in both figures show the two individual signals that are amalgamated, whilst the top right image shows the resulting reconstructed signal. The bottom images show transforms at a user-selected scale.

5.7.2 Digital Compton Suppression (DiCS)

In consideration to what is known about detector response to a scattered event, and what has been presented in relation to wavelet analysis, it should be a simple case of performing a transformation to identify a scattered event. The transform holds coefficients which relate

to the product of a wavelet (at a particular scale) and the original signal (at a particular frequency), at a particular translation. Thus, as the wavelet is translated through the signal, it is effectively interrogating the frequency components of the signal at discrete translations. A multiple interaction has a discontinuity and a sudden change in frequency on the leading edge, which will cause a sudden change in the transformation at a related scale. By performing the transformation this discontinuity becomes strikingly apparent in a number of transform arrays at different scales. It is necessary to make a judicious choice about which scale should be analysed. Picking the wrong scale would severely limit this technique. Based on inspection of a number of transformations it has been decided for the work in this thesis that scale 2 (2^2) is a good choice.

The transformation arrays at scale two are shown for both scatter reconstructions in Fig. 5.12 and Fig. 5.13 in the bottom left images, and the transforms of the individual signals are shown in the bottom right images. The transform in Fig. 5.12 shows large, gradually-changing coefficients, and small, fast-changing coefficients. The small coefficients result from noise, but the magnitudes of these coefficients are severely suppressed at this scale because there is only a small probability that noise can contaminate the lower frequencies in the transformation. It should be emphasised that this pivotal point is the key in using wavelet analysis to identify Compton scattering. The inability of high frequencies to penetrate the lower frequencies can be seen in Fig. 5.4. The lower-frequency signal features of the real charge result in large coefficients when the transform is performed at larger scales. Hence the salient features of the signal can be analysed without the inconvenience of noise once an appropriate threshold is applied to the transform array which should remove all noise components. The threshold used is simply an adjusted universal threshold of section 5.4. Inspection of the transform array Fig. 5.12 (bottom left) would indicate that scattering did not take place because no signal discontinuities were identified on the leading edge.

Inspection of the corresponding transform array in Fig. 5.13 results in a very different conclusion. A sudden change of instantaneous frequency can be seen in the transform array. This would indicate a sudden incident on the leading edge of the real charge in which the signal was irreparably changed. This change is simply the cessation of one majority charge cloud and the continuation of the second charge cloud. Hence the signal has been identified

as scattered and it can be partially concluded that wavelet analysis can be used to identify *in-line* scatters but not *in-plane* scatters. Only two single events have been reconstructed due to the lack of time alignment, resulting in experimentally-different test conditions. This is then clearly not a stringent test of Digital Compton Suppression (DiCS). It is perhaps more appropriate to simply move this technique straight to real scattered-data, which will naturally be time aligned. It is worth noting the technicality of identifying the discontinuity is literally as simple as applying a threshold to the transform array and identifying the number of turning points.

5.7.3 Real Data Testing

Performing a stringent test of DiCS requires true Compton-scattered data. This is easily attained by gating on the fold of an event. If the event is fold-2 (section 3.6.1) then one AC/DC strip triggered and two DC/AC strips triggered. Neglecting random events, these types of event are then assumed to be a Compton scatter or *charge sharing*. The percentage of events *charge sharing* is expected to constitute a small fraction although no estimate for SP1 has yet been determined. However, to remove the possibility of charge sharing, the two strips that trigger on the AC/DC electrode face can be required to be non adjacent. It is then assumed that the recorded event is most probably a simple Compton scatter between these non-adjacent closed-faced pixels.

A ^{137}Cs sealed point source was placed in front of the cryostat of SP1 directly facing the AC electrode. The fold requirement of an event was that one AC electrode triggered and two DC electrodes triggered. This was then made more restrictive with the addition that the DC electrodes could not be adjacent. A total of 70149 fold-2 events were recorded, reducing to 9201 events with the more restrictive criterion. Performing DiCS on these events with a threshold of 21 on the transform array at scale 2 results in the identification of 22240 (32%) possible scattering events and 5062 (55%) possible scattering events, for the fold-2 data and fold-2 + non-adjacent data respectively.

The integrity of the results can be confirmed by inspection. A program has been written that allows one to visually inspect DiCS operating in time lapse mode on these data. The program

pauses and displays each signal and associated transform array for a user specified amount of time, or simply fast forwards through the events when input is received via the return key. The technique appears to perform remarkably well, and is almost always in agreement with a reasoned inspection. The program is available on request.

Two signals have been arbitrarily chosen to demonstrate typical signals that are identified and not identified by DiCS. These signals may have resulted from *in-line* and *in-plane* scattering and would therefore represent the best case and worse case for identification. These signals are from the first data set. The best case scenario for identification is shown below for which a discontinuity is clearly seen.

Fig. 5.14 demonstrates the steps taken towards identification. This signal most definitely has signal features in common with the reconstructed in-line scatter shown in Fig. 5.13. It was these features that identified the signal (Fig. 5.14a) as a scatter, and it is assumed that the code has indeed operated on real data and identified a true scatter. A threshold of 21 was applied to the transform. This method can clearly be optimised. An example signal which was not identified is shown in Fig. 5.15.

Fig. 5.15 represents a signal that has not been identified. Fortunately, the transformation looks similar to that for the reconstructed *in-plane* scatter and a reasoned analysis would agree that it would be unlikely for these types of event to be identified. In reference to Fig. 5.15c, it can be seen that there are almost two turning points above a magnitude of 21, which results from noise at the very top of the leading edge of Fig. 5.15a. Noise occurring at this position can be accounted for by placing a condition on the transform which requires that the second turning point is significant. DiCS is clearly not optimised and the transform array that is analysed is not fixed and could easily be greater or smaller than 2. Further optimisation is possible and is discussed in the final chapter. Performing this technique on a number of signals and inspecting the results does imply that this is a very powerful technique. However, future directions of DiCS will depend on the need to identify scattered signals and the reliability of competing pattern recognition algorithms. It is difficult to judge how important scattering identification is, it should simply improve image quality, which is itself subjective.

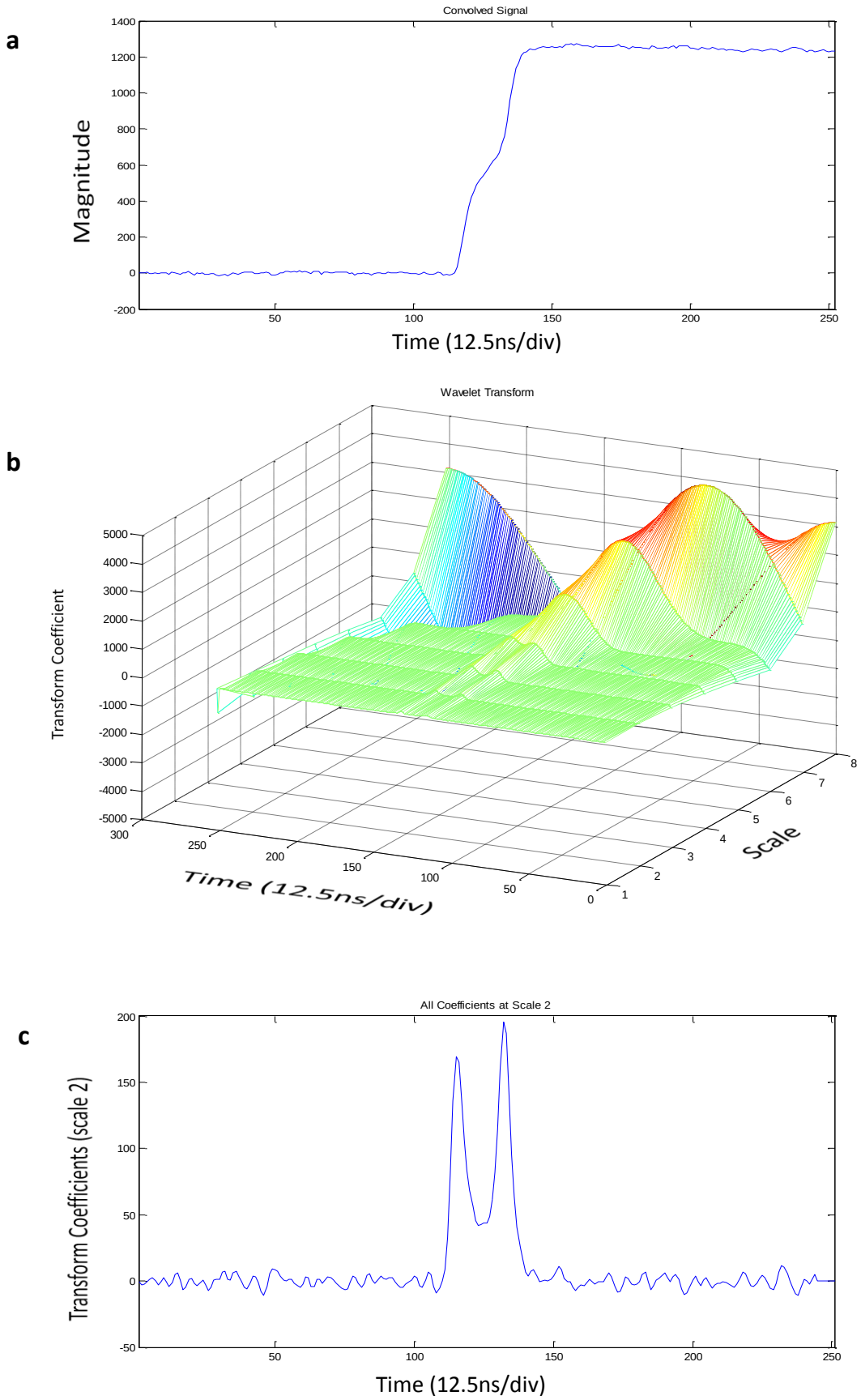

Figure 5.14: The very top signal (image a) represents a signal that has been identified as a Compton scatter. The middle image (image b) represents the transformation of this signal into the frequency domain, in which a signal discontinuity can be seen in a number of transform arrays. The bottom figure (image c) is the transform array at scale 2. The signal discontinuity is clearly apparent in this image, accompanied by noise.

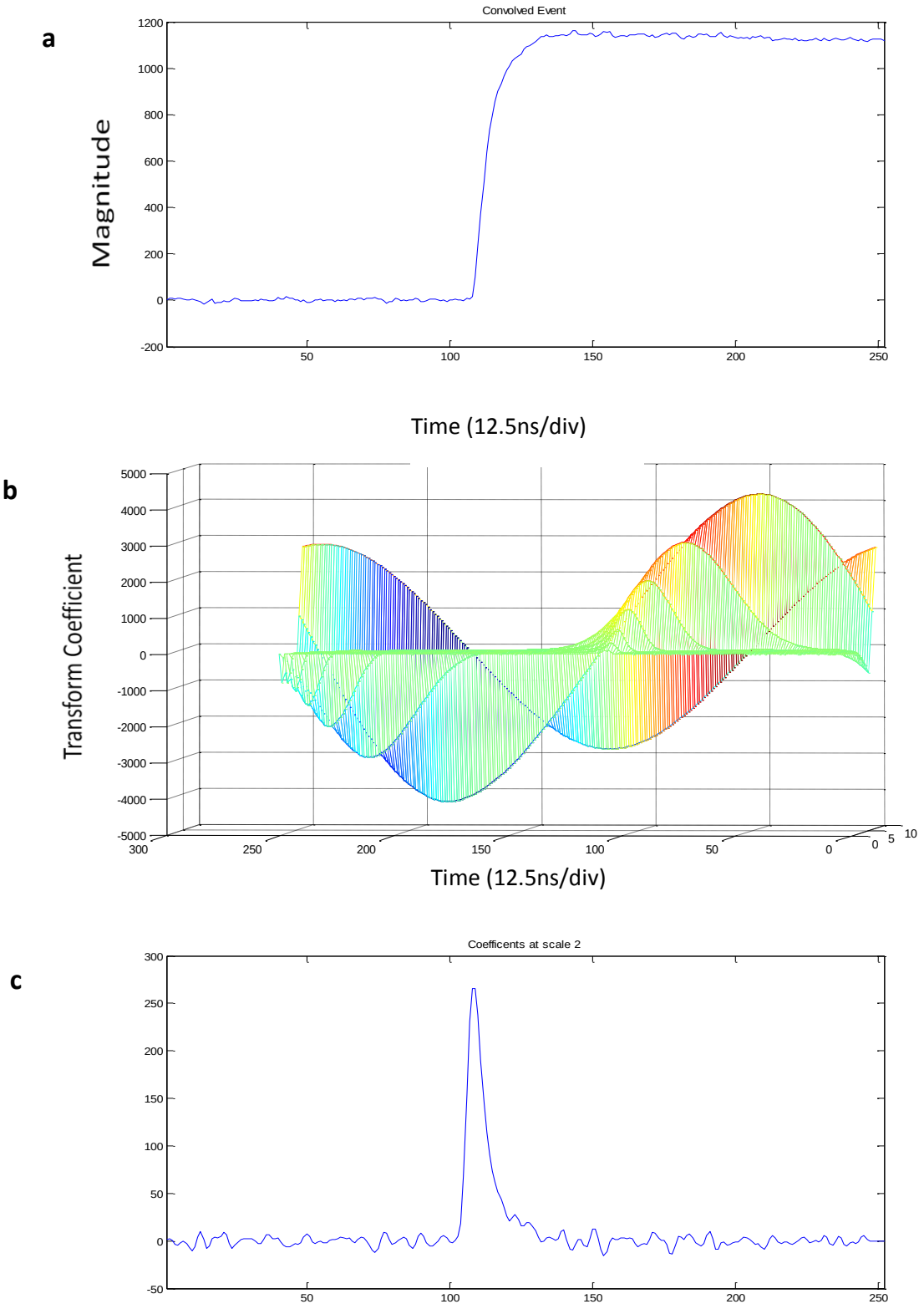

Figure 5.15: Image (a) represents a signal that has not been identified as a Compton scatter. Image (b) represents the transformation of this signal into the frequency domain. The unusual perspective is used to give a better view of any discontinuities. Image (c) is the transform array at scale 2. No signal discontinuities are present in this image.

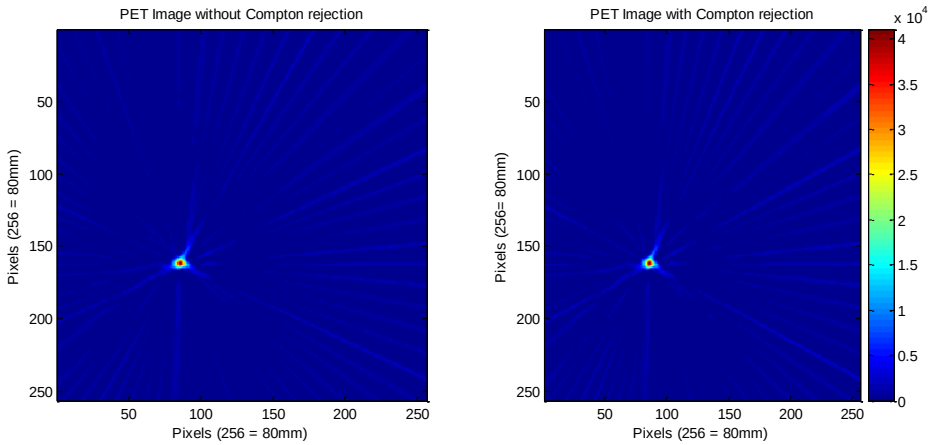

Figure 5.16: PET images of a Na-22 point source with and without Compton rejection. Images were produced from parallel beam LORs only and therefore show very little dependence on depth. The FWHM without Compton rejection is 3.44pixels and 3.37pixels with Compton rejection.

Sophisticated imaging codes which would benefit from the rejection of scattering events do not yet exist for SmartPET or are currently under development. The most sophisticated imaging code to date is a positron emission tomography code written by Andrew Mather [Mat06], which took an intensive 3 years to write and is currently being modified by another PhD student. However, at present DiCS has only been incorporated into the code presented in [Mat06]. The results are shown in Fig. 5.16 in which the left image represents an image without DiCS and the right image incorporated DiCS. The FWHM was improved but not significantly. This was expected because DiCS identifies scatters through depth (*in-line*) and the imaging code simply works on opposite lines of response so that the depth of interaction is almost inconsequential. However, although the actual image failed to show an improvement, two examples of an identified scatter and a non identified scatter did indeed indicate that the digital Compton rejection was successful. The arbitrary signals are shown in Fig. 5.17. The first two images are composed of an identified scattering and a non identified scattering respectively. The second two images are enlargements of the first two images respectively. The discontinuity is not apparent in the unmagnified image, but when the image is enlarged it is reasonably apparent that the signal was correctly identified as a scatter. The unidentified signal would also appear to be correctly identified by inspection of the enlarged image as a non-scattered response. It should be noted that for Fig. 5.16 the extra criteria of two significant turning points in the transform was applied. The development of a Compton camera imaging code is described in the next chapter but has not been amalgamated with the DiCS C-code.

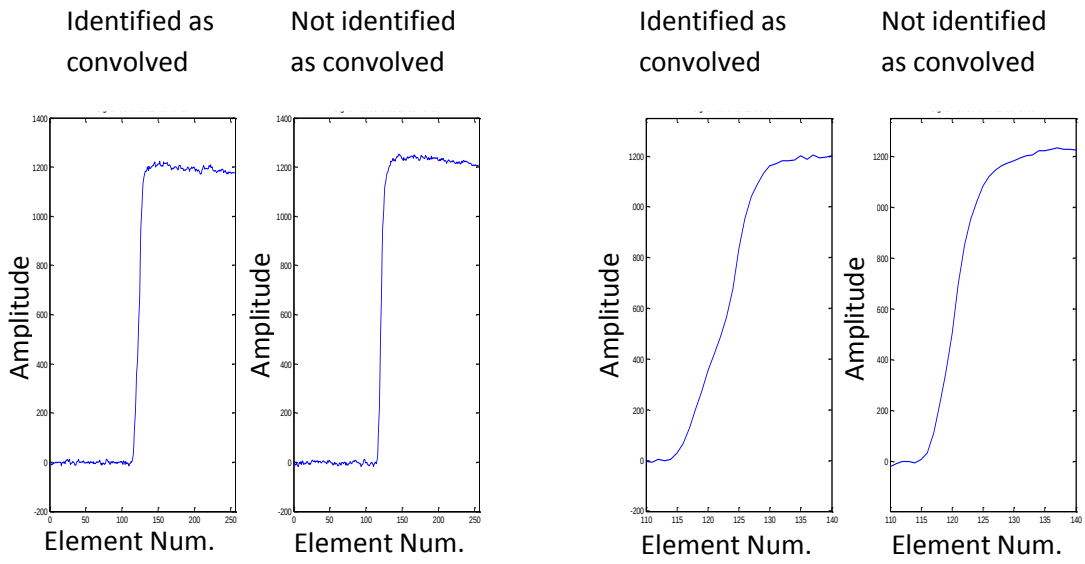

Figure 5.17: Left hand figures show two signals; the first signal was identified as convolved by the method developed, the second signal was not identified as convolved. Right hand figures zoom in on both signals respectively; signal identified as convolved due to kink on leading edge, signal not identified as convolved has no such signal discontinuity. This figure shows the sensitivity to convolved signals.

Chapter 6

Compton Camera

Single photon imaging in nuclear medicine currently relies on mechanical collimation to form projections of spatially-distributed sources. Chapter 1 describes this technique in detail, in which the detection sensitivity is inversely proportional to the spatial resolution of the image. In contrast, Compton cameras assign directional information to incident photons that scatter within the camera system according to the kinematics of a particular event and the Compton scattering formula. Hence, the sensitivity issues arising from the use of mechanical collimation are avoided. Excellent energy and spatial resolution are clearly fundamental components of a Compton camera. Accordingly, the preceding chapters were designed to develop and test possible solutions which can be used to extract the location of interaction from the detector response. A selection of these methods will now be utilised to image isotropic and anisotropic sources. Intuitively, image quality should be directly related to the best possible attainable position resolution. A simple analytical imaging code, which avoids statistical or filtering methods to improve image quality, is therefore required to evaluate the affects of spatial resolution. A simple back projection code was developed from first principles and constructed in a series of MATLAB functions and scripts. This was subsequently validated with simulated data before being used with real data.

6.1 Compton Cameras

The principal idea behind the operation of a Compton camera has been around for several decades. Indeed, many articles detailing actual Compton cameras have been published for

various fields of research with astronomy, medical and industrial applications being the main motivations. The first paper which explicitly details gamma-ray imaging through the exploitation of the kinematics of Compton scattering without the use of collimators came from the astronomy community, in which a telescope composing of a scattering scintillation detector coupled to an absorbing scintillation detector was described [Whi68]. This telescope was carried on a balloon in 1971. Further gamma-ray telescopes were developed with the most notable being COMPTEL [Sch77], which was satellite-based and launched in 1991 becoming the first Compton telescope in orbit. COMPTEL also produced the first ever all-sky survey in the 0.75-30MeV energy region and revealed the distribution of relatively recent supernovae remnants characterised by ^{26}Al, along with much younger supernovae characterised by ^{44}Tl. COMPTEL was purposely crashed into the pacific on June 4th 2000 after a single gyroscope failed. Replacement semiconductor telescopes are planned.

The first Compton camera for use in nuclear medicine was described in 1974 [Tod74]. This paper proposed using an array of orthogonal silicon detectors as the detection medium. Systems based on planar germanium technology were subsequently devised and constructed [Sin81]. Image reconstruction methods were applied and tested with ^{137}Cs and ^{99m}Tc point sources [Sin83a]. The germanium scatter detector was 6mm thick and achieved a resolution of 1.3keV FWHM at 140keV. Superior image quality was found with an algebraic reconstruction technique (ART) which is a common iterative technique. This camera demonstrated the feasibility of using electronic collimation in nuclear medicine for the first time. The germanium research detector, which was fabricated at Berkeley, was lent to the University of Michigan by M. Singh for evaluation of other possible applications, namely the monitoring nuclear wastes [Mar93].

A number of Compton camera designs have now been implemented for nuclear medicine applications. Various detector materials are employed in these camera systems including: xenon [Bol97], silicon [Cli98], germanium [Piq04] and CZT [Leh04]. Indeed, hybrid detection systems make highly-suitable Compton cameras. In contrast to these detection systems which closely follow the methodology of using two cameras, some groups have actually begun imaging with single detector systems [Xu06] [Kur04]. Compton cameras have now successfully imaged various source configurations utilising both monochromatic and polychromatic sources in a combination of isotropic and anisotropic geometries. SmartPET

collaborators in Melbourne have recently reconstructed images of a point source under various configurations with data that were collected at Liverpool [Gil07]. The reconstruction algorithms that were used all feature statistical and iterative methods. However, although indirect reconstructions provide good quality images they do not directly relate image quality to the spatial resolution of the detector, for which an analytical code is needed.

6.2 Compton Camera Performance Factors

Spatial resolution, energy resolution and detection sensitivity are the key attributes which govern the performance of a classical Compton camera. Spatial and energy resolution have intrinsic limits which have been discussed within this thesis, these limitations propagate into cone axis and opening angle uncertainty, ultimately degrading the final image. Detection sensitivity is clearly related to geometrical effects and optimisation is possible. A brief discussion of optimal geometries, possible image reconstruction techniques and the combination of resolution limitations is now given for a complete understanding of the dynamics of a classical Compton camera.

6.2.1 Efficiency

The definition of a classical Compton camera requires a photon to scatter in the scattering detector and subsequently escape only to become absorbed in the absorbing detector. Useful events are then selected when the sum of the energy deposited in the two detectors add-back to the incident gamma-ray energy. Models have been developed to quantify the probability of such an event occurring in a Compton camera [Sin83b] and the fraction of valid events that are useful from a total number of photons emitted is given by the absolute camera efficiency [Mar94].

$$\in_{acc} = \left(\frac{\Omega_1}{4\pi}\right) P_c f_2 \in_{ip2} \tag{6.1}$$

where the term in the parentheses represent the probability that a photon emitted by the source falls in the solid angle subtended by the first detector, P_c is the probability that a

photon scatters in the first detector and escapes within a prescribed solid angle subtended by the second detector, f_2 is the probability that the scattered photon will fall onto the second detector and $\in_{ip\,2}$ is the intrinsic efficiency of the second detector as given by Equ. 2.36. P_C is a function of: the scattering angle probability as obtained by the Klein-Nishina distribution (Equ. 2.8) for a particular energy, the linear attenuation coefficient at a particular energy (Equ. 2.2) and the Compton cross section at a particular energy (section 2.1). The efficiency of a Compton camera is therefore also a function of energy. However, the Compton scattering cross section varies by only a factor of 3 between 100keV and 10MeV and it is found that the scattering angle is the most dominant factor for efficiency. This is a geometrical effect which can be optimised by design. Example efficiencies reported by Martin [Mar94] vary from 2×10^{-4} at 662keV to 1×10^{-4} at 1.37MeV for a fixed crystal separation of 30cm, whilst efficiency is quoted as 1.5×10^{-2} for 662keV with a separation of 10cm. It is perhaps unsurprising that the minimum separation between the scattering and absorbing detector results in the most efficient Compton camera geometry.

6.2.2 Angular Resolution

Common to all Compton cameras is the scattering formula (Equ. 2.7) which is used to extract angular information (θ) from a scattered event. This information is then used to construct a cone in relation to a cone axis which is defined from the two positions of interaction. Energy uncertainty affects the determination of θ, whilst position uncertainty affects the direction vector and vertex of the cone. These two independent uncertainties can be added in quadrature to give a total angular resolution. However, the individual contributions from spatial and energy uncertainty need to be considered independently first.

Energy resolution is a combination of uncertainty arising from intrinsic energy resolution and Doppler broadening (section 2.5.5). If Doppler broadening is neglected then the principal uncertainty in estimating θ is given by the differential of the Compton scattering equation [Rog01]:

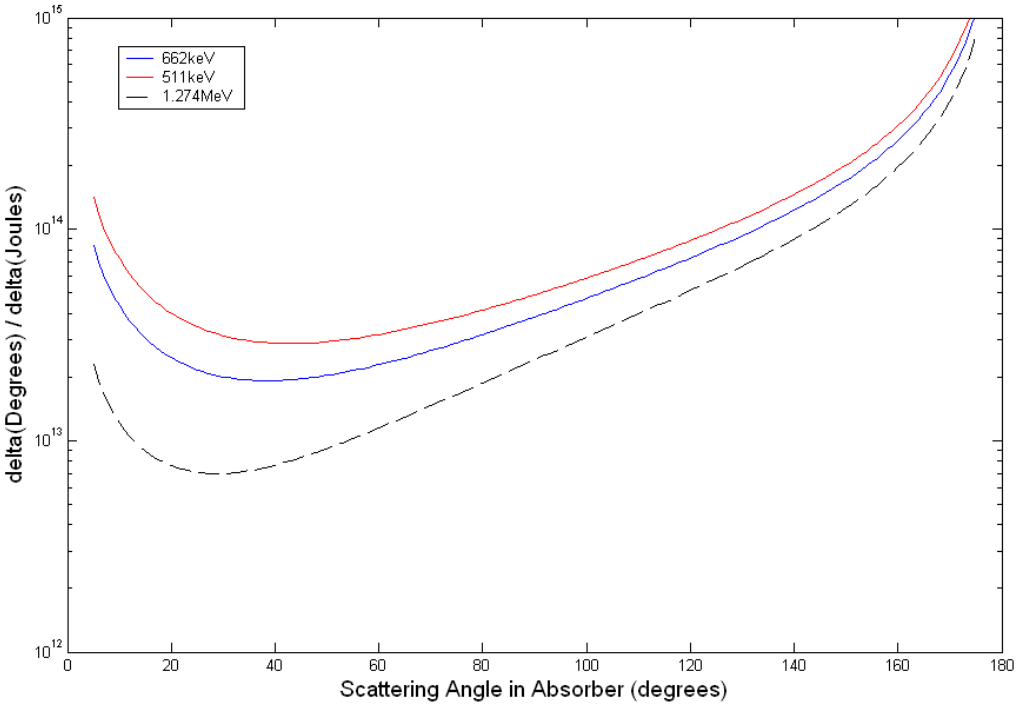

Figure 6.1: Variation of angular uncertainty divided by energy uncertainty against scattering angle for a number of energies. The smallest angular uncertainty is for scattering in the region of 20° to 40°. Large angular uncertainty is introduced from low angle scattering or high angle scattering.

$$\Delta\theta_{E_i} = \frac{(2-\cos\theta)^2}{E_\gamma \sin\theta}\Delta E_i \tag{6.2}$$

where, $\Delta\theta_{E_i}$ represents the angular uncertainty from the intrinsic energy resolution ΔE_i, and E_γ is the incident photon energy. Equ. 6.2 indicates that the angular uncertainty resulting from the intrinsic energy resolution improves with increasing gamma-ray energy. This can also be seen in Fig. 6.1 which plots the variation of $\Delta\theta_{E_i}/\Delta E_i$ against θ for three photon energies. This derivative becomes infinite at scattering angles of 0° and 180° and has a minimum of angular uncertainty for 40° scattering at lower energies, moving towards 20° for higher energies. However, geometrical factors limit the scattering angle to ≤60°.

The contribution of Doppler broadening can be summed in quadrature with the contribution from the intrinsic energy resolution of the detectors, provided that Doppler broadening is considered as a normal Gaussian distribution. The contribution from Doppler broadening, ΔE_{Dop}, is given by [Hir03]:

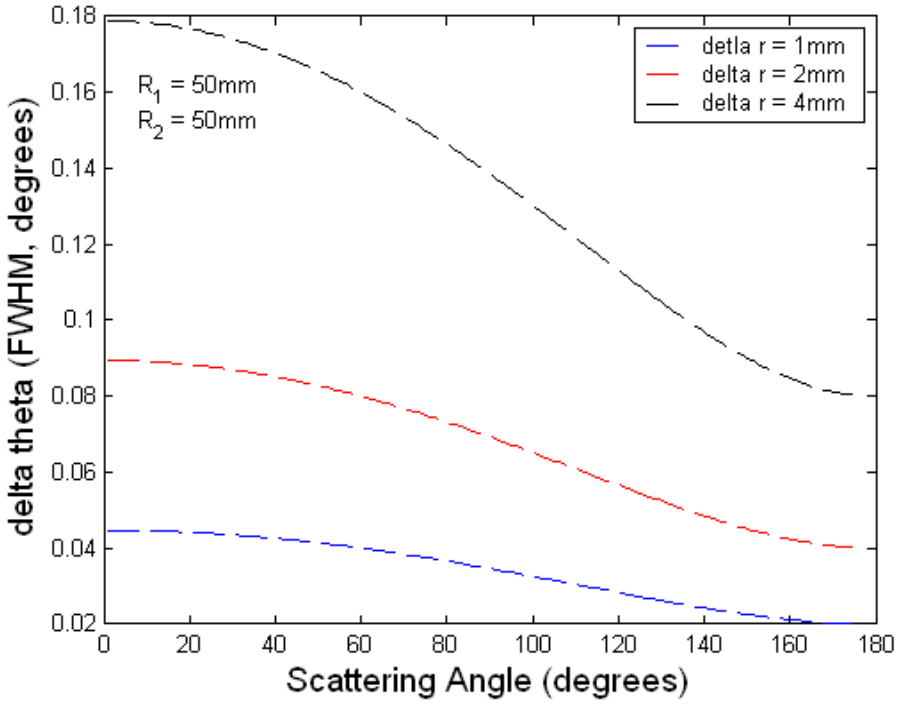

Figure 6.2: Angular uncertainty resulting from the spatial resolution of a Compton camera, where, R_1 is source to scattering site distance, R_2 is scatter site to absorption site distance and delta r is the spatial uncertainty of the interactions.

$$\Delta E_{Dop} = K\frac{E_\gamma - E_{\gamma'}}{E_\gamma}\sqrt{E_\gamma^2 + \left(E_\gamma - E_{\gamma'}\right)^2 - 2E_\gamma\left(E_\gamma - E_{\gamma'}\right)\cos\theta} \tag{6.3}$$

where, K is a constant for germanium (1.43×10^{-2}) which is related to the width of the Compton profile, E_γ is the incident energy, $E_{\gamma'}$ is the scattered photon energy and θ is the scattering angle. The net energy resolution is then given by Equ. 2.34. Although silicon has desirable properties for a scattering detector (section 2.3), it also has larger Doppler broadening than germanium and its proposed use a scattering detector [Gri07] is a compromise between efficiency and angular resolution.

Uncertainty of interaction location is a consequence of noisy pulse shapes resulting in a distribution of possible cone direction vectors and vertices. Each detector introduces an individual angular uncertainty $(\Delta\theta_s, \Delta\theta_a)$. These can be summed in quadrature to give the total angular uncertainty from spatial uncertainty. However, if the spatial resolution is isotropic in each detector $(\Delta x = \Delta y = \Delta z = \Delta r)$ and each detector has equivalent spatial resolution, which is a reasonable assumption if both detectors are the same material, then a reduced equation leads to the total angular uncertainty from spatial uncertainty [Ord99].

$$\Delta\theta_{spl} = \sqrt{\frac{(\Delta r)^2}{R_2^2} + \frac{(\Delta r)^2}{R_1^2}\left[1 + \frac{R_1^2}{R_2^2} + 2\frac{R_1}{R_2}\cos\theta\right]} \tag{6.4}$$

where, $\Delta\theta_{spl}$ is the angular uncertainty resulting from spatial uncertainty, R_2 is the scattering site – absorption site separation, R_1 is the source-scattering site separation and θ is the scattering angle. The interpretation of the geometrical effect of R_2 on the angular uncertainty resulting from spatial resolution, is that $\Delta\theta_{spl}$ is effectively inversely proportional to the interaction separation, R_2. Therefore, a greater scattering-absorber separation gives a greater angular resolution. The effect of R_1 is not so apparent but angular resolution is reported to improve for sources very close to the scattering detector [Ord99]. Assuming that one detector had infinite spatial resolution whilst the other did not, it is easily concluded that spatial resolution in the scattering detector affects both the cone orientation and vertex, whilst the absorber detector affects only the cone direction. Fig. 6.2 shows $\Delta\theta_{spl}$ for number of spatial resolutions at a fixed geometry ($R_1 = R_2 = 50\text{mm}$). This figure clearly shows the dependency of $\Delta\theta_{spl}$ on the spatial resolution of the camera.

The total angular uncertainty is then given as the quadrature sum of the angular uncertainties introduced by energy and spatial uncertainties.

$$\Delta\theta = \sqrt{\left(\Delta\theta_{spl}\right)^2 + \left(\Delta\theta_{E_i}\right)^2} \tag{6.5}$$

Angular uncertainty is a function of energy and spatial resolution. Both of these properties have been shown to be limited by intrinsic and practical factors. The geometrically free parameters that can be manipulated to optimise a Compton camera are the detector separations, the source-absorber separation and the scattering angle. However, maintaining efficiency for large detector separations is prohibitively expensive and a compromise is required. The source is easily moved relative to the scattering detector and scattering angle can be gated in software. Other than taking these simple steps, the angular uncertainty cannot be reduced unless a different detector material is utilised.

6.2.3 Reconstruction Algorithms

Energy depositions and interaction sites are used to construct cones that are projected out into space. A static plane at a fixed distance from the centre of the absorbed detector is effectively used as a projection screen, on which multiple cones are projected. Cones that intersect on this plane yield conic surfaces which represent integration paths. The conic integration paths will be composed of ellipses, parabolas and hyperbolas. If the source is located on a central axis of the Compton camera that is normal to the centre of the absorber detector, and the projection plane is located through the source, then the conic intersections are considered as a number of intersecting straight lines provided that the integration path is small. Similarities with conventional tomography can be drawn at this stage and techniques for straight-ray transaxial tomography can be applied. This is justified by ultrasound reflective tomography which back-projects signals over elliptical paths but uses straight-ray reconstruction techniques [Nor79], although the paths of integration which include parabolic and hyperbolic paths are more complex than for ultrasound.

The term *laminogram* is used to describe a source reconstruction provided by a number of intersecting lines. This produces a rough estimate of the source distribution and intensity. Image reconstruction codes which do not apply any further mathematical analysis at this point are referred to as analytical back projection codes. An example of a single slice from a simple back projection code is shown in Fig. 6.3. This image shows a number of intersecting conics and was produced with simulated data (appendix A). Codes which do apply mathematical analysis are referred to as filtered or iterative, depending on the utilised mathematics. Laminograms suffer from blurring arising from false intersections close to the actual source location. This blurring has a $1/r$ form and can be filtered in the frequency domain by a fixed resolution filter and a Fourier transform.

$$\Lambda_\phi(\xi_r) = \int_{-\infty}^{\infty} \lambda_\phi(x_r) e^{-j2\pi\xi_r x_r} dx_r \tag{6.6}$$

where Λ_ϕ is the projection of the source intensity in the frequency domain related to the frequency ξ, λ_ϕ is the intensity function representing the source distribution and the exponential term is the filtering function. The subscript r is simply representative of a

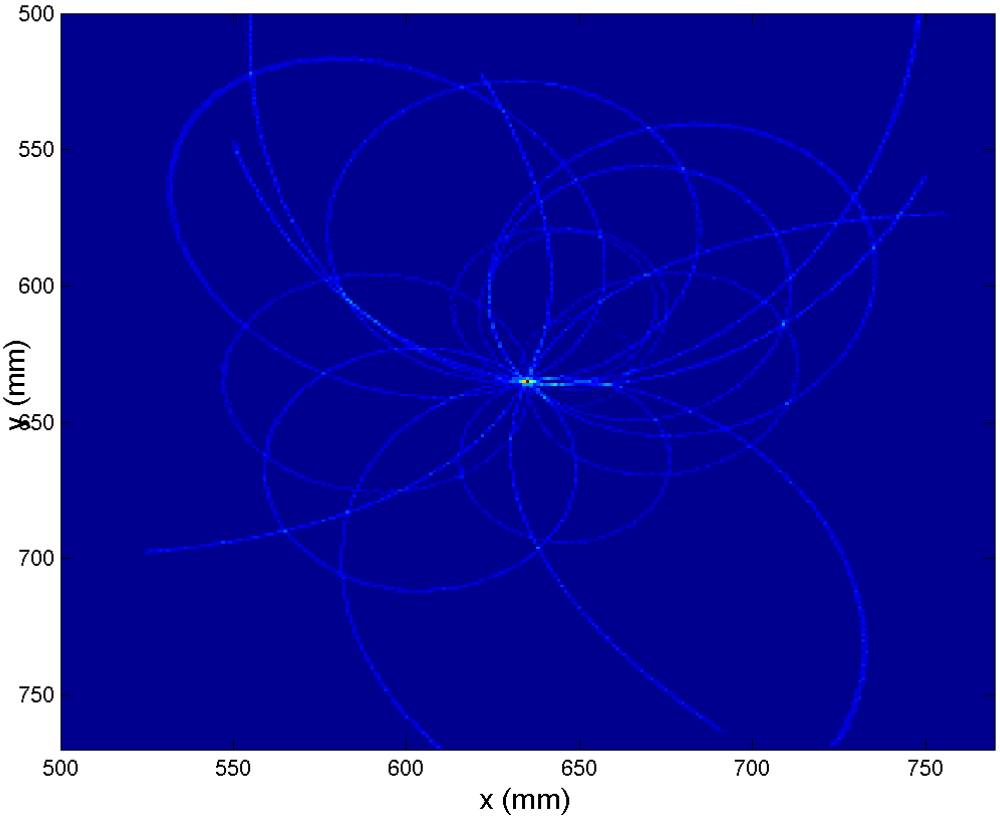

Figure 6.3: A number of cones constructed from simulated data (appendix A). The source was located at (635,635) and the cones do indeed intersect at this coordinate thus reconstructing the source. The intersecting conics can be considered as straight lines close to the source. As intersecting lines approach each other they actually intersect prematurely and the reconstructed source has a 1/r blurring. An important point to stress is that false point sources will always be reconstructed by cones that intersect at arbitrary coordinates.

rotation of the x and y axis about an angle ϕ, which is necessary to produce slices for a tomography image and simulates the rotation of the camera. Equ. 6.6 is mathematically identical to Equ. 5.1. Imaging codes which use Equ. 6.6 are exclusively known as filtered back projection (FBP) codes.

Other imaging techniques take a statistical iterative approach and are more computationally intensive. An example is the ART reconstruction algorithm (section 6.1) which starts with an initial estimate of the image (based on system parameters: noise, etc), projects the estimate onto a hyperplane (the actual projection), and compares the difference between the initial estimate and the actual image. The image is then updated based upon the difference between the estimated and the actual projections. This is performed in succession for a set number of iterations. The benefits of using this technique are good quality images and low noise. Gillam [Gil07] has used a maximum likelihood estimator (MLE) algorithm described by

Wilderman for SmartPET Compton image reconstructions, which is also an iterative technique. Effects of finite resolution were approximated by back projecting a central cone for mean scattering angle and two neighbouring cones with Gaussian-weighted amplitude. Hence this reconstruction weights the back-projected central cone with the sum of 2 Gaussians that approximates the true angular uncertainty.

6.3 Imaging Code Development

The most commonly used coordinate system for a Compton camera is the Spherical coordinate system because the conics can be drawn directly onto the projection plane. This spares precious memory addresses or increases the discretisation of the conics on the projection plane so that their representation approaches that of a continuous line. However, for the purposes of simplicity it was decided that a Cartesian coordinate system would be developed in this thesis. This decision was based on the memory resource requirements of building a three-dimensional world in computer RAM against the total RAM available on a 726MB laptop; which is sufficiently adequate.

6.3.1 General Equation of a Cone

Compton camera imaging is based principally on intersecting cones. Each cone is defined by an apex, opening angle, axis and a base. The axis is perpendicular to the base plane and there is rotational symmetry about the axis. In this particular case a circle is projected onto the base plane, however, if a new plane intersects the cone at an arbitrary angle to the axis, then a conic is projected onto this new plane. Conic surfaces can be categorised according to their eccentricity. Surfaces categorised as hyperbolic are usually disregarded for imaging because, by definition, the cone axis does not intersect the 'projection' plane, implying a rather large opening angle or that the source does not reside on the plane and is therefore discarded in the analysis. The general equation of a cone has been used to construct cones in MATLAB and is given in the form:

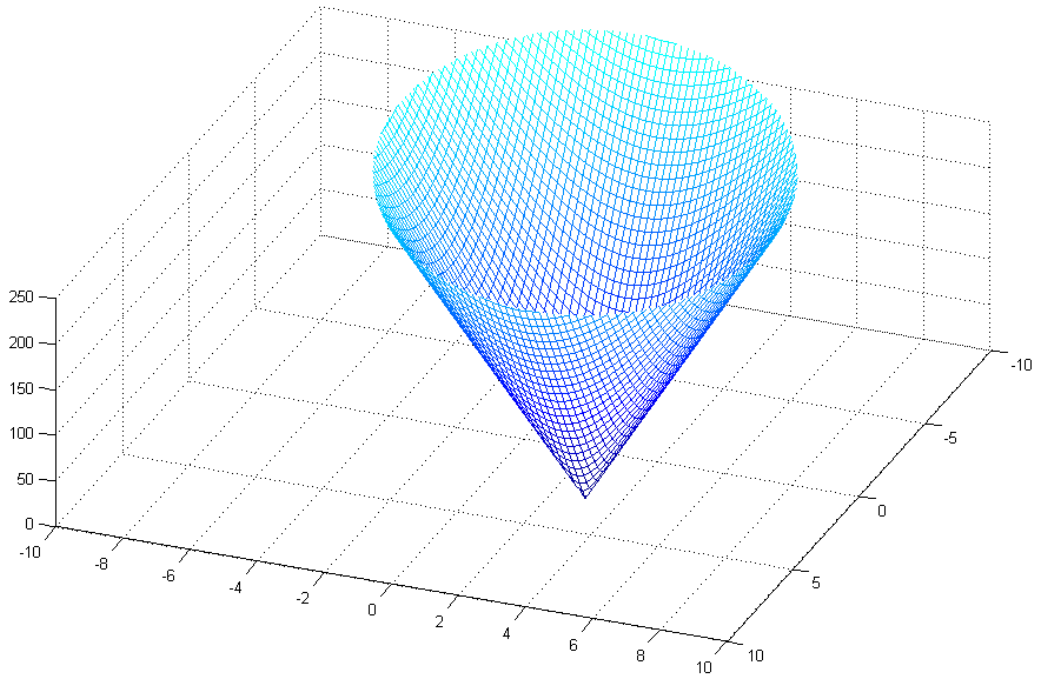

Figure 6.4: An example cone that has the z axis as the cone axis and its apex at (3,4,5) with an opening angle of 1.5°. The problem of conic discretisation can clearly be seen by the discrete mesh grid. So that two intersecting cones may not technically intersect on a projection plane in software.

$$\frac{(x-x_0)^2+(y-y_0)^2}{\left[\tan\left(\frac{\theta}{2}\right)\right]^2}=(z-z_0)^2 \tag{6.7}$$

where, x, y and z are Cartesian coordinates or a single point on the cone. x_0, y_0 and z_0 describe the coordinate of the apex given by the interaction site in the absorbing detector. θ is the opening angle of the cone which is determined by the energy depositions in the Compton camera. Simplifying this equation in terms of a single variable will result in an equation of the second degree, which once solved results in two eigenvalues. The cone is then a function of two variables that has two solutions for each unique coordinate. Two cones are now defined with a common axis, otherwise known as a double cone, so that each cone has a common apex. The cones are symmetric about a plane perpendicular to the cone axis and taking the absolute eigenvalue removes the ambiguity of the cone direction. Solving Equ. 6.7 for a single variable clearly restricts the cone axis to be co-directional with that particular axis, provided that all variables are eigenvalues of orthonormal eigenvectors. A mesh grid with two dimensions can be created in MATLAB allowing the solution of each individual coordinate to be calculated. An example cone with the z axis selected as the cone axis is shown in Fig. 6.4.

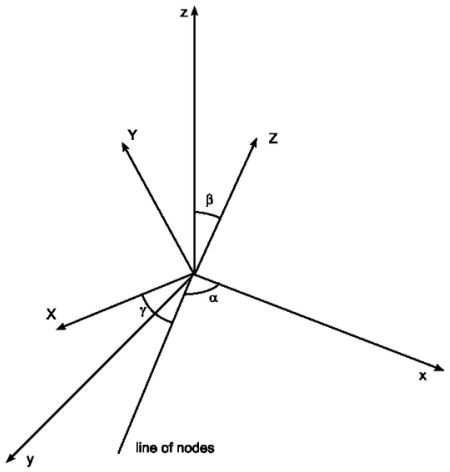

Figure 6.5: A frame space rotation that maintains orthogonality (x -> X), (y->Y) and (z->Z). This requires Euler angles which are shown (α, β, γ).

6.3.2 Transformation Matrix

Energy information can be directly translated into the opening angle of a cone generated with Equ. 6.7. However, this cone does not *per se* completely represent the interaction. The cone still requires information from both extracted interaction sites to be translated into a direction-vector to create an off-axis cone. This rotation is achieved with knowledge of basic linear algebra and a transformation matrix. The Cartesian coordinate system is simply described by three mutually-perpendicular unit vectors so that the cross product of any two unit vectors results in the third unit vector. The z direction unit vector can be rotated to be co-directional with the direction vector calculated from the two interaction sites. To maintain the definition of a Cartesian coordinate system, both the x and y direction unit vectors must also be rotated so that the cross product of any two unit vectors results in the third. Euler angles are used to satisfy this condition and the transform is relatively simple. Fig. 6.5 shows how a Cartesian coordinate system can be rotated so that the new axes maintain orthogonality. Majuscules indicate the new frame of the coordinate space in Fig. 6.5 and the angles α, β and γ represent the new spatial orientation in reference to the original frame as indicated by lower case. The transform matrix is then given by: (6.8)

$$\begin{bmatrix} x' \\ y' \\ z' \end{bmatrix} = \begin{bmatrix} \cos\beta\cos\gamma & \sin\alpha\sin\beta\cos\gamma + \cos\alpha\sin\gamma & -\cos\alpha\sin\beta\cos\gamma + \sin\alpha\sin\gamma \\ -\cos\beta\sin\gamma & -\sin\alpha\sin\beta sin\gamma + \cos\alpha\cos\gamma & \cos\alpha\sin\beta\sin\gamma + \sin\alpha\cos\gamma \\ \sin\beta & -\sin\alpha\cos\beta & \cos\alpha\cos\beta \end{bmatrix} \begin{bmatrix} x \\ y \\ z \end{bmatrix}$$

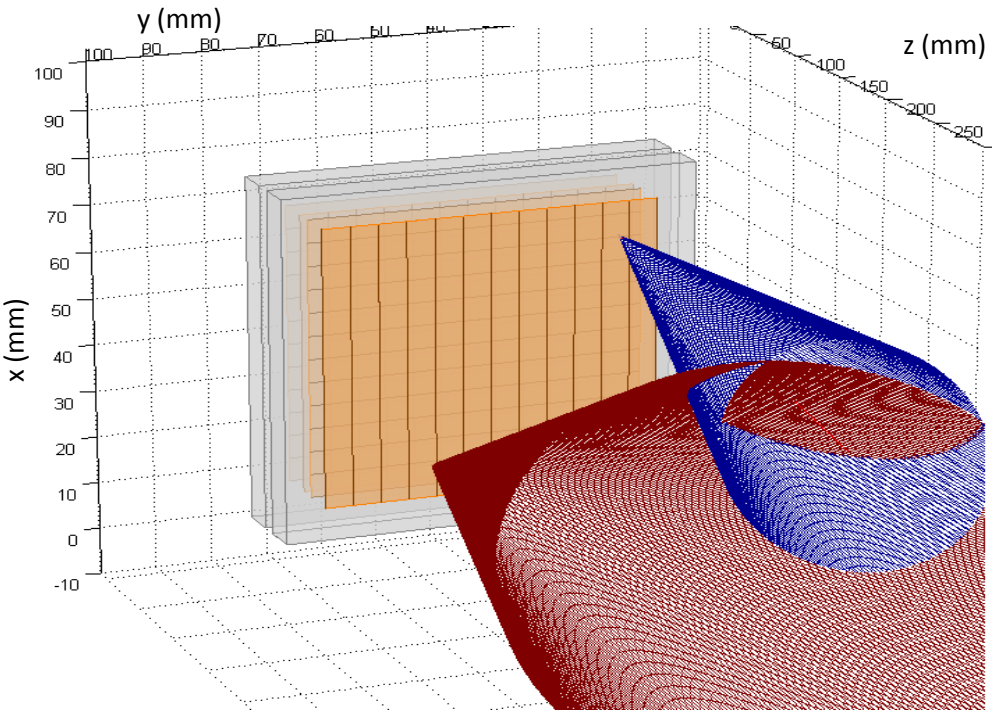

Figure 6.6: An example of two rotated cones which intersect along the z axis. There is clearly a range of z values for which intersections occur creating a problem if the source location along the z axis is unknown.

where the primes indicate the new coordinates of a rotated cone. A bespoke back projection code can now be designed for SmartPET as a simple collection of functions and scripts. Each event that passes the criterion of a coincidence in SP1 and SP2, fold 1 in both detectors, and an add-back to the source energy has a cone constructed. The apex is given by the interaction in SP2, the angle is given by the energy depositions and the cone axis is given by the vector that joins both interaction sites. When new cone coordinates are calculated these are projected into the original reference frame, therefore all cones can be compared in the same space. Fig. 6.6 displays two example cones that have been rotated and projected onto the same reference space. These cones result from real interactions in SP1 and SP2. They clearly intersect and the final part of the imaging code is to project this intersection onto a 'projection' plane. The discrete nature of the cones requires a frustum to be defined over a specified range along the z axis. This would clearly affects the resolution of the image and it is desirable that only a very narrow frustum is defined.

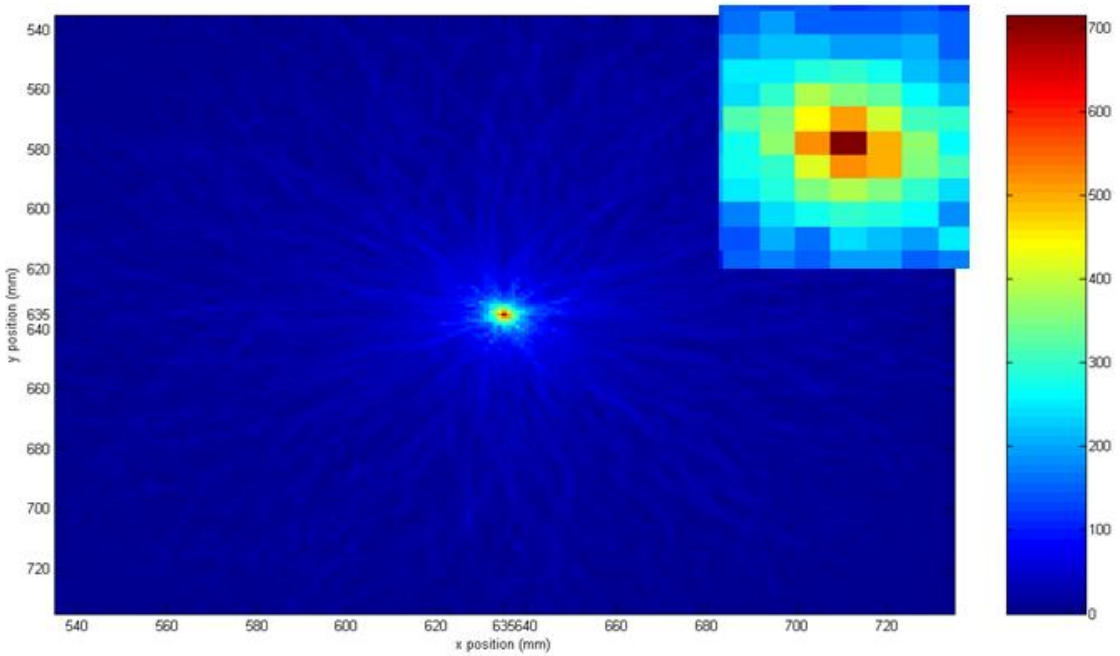

Figure 6.7: Back projection of ^{137}Cs point from simulated data. The spatial resolution is simulated as sub millimetre and the energy resolution is exact, representing ideal imaging conditions. 1/r blurring is clearly seen.

6.3.3 Validation with Simulated Data

The simple back-projection code requires validation with simulated data. The simulation was performed with Geant4 and is presented in appendix A. A single ^{137}Cs point source was simulated and interaction sites were defined with sub-millimetre spatial resolution, representing ideal imaging conditions. The reconstruction is presented in Fig. 6.7 and all scattering angles were utilised. A point source was indeed reconstructed indicating the defined cones are correctly rotated. The mesh grid used in MATLAB was specified in 1 millimetre increments and therefore the best possible image resolution for the simulated data is 1mm FWHM. Reassuringly, the most intense pixel in the image does only cover 1mm^2. However, a salient feature in the figure is the 1/r blurring due to false intersecting lines close to the true source location. This is a good example for the need to apply a filter to the back projected image. The axes in Fig. 6.7 begin at 535mm due to a technicality for which all cone coordinates need to be positive; 600mm was added to all cone x and y coordinates so that the coordinate (600,600) is the bottom corner of the Compton camera and (635,635) which is the source is located on the x and y coordinates of the camera axis.

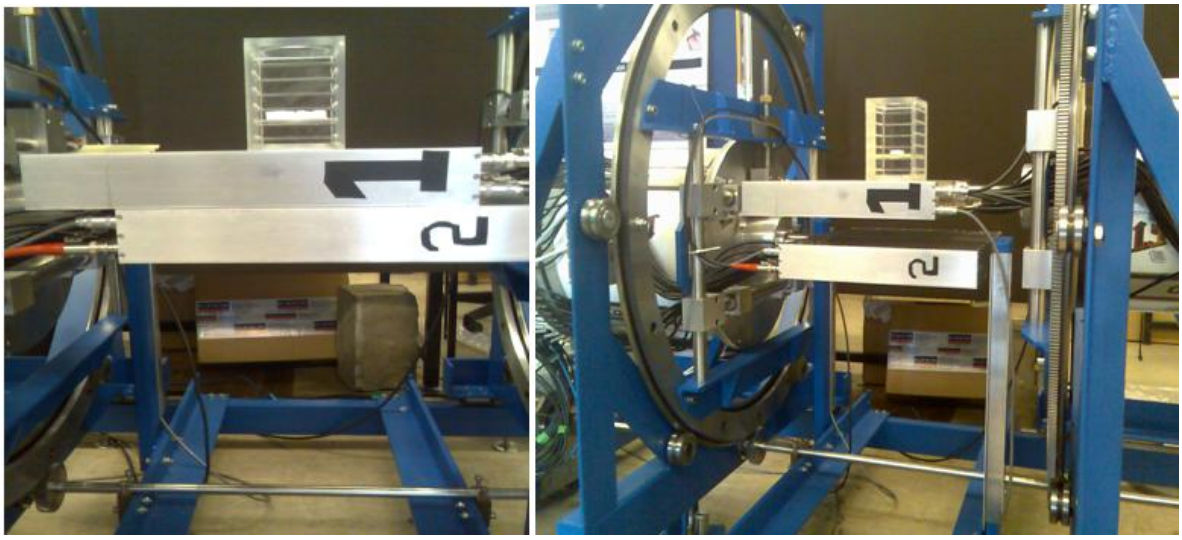

Figure 6.8: SmartPET detectors in Compton camera configuration. SP1 was the scattering detector and SP2 was the absorber. A point source and a line source were both imaged 50mm from the cryostat of SP1. The effect of crystal separation was also investigated with the cryostats abutting (image a) and separated (image b).

6.4 Experimental Imaging

Two radioactive sources have been imaged experimentally with the SmartPET system. These sources were a ^{137}Cs point source and a ^{22}Na line source. The point source was chosen for the purposes of a comparison with the simulation. The rotating gantry, locked in a horizontal position, was used to hold the detectors in an appropriate geometry. Attempts were made to investigate the angular resolution as a function of crystal separation. The experimental configuration can be seen in Fig. 6.8. Both sources were positioned 50mm from the front face of the cryostat of SP1. SP1 acted as the scattering detector and SP2 acted as the absorbing detector. Data acquisition was performed with the GRT4 cards, and the trigger system described in section 3.5 was adjusted so that a trigger signal was received when SP1 and SP2 triggered in coincidence.

There was one notable difference between this experiment and the experiment in chapter 3. The GRT4 cards were adjusted for higher accepted trigger rates due to a PET experiment that ran between the work in chapter 3 and this current work. The only way to achieve a higher trigger acceptance was to cut the number of samples in each signal from 256 to 128, thus doubling the DAQ throughput. However, this now prevents a direct application of all of the C functions that have been developed in the previous chapters. The basis data set (section 4.6.1) for depth determination requires an adjustment from 1250 samples to 610

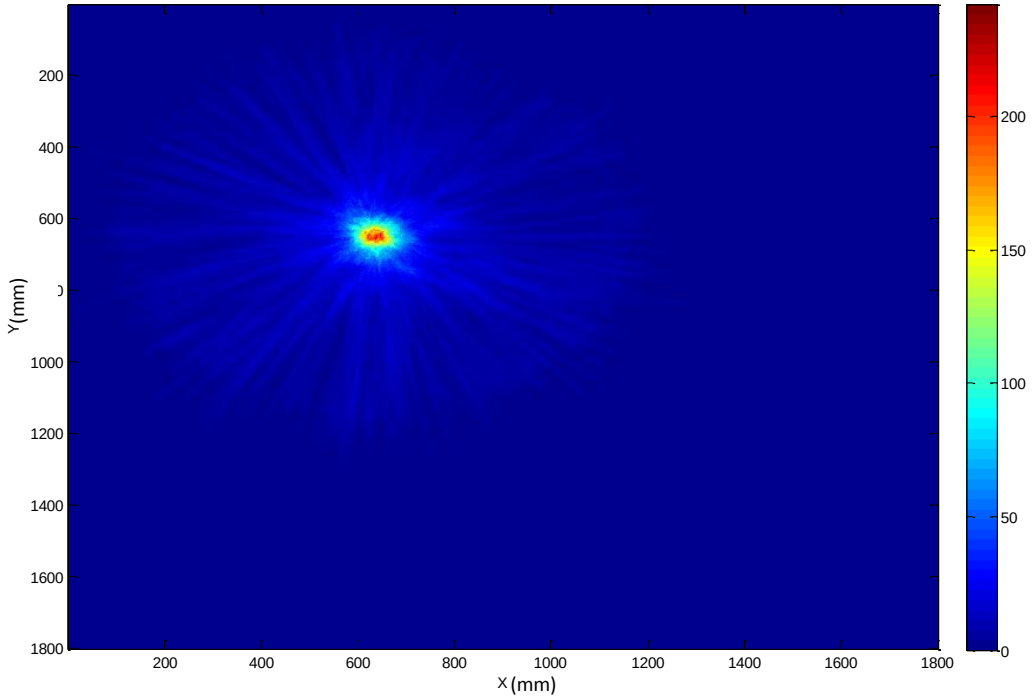

Figure 6.9: Reconstructed ^{137}Cs point source located 50mm in front SP1's cryostat. The number of events used was 2500 and the FWHM of the point source is 54.3mm.

samples. This is not a challenging proposition because the rise time is unaffected (12.5ns per division on the leading edge), but it is does require a well established C code to be rewritten. The principle of a basis data set has been demonstrated, and it is perhaps more profitable to spend the time required to adjust the prototype basis data set developing new bespoke basis data sets for SP1 and SP2. DiCS now also fails to operate as expected because the dyadic grid used in chapter 5 is no longer appropriate. The transformation of a 128 sample signal requires thorough investigation or alternatively the signal requires an extension to 256 elements. However, simple parametric PSA can still be applied.

6.4.1 ^{137}Cs Point Source

A ^{137}Cs point source was positioned 50mm, along the central axis of the Compton camera, from the cryostat of SP1 as shown in Fig. 6.8. The crystals of SP1 and SP2 were brought together as close as possible so that the cryostats were touching. The reconstructed point source is shown in Fig. 6.9. All events that were fold 1 in both detectors and add-back to 662keV were included in the reconstruction; this was a total of 2500 events. No gates on the

scattering angle were applied. Simple parametric PSA was applied to all useable events with both the transient induced charges and real charges contributing to the determination of interaction location. There are no significant variations between SP1 and SP2 which would require the adjustment of simple PSA between the detectors. Simple PSA is based on a distribution of parameters over the active volume dimensions. Similar distributions were seen in both detectors and it was then simply assumed that the PSA developed for SP1 was transferable to SP2.

Basic analysis of Fig. 6.9 reveals that the FWHM of the reconstructed point source is 54.3mm which represents poor image resolution. A problem with the imaging code was initially thought to be responsible for this poor resolution. However, the code was retested and does indeed work, as demonstrated by a reconstructed point source and validation with simulated data. Other inherent factors which can degrade the image are energy and spatial resolution. Energy resolution is assumed to be optimised and spatial resolution is assumed greater than the raw granularities. A comparison with simulated reconstructions (appendix A) reveals that Fig. 6.9 actually represents a Gaussian spatial resolution with a standard deviation of $1.5\text{mm} < \sigma < 2\text{mm}$. This deduction is based on comparisons of the FWHM values and a simple inspection of Fig. A.3, which displays image intensity as a function of spatial resolution. Furthermore, comparisons with advanced imaging [Gil07] show that this FWHM is of the order of magnitude expected from such a simple code. Filtered back projection of a ^{152}Eu (1408keV) point source using a spherical-based code resulted in a FWHM of $\sim$12mm. The detector cryostats were 30mm apart, the source was 30mm in front of the camera, and the data were filtered and properly sequenced. Therefore, in consideration to the different camera configurations, energies and data filtering, it is anticipated that Fig. 6.9 should show a worse image resolution. In reference to the preceding sections, it is also considered that Fig. 6.9 represents the worst case scenario. Improvements, which are discussed in the next chapter, should be used to improve image quality.

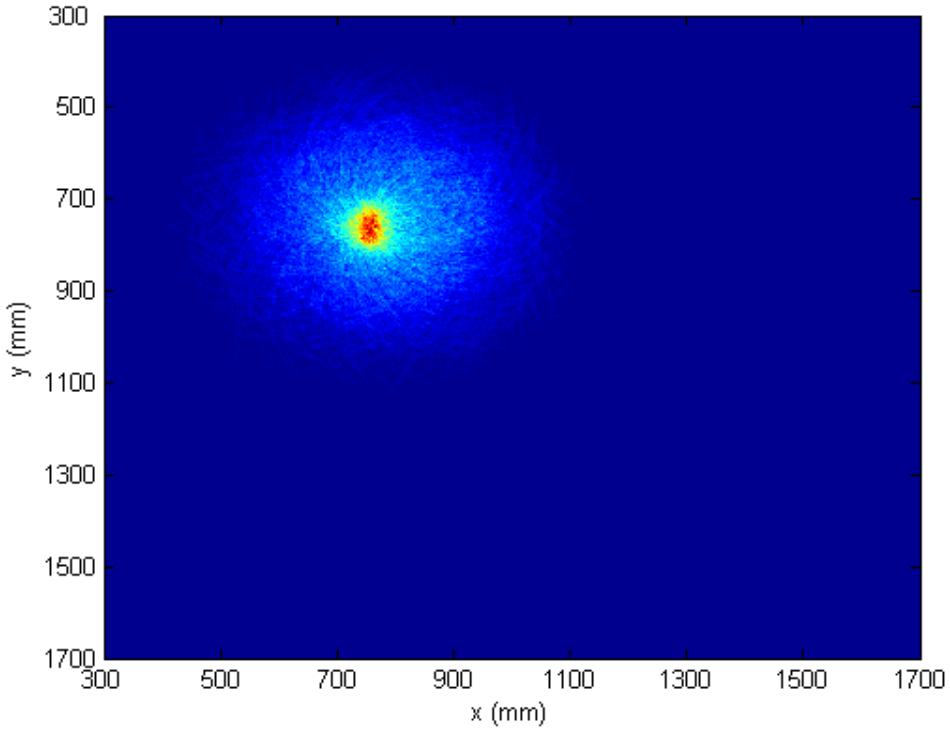

Figure 6.10: Reconstructed ^{137}Cs point source located 50mm in front SP1's cryostat. The number of events used was 2500 and the FWHM of the point source is 54.3mm.

6.4.2 ^{22}Na Line Source

Two experimental runs that utilised a ^{22}Na line source (7.5cm long cylinder of 2mm radius filled with liquid ^{22}Na) were planned and executed. These were to test the effects of introducing gates on the scattering angle and the effects of crystal separation. However, once the data were sorted off-line it was found that one of the runs had suffered a failure in DAQ and a number of SP2 DC electrodes failed to record data. Loose cables were found to be the cause and the problem was fixed. Unfortunately, the DAQ was then required for another project and data for crystal separation were not acquired. The resulting image for the minimum detector separation is shown in Fig. 6.10. This image has been reproduced (but not shown) with various scattering angular-acceptances resulting in imperceptible variations. Therefore, it can be concluded that gating on the scattering angle is not the dominant effect in this image. The factors which govern performance of line source imaging are clearly not well understood. Therefore the line source image is included for completeness but not for interpretation. No measure of the spatial resolution is possible because there are no simulations to justify the conclusion. The line source would also appear to be a further step in complexity. The 1275keV line was used for imaging and by

inspection it can be seen that the response does not appear to be significantly different than that for Fig. 6.9. However, one key attribute in Fig. 6.10 does indeed indicate that this image resulted from a distributed line source. Consider the artefacts that result from cones intersecting close to a point source (Fig. 6.9 and Fig. 6.7). These reconstructed lines do not appear in Fig. 6.10, indicating that a point source is not present in Fig. 6.10. The cones actually appear to intersect randomly over a large area, therefore indicating a large number of point sources located about a central position.

Chapter 7

Conclusions and Recommendations for Future Work

A full and thorough description of a Compton camera that is based upon the SmartPET detectors and electronics has been given, including a justification of the detector materials. Techniques for improving the spatial resolution of the detectors over that provided by the raw granularity have been tested and an experimental basis data set has been developed. A novel technique based on modern digital signal processing has also been investigated and tested with real data. The work performed for this thesis ultimately resulted in images of radioisotopes being produced. A summary of the thesis is presented in this chapter which highlights salient issues and is accompanied by suggestions for the future direction of the SmartPET project.

7.1 Summary

The first chapter was used to introduce the aims and objectives of the research in this thesis, namely to produce an image of a radioisotope without mechanical collimators, which was subsequently achieved. Radiation detection was presented in the second chapter with an emphasis on detection material and practical considerations. Energy resolution was seen to be an intrinsic property of the detector material whilst spatial resolution could be optimised with utilisation of the weighting field concept. Pulse shape analysis was

introduced and a coincidence experiment was devised in the third chapter to generate data that could test the suitability of pulse shape analysis.

Analysis of the coincidence experiment was presented in chapter 4, and work was performed to increase spatial resolution towards the spatial limitations based on the momentum of the recoil electron. It was found that signal pre-processing is a necessity prior to true signal analysis, and that this pre-processing is restricted by the lack of knowledge of t_0. It was proposed that t_0 can be estimated by summing all signals from a single event to average out the noise. It was also found that by performing detector characterisation with a coincidence scan, which incorporated germanium auxiliary detectors, that multiple scatters in the primary crystal could be removed from the data. Therefore, the integrity of characterisation data was increased.

Analysis of the high-quality data in chapter 4 resulted in an excellent agreement with previous work; once the systematic errors of crystal alignment were considered. This unexpected result immediately drew the conclusion that *rise times* are a function of depth and independent of energy deposition. However, more significant conclusions were drawn assuming that the work presented in this thesis is free from Compton scattering. The excellent agreement would then appear to indicate that the previous work was also free from Compton scattering or that scattering had a negligible effect. Therefore it was concluded that particular scattering events cannot be resolved. The terms *in-line* and *in-plane* were introduced to classify scattering according to whether it can be identified or not identified in a SmartPET detector. Additionally, the narrow distribution of *rise times* would indicate that the warping of the electric field is not highly significant in the active region. Albeit there is a low-level broadening which could realistically result from a small effect of electric field warping, but this was insignificant and subsequently neglected. Therefore, only 20 signals realistically need simulating to describe real charge detector response through depth.

It was also found in chapter 4 that the asymmetry parameter is insensitive in the bi-polar region. This region realistically covers 2mm through depth and results in small asymmetry parameters. However, the majority of the crystal depth does indeed result in a reliable asymmetry parameter. Additionally, it was concluded that the asymmetry parameter is also

energy-independent. With overall good agreement with the secondary collimated scan, it was concluded in chapter 4 that simply parametric PSA is suitable to increase the spatial resolution of SP1.

The basis data set has been tested and proved capable of providing 1.9mm (FWHM) position resolution. Some strange artefacts are seen for positions determined outside of the crystal, but the number of counts is small and it is thought that these could be scattering events. The development of a partial experimental basis data set represents a movement away from simple PSA. The calculated FWHM also fails to truly represent the true attainable spatial resolution because the beam is greater than 1mm wide within the crystal. Therefore, holding the collimator static and determining interaction locations would always result in a distribution wider than 1mm. The best possible test of position resolution is thought to be the effect on the final images. Finally, it was demonstrated that multiple interactions occurring far enough apart can be treated as individual interactions and sequenced with the Klein-Nishina relationship.

A discrete wavelet transform can be used to transform detector signals and then reconstruct these signals. The reconstruction is not exact but is an approximation. Wavelet analysis can therefore be used to clean the signals, but this is computationally intensive and slow. Perhaps more significantly it can be used to identify *in-line* multiple interactions in closed-face-pixels, which is considerably faster. Cleaned signals are only representations and these representations have been shown to be similar to the real signal. It is then not surprising that parametric PSA is not improved by the application of wavelet analysis. Results for 662keV are reliable but the transient-induced charges for low-energy interactions are not reliable. Wavelet analysis can be used for detectors which do not have simulations or basis-data-sets as a quick method of rejecting scattering events.

The SmartPET system has been shown capable of producing Compton camera images utilising simple back projection methods. These codes resulted in rather poor image quality but demonstrated that simple PSA produced good spatial resolution. It is worth noting that configuration of the free variables of the Compton camera and the reconstruction algorithm represented the absolute worst case scenario. Indeed, far greater image quality has recently

been produced using more advanced volumetric and iterative imaging codes with an optimised system proving that SmartPET is a valid Compton camera.

7.2 Future Directions

This thesis represents the beginning of Compton camera imaging at Liverpool. The SmartPET system has been shown to be capable of performing Compton camera imaging. However, the system in this thesis does not represent an optimised system and there are a number of important suggestions to make that may increase performance. These suggestions can be split into spatial resolution and camera optimisation.

The best position spatial resolution is clearly critical and although parametric PSA increases raw granularity, other techniques offer more attractive alternatives. The experimental basis-data-set performed beyond expectations and has yet to be fully tested. A narrower primary collimator beam could be employed and reconstructed with the basis-data-set. Indeed, a narrower beam could be used to build a newer basis-data-set. An experimental basis-data-set could also be constructed for the transient-induced charges. This would require secondary collimation. A number of factors hampered the secondary collimated scan, partly due to time restrictions but also due to human error. It would be wise to determine the primary collimator x-y static time by the number of statistics collected at that particular location and avoid using a universal static time. This would require sophisticated online analysis programs but these could be incorporated into industry-standard packages (MATLAB or LabVIEW) to remove function redundancy. This would then also decrease the final analysis time. It is also highly-advisable that a greater number of positions should be scanned with secondary collimators. A full electric field simulation is an alternative, but this would require validation with secondary collimated data.

One of the problems encountered whilst imaging and which was common to the coincidence measurements were the time restrictions. This problem arises from a lack of DAQ, and dedicated electronics are necessary. These are now currently available and are being tested, but using these with the SmartPET detectors as quickly as possible is a priority. The system itself needs optimising as does the image reconstruction code. Concentrating on

the system, it is suggested that this is modelled in Geant4 and optimised according to the factors presented in chapter 6. An imaging code could then be written which would represent the best possible code. Filtered back projection is clearly an improvement over simple back projection. It is advised that filtered back projection is used as a minimum for imaging. However, even greater improvements are possible with iterative reconstruction algorithms. The predictions of optimal system performance can be used as a benchmark for experimental imaging. This would also serve as a good test of the spatial resolution of the camera. It would be advisable to concentrate on a point source image and understand the performance factors before imaging a line source. Several attempts were made to image a line source but this ultimately proved a complex issue with dynamic factors. Other factors such as radioisotope and scattering detector material can then be addressed. The overwhelming majority of clinical planar and SPECT studies use Tc-99m. This is due to its inexpensiveness, availability and easy containment. A silicon scattering detector is necessary if such low energies are to be imaged.

Digital Compton Suppression (DiCS) is a technique which has proved to be powerful and open to optimisation. The wavelet function is not currently a bespoke design for SmartPET, but it could indeed be specially designed to form an orthogonal basis of vectors which extract maximum energy from the signals of interest. Once signals are identified as scattered they are rejected. However, if the interactions are well separated in depth then the 'individual' transforms are also well separated and the transform heights are then related to energy deposition if a single depth of interaction can be determined. It may also be fruitful to attempt a de-convolution based on predicted transform shapes, matching a library of predicted shapes against a single transform. The signals would only require alignment about a single maximum and this should be a fast process involving only 20 signals, in addition to another 19 to de-convolve the other interaction. Wavelet analysis will also benefit from faster DAQ operating over a large bit range. In-plane scatters would show a larger discontinuity and identification would be more probable. The project is evolving and it will be interesting to follow its progress in the future.

Appendix A

Geant4 Simulations

The SmartPET detectors have been simulated in Compton camera configuration to provide test data for the imaging code of chapter 6, and to provide a measure of image quality for a range of theoretical, detector, spatial resolutions. The simulation code is an amalgamation of two Geant4 codes provided by two SmartPET project collaborators who have subsequently left the project[4]. I would like to thank both collaborators for excellent advice; both work related and not.

A.1 Geant 4

Geant4 is a radiation transport code written in C++ and containing an abundant set of physics models in an array of user classes. Specific applications are built by choosing the appropriate user classes for the required simulation. The user has complete control over all aspects of the simulation from geometry, particles of interest, physics processes to the response of sensitive detector components. There are three types of user; an end user, application programmer and a framework provider. The work presented in this appendix is the result of an end users' work. The end user specifies the geometry, particles of interest, number of events, particle tracking and controls the simulation by varying the run time parameters. These parameters can be specified in the main program (C++) and ran automatically, or from an interactive terminal using batch mode. The former option of

[4]These were Majid Farahmand, formerly from the Liverpool group, and Toby Beverage who worked as a collaborator from Monash University, Melbourne.

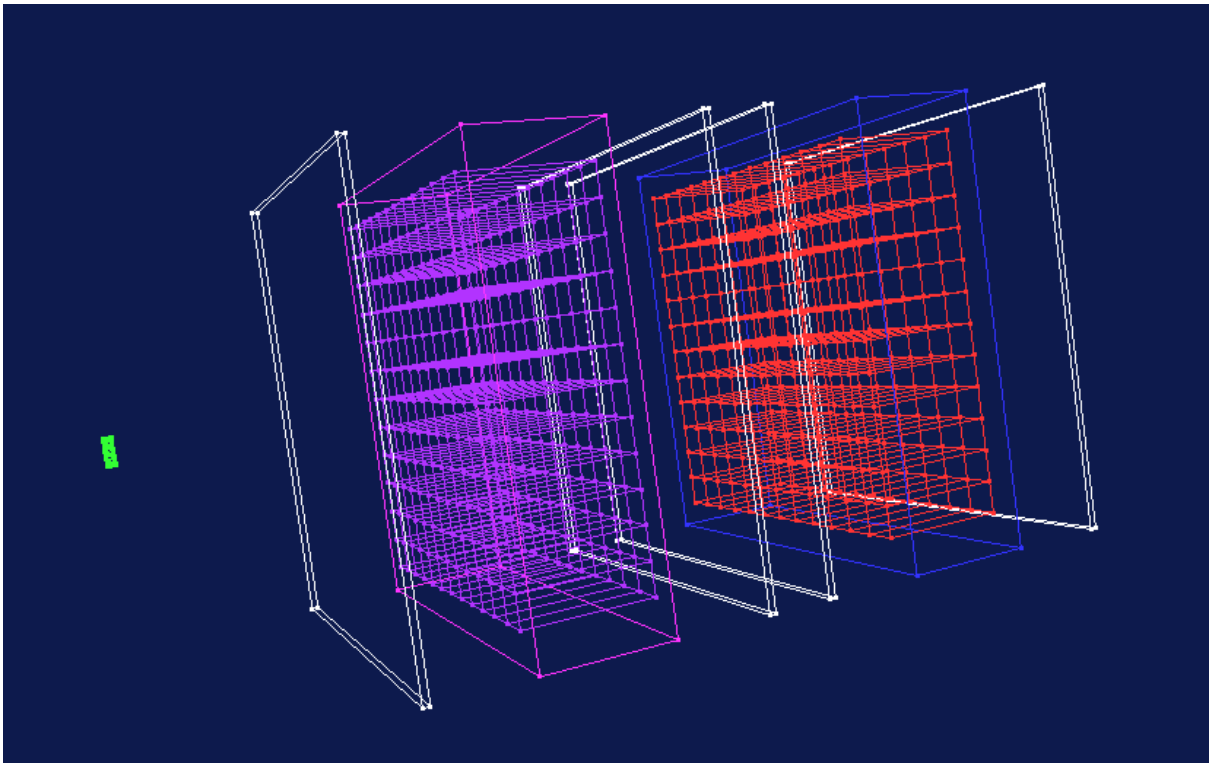

Figure A.1: Visualisation representing the geometry of simulations. The source is shown in green, SP2 in purple, SP1 in red and the aluminium window in white. Segmentation is achieved by the arrangement of individual logical volume (Ge) towers (courtesy of M. Farahmand).

specifying the parameters has been used in this appendix.

A.2 Simulation

A ^{137}Cs point source was simulated 50mm from the front face of the aluminium window on the cryostat of SP2. The cryostat is included in the simulation and both detector cryostats sat tightly together. Therefore, the total crystal separation was 30mm. The simulation world was established so that a line parallel to the z axis can intersect the source, SP1 and SP2. The world started at z = 0mm and ended at z = 150mm. The source sat in front of SP2 so that SP2 was the scattering detector and SP1 was the absorbing detector. Geant4 places the centre of any cube at the origin by default. This was modified in the z axis so that two detectors could sit in unique locations. However, the x and y locations were not modified so that the camera axis ran parallel to the z axis and intersected x = 0mm, y = 0mm. The source was positioned on the camera axis. The detectors were constructed using a total logical volume of 74x74x20mm, segmented into pixels of (5x5x20)mm^3 and filled with a material that had the following physical properties:

- 72.61g/mole
- 70kelvin
- 5.32gcm^{-3}
- 350eV mean excitation energy
- 32 atomic number

The physical properties of the aluminium window were:

- 26.98g/mole
- 2.7gcm^{-3}
- 13 atomic number

The world was filled with a definition of air with the following physical properties:

- 1.29E-3g/mole
- 0.00129gcm^{-3}
- 70% N (Z = 7) 30% O (Z = 8)

A.3 Results

The results for the ^{137}Cs point source are primarily used to produce test data for the imaging code. However, it can also be used to deduce multiple hit patterns, single closed-face-pixel pixel interactions and separation through depth for multiple interactions in a single closed-face-pixel. An energy spectrum from the simulation is shown in Fig. A.2. This spectrum was produced from events that interact only once in each detector. Initial results indicate that 33% of events are composed of single interactions in both detectors. Whilst 16% of events are composed of multiple scatters in both detectors.

A.3.1 Effects of Position Resolution

Each simulated position was smeared by a Gaussian distribution to reproduce the effects of noise. The distribution had a mean of zero and the point source was imaged for a range of standard deviations, in 0.5mm increments, from 0-10.5mm. The resulting image

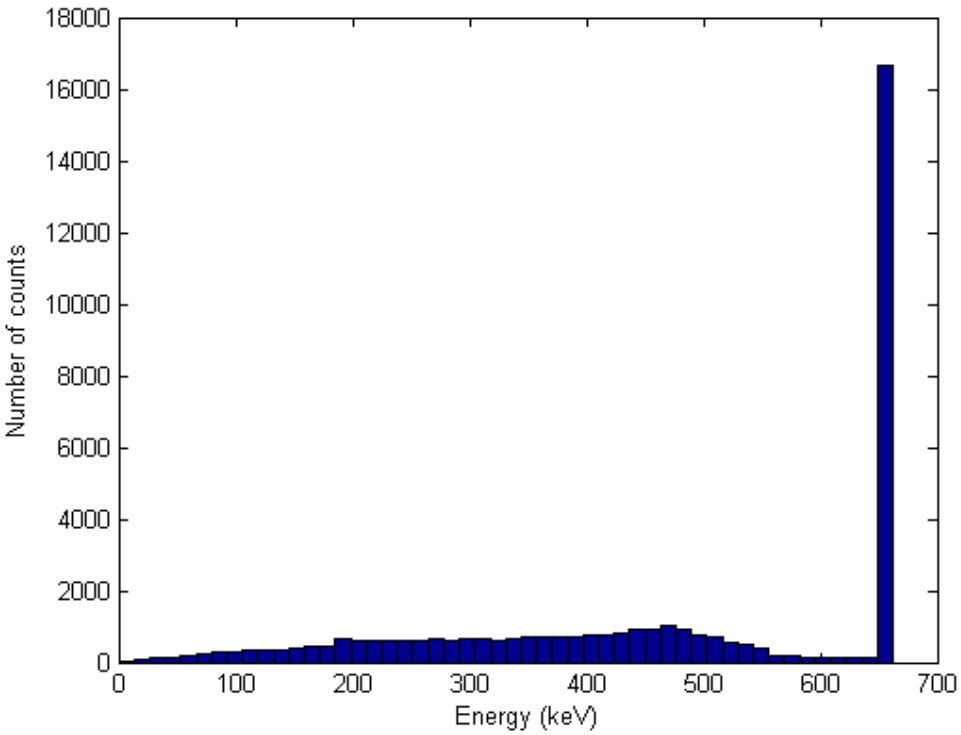

Figure A.2: Add-back spectra from both SP1 and SP2 detectors. Total energy from each event used, regardless of a single or multiple interaction event.

reconstructions are shown in Fig. A.3. All of the entries in each column in each image matrix were summed and the resulting values for each particular column were placed in a new array element indexed with the column number. This produced a new signal for each image from which the FWHM of the image could be calculated. Results are presented in table A.1. The FWHM with a standard deviation of 0 does not appear to tally with the image quality of Fig. A.3a, in which the majority of the point source populates 1-pixel. This can be partly explained by the method for which the FWHM is calculated. Each pixel surrounding the point source does indeed have a small contribution from the discrete precision of cone surfaces and plane intersections; only 756MB of RAM has been used to generate the images and therefore the cones are severely limited to a rather 'pixelated' world. To compensate for this the plane of intersection is not an infinitesimally thin plane but is a rather thick 1mm. Therefore, when the columns are summed, values which do not appear to affect image quality suddenly summate into a significant contribution. This 'error' then propagates through the range of standard deviation increments. And although the point is completely smeared in images with large standard deviations, when the columns are summed the point source is restored and the FWHM tangible. This would indicate that image quality is a rather

subjective science. However, some useful information can be gained from Tab. A.1. There is not a significant decrease in FWHM from 0-0.5mm standard deviation, but there is a significant decrease from 0.5-1mm, indicating that sub-millimetre position resolution is worth attempting, whilst it would not be profitable to push from 1.5mm standard deviation to only 1mm standard. The latter position resolution is the most probable target for imaging.

Standard Deviation	FWHM (mm)	Standard Deviation	FWHM (mm)
0	36	**5.5**	103.36
0.5	40	**6**	104.22
1	50.63	**6.5**	111.94
1.5	53.27	**7**	120.88
2	58.82	**7.5**	116.32
2.5	62.4	**8**	120.57
3	78.47	**8.5**	121.28
3.5	77.49	**9**	124.71
4	87	**9.5**	129.38
4.5	99.83	**10**	133.11
5	103.84	**10.5**	130.76

Table A.1: The FWHM values of the reconstructed point source for a number of detector spatial resolutions. The reconstructions are shown in Fig. A.3.

The image reconstructions that are presented in Fig. A.3 have been selected to illustrate how image quality varies as a function of detector spatial resolution. The standard deviation increments shown are from 0mm to 9mm in 1mm steps. The top left image is for 0mm and the bottom right image is for 9mm. The 1mm incremental step proceeds from the top left image down the first column so that the top right image is for a standard deviation of 5mm.

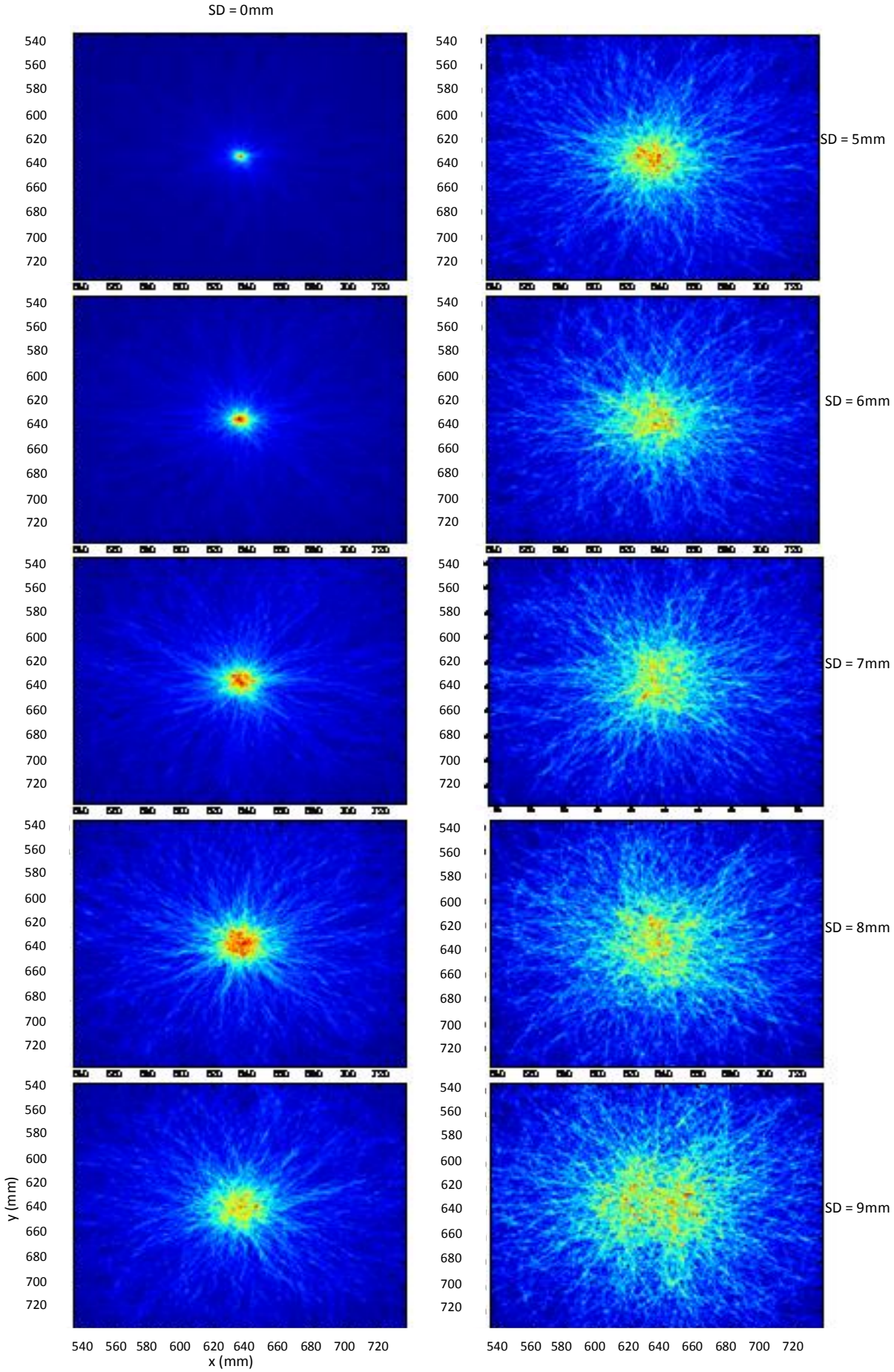

Figure A.3: Reconstructions of a simulated point source for a number of position resolution standard deviations.

A.3.2 Detector Multiplicities

Detector multiplicities for SP1 and SP2 in Compton camera configuration have been calculated for the ^{137}Cs point source. Tab. A.2 shows the relative intensity of different multiplicities for SP1 and SP2. The percentage of these multiple events which are identified as fold-1 is also shown. It can be seen that the majority of multiplicity-2 events are wrongly identified as fold-1. This implies that simple PSA will under perform if only fold-1 gates are applied to data analysis, because PSA assumes a fold-1 event is a single interaction. More advanced analysis is required to deal with these events.

Multiplicity SP1	Events	Percentage fold1 (%)	Multiplicity SP2	Events	Percentage fold1 (%)
1	26822	100	**1**	21091	100
2	8925	60	**2**	9974	62
3	3453	32	**3**	5347	40
4	1185	19	**4**	2657	28
5	352	13	**5**	1116	21
6	103	17	**6**	357	19
7	21	14	**7**	104	15
8	6	0	**8**	20	10
9	0	0	**9**	5	0
10	0	0	**10**	1	0

Table A.2: Analysis of the multiplicity and resulting fold in the Compton camera when imaging a ^{137}Cs point source.

Wavelet analysis can be used to identify multiplicity-2 events that are wrongly identified as fold-1. This is a significant fraction of the data. However, not all wrongly identified multiplicity-2 events can be identified and the scatter needs to travel through depth to be identified (*in-line* scattering). Fig. A.4 shows two histograms of scattering distance through depth for multiplicity-2 events wrongly identified as fold-1. Two histograms are shown for SP1 and SP2 respectively. The majority of these events are within 2mm and will probably not be identified (*in-plane* scatters). However, these add the smallest erroneous

contribution to interaction location determination, whilst the furthest apart scatters contribute the biggest error to spatial resolution. It is therefore advantageous to identify *in-line* scatters over *in-plane* scatters.

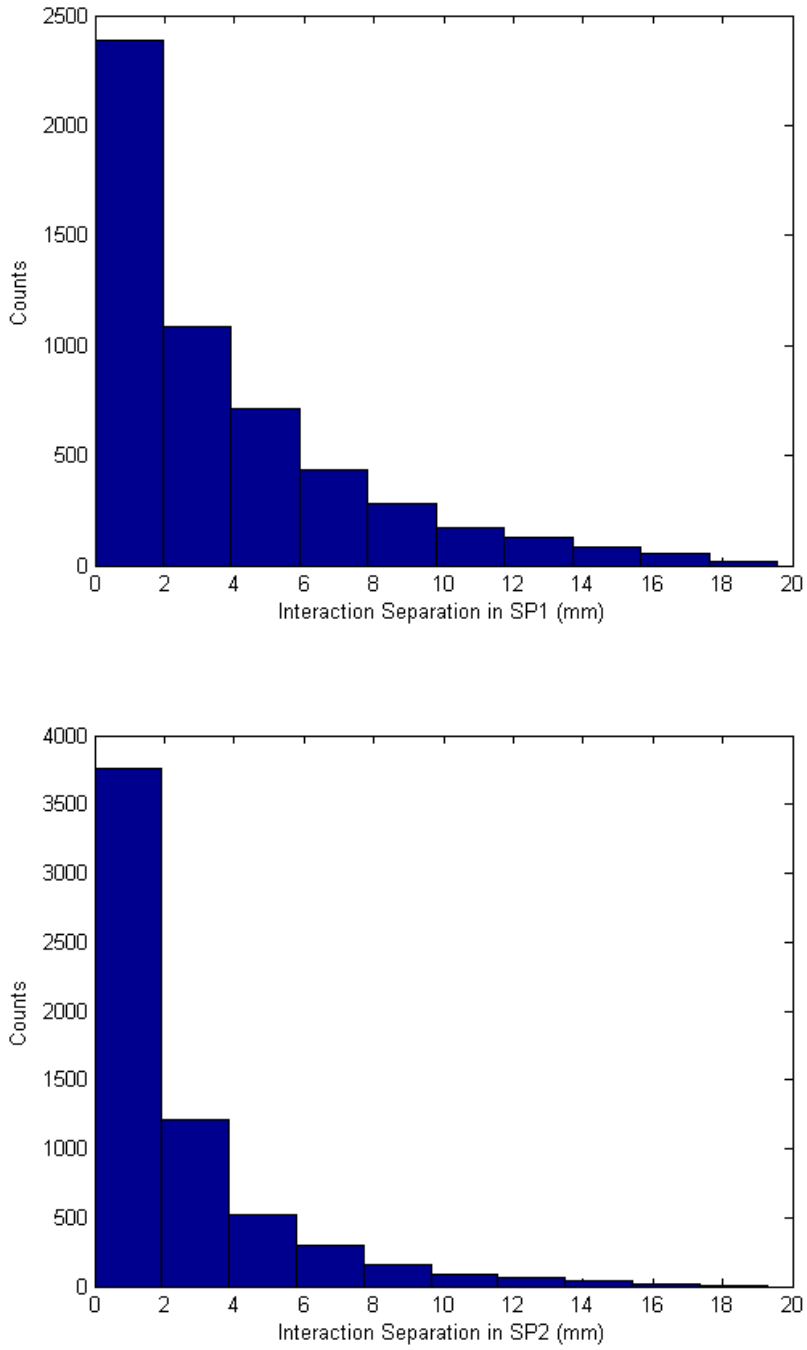

Figure A.4: Histograms of the distance through depth between the two interaction sites for multiplicity-2, fold-1 events; both the scattering (SP2) and absorbing detectors (SP1).

References

[Ago03] S. Agostinelli, et al, 'GEANT4: A Simulation toolkit', Nucl.Instrum.Meth.A506:250-303,2003

[Ang58] H.O. Anger, 'Scintillation Camera', Review of Scientific Instrumentation, Vol 29, pp. 27-33, 1958.

[Asp07] M. Aspinall, 'The empirical characterization of organic liquid scintillation detectors by the normalized average of digitized pulse shapes', NIMA 578 (2007) 261-266.

[Baz00] D. Bazzaco et al, Proceedings of the TMR user meeting, Cologne, 2000

[Bil67] H.R. Bilger, 'Fano Factor in Germanium at 77^{o}K', Physical review, Vol. 163 Num. 2, page 163-238, 1967

[Boc00] P. Boccacci, et al, 'The 2D+1 method for an efficient modelling of collimator blur in 3D SPECT imaging', ANALISI NUMERICA: Metodi e Software Matematico, 19 – 21 Gennaio (2000)

[Bol97] A. Bolozdynya, et al, 'A concept of cylindrical Compton camera for SPECT', Conference Record of the 1997 IEEE Nuclear Science Symposium and Medical Imaging Conference, Albuquerque, NM.

[Buc95] J. Buckheit, et al, 'Wavelab and reproducible research', Wavelets and Statistics, 1995.

[Che03] S. Cherry, et al, 'Physics in Nuclear Medicine', 3rd edition, W. B. Saunders, 2003, ISBN 9780721683416.

[Cli98] N. Clinthorne, et al, 'Choice of scattering detector for Compton-scatter camera', Journal of Nuclear Medicine, vol. 39, pp. 51P, 1998.

[Cli03] N. Clinthorne, et al, **'**Multi-resolution image reconstruction for a high-resolution small animal PET device', IEEE Nuclear Science Symposium Conference Record, Vol. 3, 1997 - 2001 (2003).

[Col06] J. Colinge, 'Physics of Semiconductor Devices', Springer, 2006.

[Cre07] F. Crespi, et al, 'A PULSE SHAPE ANALYSIS ALGORITHM FOR SEGEMENTED HPGe DETECTORS', ACTA PHYSICA POLONICA B, Vol. 38 (2007)

[Dav65] C.M. Davisson, 'Interaction of gamma-radiation with matter alpha, beta and gamma spectroscopy'. Ed. by Siegbahn, K. Pub. North-Holland, p37-78, 1965.

[Del99] M. Delephanque, et al, 'GRETA: utilizing new concepts in γ-ray detection', NIMA 430 (1999) 292 – 310.

[Des02] M. Descovich, 'Improving the position resolution of Highly Segmented HPGe Detectors using Pulse Shape Analysis Methods', Thesis, 2002.

[Dob03] J. J. Valiente-Dobon et al, Nucl. Instr. Meth. A505 (2003) 174.

[Dob05] J. Dobson, 'THE CHARACTERISATION AND POSITION RESOLUTION OF A PLANAR GERMANIUM STRIP DETECTOR', PhD Thesis, Liverpool, 2005

[Don94] D. Dononho, I. Johnstone, 'Threshold selection for wavelet shrinkage of noisy data', Eng. Med. and Bio. Soc. Vol. 1 (1994) A24-A25

[Ebe01] J. Eberth, et al, Prog. Part. Nucl. Phys. 46 (2001) 389

[Fra97] G. de France and J. Simpson. *Nucl. Phys. News* **7** 1 (1997), p. 12.

[Gam97] L. Gamir, 'A NEW METHOD FOR THE DETERMINATION OF THE ENTRY POSITION OF γ-RAYS IN HIGH PURITY', PhD Thesis, Cranfield, 1997.

[Geo93] Georgiev, U. and Gast, W. (1993): Digital Pulse Processing in High Resolution, High Throughput Gamma-Ray Spectroscopy, IEEE Transactions on nuclear science, Vol. 40, No.4, p. 770-779.

[Gil07] J. Gillam, et al, 'Volumetric Image Reconstruction of SmartPET Data Using a Compton-Camera Configuration', under review.

[Gri07] A. Grint, et al, 'A Semiconductor Compton Camera System in SPECT Mode', IEEE, MIC, Hawaii, October 2007.

[Gro05] S. Gros, 'Characterisation of an EXOGAM clover', PhD Thesis, Liverpool, 2005

[Ham05] N. Hammond, et al, 'Ambiguity in gamma-ray tracking of 'two-interaction' events', NIMA, 547 (2005) 535-540.

[He01] Z. He, 'Review of the Shockley-Ramo theorem and its application in semiconductor gamma-ray detectors', NIMA, 463 (2001) 250-267.

[Hir03] M. Hirasawa, T. Tomitani, 'An analytical image reconstruction algorithm to compensate for scattering angle broadening in Compton cameras', Phys. Med. Biol. 48 (2003) 1009-1026.

[Hol89] M. Holschneider, et al, 'Wavelets, Time-Frequency Methods and Phase Space', Springer-Verlag, 1989

[Hua00] Chia-ho, 'Compton Imaging System Development and Performance Assessment', PhD Thesis, Michigan, 2000.

[Hue99] R. H. Huesman et al, 'Motion compensation in cardiac nuclear medicine imaging', Abstract book of future directions in nuclear medicine physics and engineering symposium, Chicago, IL, March, 1999.

[Hut07] B. Hutton, 'Single Photon Emission Computed Tomography (SPECT)', Presentation at University College London, meeting 2007

[IOFFE] Ioffe Physico-Technical Institute, database for semiconductors, based on 'Handbook Series on Semiconductor Parameters', World Scientific, 1999.

[Kic97] C. Kicey, C. Lennard, 'Unique reconstruction of band-limited signals by a Mallet-Zhong wavelet transform algorithm', Fourier Analysis and Appl. 3(1): 63-82, 1997

[Kle42] Klein, O. and Y. Nishina, Z. Physik, vol. 52, p.415, 1942.

[Kno00] G.F. Knoll, 'Radiation Detection and Measurement', third edition, John Wiley & Sons, (2000)

[Kra88] K.S. Krane, 'Introductory Nuclear Physics', John Wiley & Sons, 1988.

[Kro96] T. Kroll, et al, 'Analysis of simulated and measured pulse shapes of closed-ended HP-Ge detectors', NIM A, 371 (1996), 489-496.

[Kro00] R.A. Kroeger, et al, 'Gamma Ray Measurement using the Multiple Compton Technique', Nuclear Science Symposium Conference Record, 2000 IEEE, 8/7-811 vol.1

[Kur04] J. Kurfess, et al, 'An advanced Compton telescope based on thick, position-sensitive solid-state detectors', New Astronomy Reviews, Vol. 48, Issues 1-4, February 2004, 293-298.

[Laz04] I. Lazarus et al. (2004) IEEE Trans. Sci. NS-51, 4, 1353.

[Lee03] I. Y. Lee, et al, 'Developments in large gamma-ray detector arrays', IoP, Rep. Prog. Phys. 66 (2003)

[Lee07] I. Y. Lee. Private communication.

[Leh04] C. Lehner, et al, '4π Compton Imaging Using a 3-D Position-Sensitive CdZnTe Detector Via Weighted List-Mode Maximum Likelihood', IEEE transactions on Nuclear Science, Vol. 51, No. 4 August 2004.

[Leo94] R. Leo, 'Techniques for nuclear and particle physics experiments', second edition, springer Verlag, (1994).

[Mal99] S. Mallet, 'A wavelet tour of signal processing', second edition, Academic Press, 1999

[Mar93] J. Martin, et al., 'A ring Compton camera for imaging medium energy gamma-rays', IEEE Trans Nuc Sci NS-40(4), 972-978 (1993)

[Mar94] J. Martin, 'A COMPTON SCATTER CAMERA FOR SPECTRAL IMAGING OF 0.5 TO 3.0 MeV GAMMA RAYS', PhD Thesis, Michigan, 1994.

[Mar01] J. van der Marel, B. Cederwall, 'Collimatorless imaging of gamma rays with help of gamma-ray tracking', NIMA 471 (2001) 276-280

[Mat06] A. Mather, 'Evaluation of the Planar Germanium SmartPET system for use in Positron Emission Imaging', PhD Thesis, Liverpool, 2006

[Mih00] L. Mihailescu, 'PRINCIPLES AND METHODS FOR γ-RAY TRACKING WITH LARGE VOLUME GERMANIUM DETECTORS', PhD Thesis, Bonn, 2000

[Mih04] L. Mihailescu et al, 'SPEIR: a Ge Compton camera', Elsevier, 2004

[Mil05] L. Milechina, B. Cederwall, '3D position sensitivity of a highly segmented Ge detector', NIMA 550 (2005) 278-291.

[Nol85] P. Nolan, et al, Nucl. Inst. Meth. A236, 95, 1985

[Nor79] S. Norton, M. Linzer, 'Ultrasonic Reflectivity Tomography: Reconstruction with Circular Transducer Arrays', Ultrasonic Imaging, Vol. 1, (1979) 154-184

[Ord99] C. Ordonez, et al, 'Angular Uncertainties due to Geometry and Spatial Resolution in Compton Cameras', IEEE Transactions on Nuclear Science, Vol. 46, No. 4, August 1999.

[Par04] G. Parker, 'Introductory Semiconductor Device Physics', IoP Publishing, 2004.

[Pea02] C. Pearson, et al, 'Digital gamma-ray tracking algorithms in segmented germanium detectors', IEEE Transactions on Nuclear Science, Vol. 49 (2002) 1209-1215.

[Pei92] A. Peisert, INFN report on Silicon microstrip detectors, 1992.

[Pet93] F. Petry et al, 'Background recognition in Ge detectors by pulse shape analysis', nuclear instruments and methods, section A 332 (1993) 107 – 112.

[Phl02] B. Phlips, et al, 'Small Animal PET Imaging with Germanium Strip Detectors', Nuclear Science Symposium Conference Record IEEE, Vol. 3, (2002), 1438 – 1442.

[PICKER] PICKER product information relating to PRISM 1000XP and PRISM 2000XP collimators, currently used at the Royal Liverpool Hospital

[Pie96] R. Pierret, 'Semiconductor Device Fundamentals', Addison-Wesley, 1996.

[Piq04] I. Piqueras, et al, 'Segmented germanium detector developments for Compton Camera application', NIMA 525 (2004) 275 – 278.

[Rad88] V. Radeka, 'LOW-NOISE TECHNIQUES IN DETECTORS', Ann. Rev. Nucl. Part. Sci., 38, pages 217-277, 1988.

[Ram39] S. Ramo, 'Currents induced by electron motion', Proceedings of the I.R.E., September 1939, p. 584.

[Rog01] W. Rogers, et al, 'Compton Cameras for Nuclear Medical Imaging', Vol. 3, Jan. 10, 2001.

[Ros93] C. R. Alvarz, 'The GASP array', Nuclear Physics News, *Nucl. Phys. News /bf* **3** 3 (1993), p. 10.

[Sam00] J. Sampson, MTsort Language, Edition 2.20 (2000), Web page: http://nnsa.dl.ac.uk/MIDAS/manual

[San03] P. Sangsingheow et al, 'Advances in germanium detector technology', Nuclear Instruments and Methods, Section A, 505 (2003) 0 183-186

[Sch77] V. Schoenfelder, et al., 'Measurement of 1-30 MeV Gamma Rays with an Imaging Compton Telescope "Comptel"', Astrophysical Journal 217 (1977) 306

[Sch86] D Schaile, et al, 'A simultaneous hit finding and timing method for pulse shape analysis of drift chamber signals', Nuclear Instruments and Methods in Physics Research A242 (1986) 247-253

[Sch92] S. Schwebel, 'Pulsform-Analyse von High Purity Germanium-Detektoren mit Flash', PhD Thesis, Max-Planck-Institut, 1992

[Sho38] W. Shockley, 'Currents to conductors induced by a moving point charge', J. Appl. Phys. 9, 635, 1938.

[Sim06] J. Simpson, 'The AGATA project', Journal of Physics: Conference Series 41, (2006) 72 – 80.

[Sin81] M Singh, D. Doria, SPIE-273, 192-200(1981)

[Sin83a] M. Singh, D Doria, 'An electronically collimated gamma camera for single photon emission computed tomography. Part II: Image reconstruction and preliminary experimental measurements', Medical Physics -- July 1983 -- Volume 10, Issue 4, pp. 428-435

[Sin83b] M. Singh, 'An Electronically Collimated Gamma Camera for Single Photon Emission Computed Tomography. Part I: Theoretical Considerations and Design Criteria', Med. Phys. Vol. 10, No. 4. Pp. 421-427, 1983.

[Sor87] J.A. Sorenson and M.E. Phelps, Physics in nuclear medicine, 2nd ed., Grune and Stratton, Orlando, Florida, 1987.

[Spi01] H. Spieler, 'Radiation Detectors and Signal Processing', LBNL Lectures, 2001.

[Scr07] D. Scraggs, et al, 'Signal analysis and processing for SmartPET', NIMA, Vol. 573, issue 1-2, p. 95-98, 2007.

[Sur92] Suric, T., 'Compton Scattering from Bound Electrons: Comparisons of the Impulse Approximation with Exact IPA Calculations', Nucl. Inst. Meth., vol. A314, pp. 240-243, 1992.

[Tan06] Tanimori et al, 'Advanced Compton Camera with the ability in electron tracking based on Micro Pixel Gas Detector for Medical Imaging', Nuclear Science Symposium Conference Record, 2006. IEEE, Volume: 6, On page(s): 3870-3874

[Tar03] G. Tarantola, et.al, 'PET Instrumentation and Reconstruction Algorithms in Whole-Body Applications', The Journal of Nuclear Medicine, Vol.44, No. 5, p. 756-769. (2003)

[Tod74] R.W. Todd et al., 'A proposed γ camera', *Nature* 251, 132 - 134 (13 September 1974)

[TUNG] Tungsten company data sheet. http://tungstenco.com/tungstenalloys.htm

[Tur06] G. Turk, 'The characterisation of the first SmartPET HPGe planar detector', Thesis, 2006.

[Use01] B Usevitch et al, 'A tutorial on modern lossy wavelet image compression: foundations of JPEG 2000', Sig. Pro. Mag. IEEE, Vol 18 (2001) 22-35.

[Vet00] K. Vetter et al, 'Three-dimensional position sensitivity in two-dimensionally segmented HP-Ge detectors', NIMA, 452 (2000) 223-238.

[Vet04] K. Vetter, et al, 'Gamma-ray imaging with position-sensitive HPGe detectors', NIM A, 525 (2004) 322-327.

[Whi68] R. Stephen White, Bull. Am. Phys. Soc. Ser II 13, No. 4, 714 (1968)

[Wul03] E. Wulf, et al, 'Germanium Strip Detector Compton Telescope Using Three-Dimensional Readout', IEEE Trans. Nuc. Sci. Vol. 50, No. 4, August 2003.

[Xu06] Dan Xu, et al, ' Filtered Back-Projection in 4_ Compton Imaging With a Single 3D Position Sensitive CdZnTe Detector', IEEE TRANSACTIONS ON NUCLEAR SCIENCE, VOL. 53, NO. 5, OCTOBER 2006